

The Harmonic Synthetic Control Method *

Ziyi Liu
(UC Berkeley)

Yiqing Xu
(Stanford)

May 21, 2026

Abstract

Synthetic control methods can produce misleading counterfactual predictions when outcome series contain unit-specific stochastic trends, a common feature of nonstationary macroeconomic data. Existing remedies, such as pre-filtering or differencing, reduce spurious matching but may discard *shared* nonstationary variation that helps estimate donor weights. We propose Harmonic Synthetic Control (HSC), which replaces this binary choice with a soft allocation mechanism. HSC jointly estimates donor weights and a treated-unit-specific smooth residual component, then extrapolates this component into post-treatment periods using a time-series forecaster. A tuning parameter, selected by rolling-origin cross-validation, governs the division between donor matching and forecasting. As it varies, HSC continuously interpolates between synthetic control applied to differenced outcomes and synthetic control applied to raw outcomes with an intercept or trend. We provide a spectral interpretation showing how HSC downweights low-frequency residual components in donor matching and assigns them to the forecasting branch. A prediction-error decomposition separates weight-estimation distortion from residual-forecasting error. Monte Carlo exercises show that HSC adapts across regimes, performing well when stochastic trends are predominantly common or idiosyncratic, while estimators fixed to one regime can fail in the other.

Keywords: synthetic control, nonstationarity, spurious regression, causal inference, frequency domain

*Ziyi Liu, PhD student, Haas School of Business, University of California, Berkeley. Email: zyliu2023@berkeley.edu. Yiqing Xu, Assistant Professor, Department of Political Science, Stanford University. Email: yiqingxu@stanford.edu. This project was inspired by discussions with Hongyu Mou and Yifan Sun regarding the replication of synthetic control studies. We thank David Bruns-Smith, Kevin Chen, Alex Hayes, Guido Imbens, Lihua Lei, David Ritzwoller, Sarah Vicol, and participants at the Stanford Metrics Lunch for their helpful comments. The authors used Claude Code Opus 4.7 as a research, coding, and writing assistant in preparing this manuscript. All errors remain solely the responsibility of the authors.

1. Introduction

Synthetic control methods construct counterfactuals for treated units by finding weighted combinations of untreated donors that match the treated unit’s pre-treatment outcome path (Abadie and Gardeazabal, 2003; Abadie, Diamond and Hainmueller, 2010, 2015). The logic is that if a weighted combination of donors can reproduce the treated unit’s outcomes before treatment, the same combination should approximate what the treated unit’s outcomes would have been in the absence of treatment. A difficulty arises when outcome series are nonstationary: the pre-treatment fit that synthetic control exploits may be spurious. Specifically, when units contain unit-specific stochastic trends, a convex combination of donors can closely track the treated unit’s pre-treatment path through coincidental co-movement rather than shared structure, producing in-sample fit that breaks down out of sample and leading to biased estimation and distorted inference (Phillips, 1986; Masini and Medeiros, 2021, 2022; Shi, Xi and Xie, 2025).

Existing responses to this problem face a tradeoff over whether to preprocess the data, such as detrending or differencing. These transformations turn nonstationary time series into stationary ones, thereby alleviating the spurious matching risk. However, these transformations also discard nonstationary variation that the treated unit potentially shares with donor units, which is the main source of identifying variation for donor-weight estimation in synthetic control (Ferman and Pinto, 2021; Abadie, 2021). Other variants of synthetic control, such as augmented or bias-corrected extensions, can reduce the residual imbalance left by imperfect pre-treatment fit (Ben-Michael, Feller and Rothstein, 2021; Arkhangelsky et al., 2021), but because they still begin from weights chosen to match raw pre-treatment outcomes, they can inherit the same underlying weight distortion caused by spurious matching.

We formalize this tradeoff through a conceptual distinction. In macroeconomic panel data, nonstationarity typically takes the form of persistent stochastic components, such as random walks or other integrated processes, whose variance grows without bound over time. We categorize this stochastic trend variation into two sources. By a *shared stochastic trend*, we mean a stochastic trend component whose innovations are shared across units; such a trend moves the treated unit

and donors together, possibly with unit-specific responses. Synthetic control is designed to exploit this shared structure, using a weighted combination of donors to approximate the treated unit’s trajectory. By an *idiosyncratic stochastic trend*, we mean a stochastic trend component whose realizations are unit-specific and do not generate stable comovement across units, even though they may appear correlated by chance in any finite sample. This is the source of the spurious matching problem. We use *stochastic trend* as an umbrella term for both.

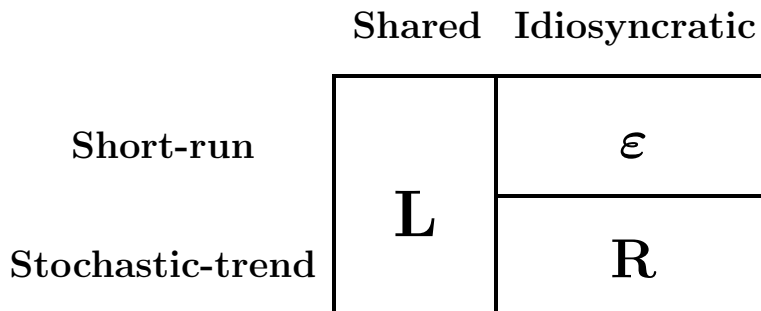


Figure 1. SCHEMATIC DECOMPOSITION OF UNTREATED POTENTIAL OUTCOMES.

Notes: L denotes the component governed by the shared factors, which may contain both short-run and stochastic trend latent factors. ϵ denotes idiosyncratic short-run noise. R denotes an idiosyncratic stochastic trend that is not governed by the shared factor structure.

Based on these concepts, we decompose untreated potential outcomes of the treated unit and all control donors into three components (Figure 1). The first is a component L , possibly low-rank and driven by shared latent factors whose loadings vary across units. These factors may include both stochastic trend and short-run variations.¹ The second is idiosyncratic short-run noise ϵ . It does not fundamentally distort donor-weight estimation: it averages out over long pre-treatment windows under standard moment conditions. The third is the idiosyncratic stochastic trend R , which is not governed by the shared factor structure. Unlike ϵ , R can severely distort donor-weight estimation: independent stochastic trends produce realized correlations whose magnitude does not vanish as T_0 grows, so longer pre-treatment windows do not help (Phillips, 1986). Whether the stochastic trend variation in the treated unit’s series is mostly shared(captured by L) or idiosyncratic (captured by R) is generally unknown to the researcher ex ante. In the first case, preprocessing removes the

¹We avoid the labels stationary and nonstationary because what matters for our analysis is bounded long-run variance, not strict stationarity. By short-run we mean variation with bounded long-run variance, which includes strictly stationary processes as well as bounded-variance nonstationary processes.

variation that synthetic control would otherwise use for donor-weight estimation. In the second case, allowing stochastic trends to enter weight estimation creates the risk of spurious matching. This tradeoff motivates us to propose a solution that adapts to both regimes.

This paper proposes *harmonic synthetic control* (HSC), which replaces this binary choice of pre-processing with a soft, data-driven allocation. HSC jointly estimates donor weights and a treated-unit-specific smooth component E that absorbs idiosyncratic trend-like variation not reproducible by a convex combination of donors. The roughness of E is controlled by a penalty $\|D_q E\|_2^2$, where D_q is the q th-order difference operator, with $q \in \{1, 2\}$ specifying the order of smoothness. The division of labor between donor matching and the smooth component is governed by a single tuning parameter $\rho \in [0, 1]$, selected by rolling-origin cross-validation. When ρ is close to 1, HSC imposes a high penalty on the roughness of E and recovers synthetic control with an intercept or with an intercept plus a linear trend, depending on whether $q = 1$ or $q = 2$. When ρ is close to 0, E absorbs the entire discrepancy between the treated unit and the convex combination of donors, and the weight estimation in HSC approaches synthetic control applied to first or second differences of the raw outcomes (for $q = 1$ or $q = 2$, respectively). At intermediate ρ , HSC continuously interpolates between these two endpoints. In post-treatment periods, the smooth component is forecast by a time series forecaster, and the counterfactual is constructed by adding the forecast of E to the donor matching component. HSC does not attempt to disentangle which portion of the stochastic trend variation is shared and which is idiosyncratic; instead, cross-validation selects the allocation between donor matching and the smooth component that yields the best out-of-sample predictive performance.

This soft allocation has a clean spectral interpretation. Any pre-treatment series can be decomposed into components at different frequencies: low-frequency content carries slowly varying (trend-like) variation, while high-frequency content carries short-run variation. The HSC weight estimation problem down-weights low-frequency components and amplifies high-frequency components, thus alleviating the spurious matching risk. The treated-unit-specific component E absorbs the low-frequency residual variation that remains after donor matching, and the post-treatment forecast of E extrapolates this low-frequency, trend-like component forward in time. Equivalently,

HSC can be understood as applying synthetic control to a soft spectral transformation of the raw data that interpolates between two extremes: at $\rho = 0$, the transformation reduces to q -th order differencing, which strongly suppresses low-frequency content; at $\rho = 1$, the transformation removes only the null-space component (constants for $q = 1$, constants plus linear trends for $q = 2$), leaving other frequencies unchanged. The method’s name reflects the form of this interpolation: at each frequency, the spectral gain of the HSC transformation is a weighted harmonic mean of the gains at the two endpoints, with weights $1 - \rho$ and ρ .

We develop an envelope bound on the HSC counterfactual’s prediction error. The error decomposes into a weight-estimation term and a forecasting term, each depending on ρ . The weight-estimation term reflects that the researcher observes $Y = L + R + \varepsilon$ rather than the shared component L alone; the HSC-estimated donor weights therefore deviate from the oracle weights constructed from L alone. This term captures the tradeoff between the risk of spurious matching at large ρ and the downweighting of useful low-frequency variation in L at small ρ . The forecasting term captures the error that would remain even with oracle weights; depending on the prediction quality of the time series forecaster, this term can be monotonically increasing, monotonically decreasing, or non-monotonic in ρ . Together these two terms determine the tradeoff that cross-validation aims to balance in the choice of ρ .

The synthetic control literature has produced many methods that match donors to the treated unit’s pre-treatment outcomes, differing in weight constraints, bias-correction strategies, and temporal aggregation (Doudchenko and Imbens, 2016; Ben-Michael, Feller and Rothstein, 2021; Arkhangelsky et al., 2021; Sun, Ben-Michael and Feller, 2024). A growing subset of this literature addresses synthetic control specifically under nonstationarity. Masini and Medeiros (2021, 2022) show that counterfactual estimation requires a cointegrating relationship between treated and donor units; without it, estimated effects diverge and inference suffers severe size distortion. Harvey and Thiele (2021) model the common stochastic trend explicitly and propose stationarity tests on the pre-treatment difference as a diagnostic for donor selection. Shi, Xi and Xie (2025) decompose outcomes into trend and cycle via the Hamilton filter and restrict donor matching to the cyclical residual. These contributions diagnose the nonstationarity problem or propose hard filters that

remove persistent variation before matching. HSC introduces the smooth component E as a new degree of freedom; rather than diagnosing nonstationarity or applying a fixed filter, HSC offers a soft, data-driven alternative that retains shared stochastic trend while mitigating idiosyncratic spurious matching.

The estimator’s mechanism draws on a different technical toolkit than is standard in the synthetic control literature. The roughness penalty $\|D_q E\|_2^2$ connects HSC to the Whittaker–Henderson smoothing framework (Whittaker, 1922; Henderson, 1924), the Hodrick–Prescott filter (Hodrick and Prescott, 1997), and penalized spline formulations (Eilers and Marx, 1996). The spectral decomposition of the HSC metric, in which the tuning parameter ρ acts as a frequency-dependent gain function on the pre-treatment residual, imports ideas from spectral analysis in time series into the synthetic control setting. This connection provides both interpretive clarity (ρ governs a soft spectral partition between what is matched cross-sectionally and what is forecasted univariately) and computational tractability, since the profiled HSC objective reduces to a standard constrained quadratic program.

We illustrate the method on the canonical Hong Kong example, the path of per-capita GDP after the 1997 return of Hong Kong to Chinese sovereignty, studied by Hsiao, Ching and Wan (2012) and Shi, Xi and Xie (2025). Cross-validation selects an interior allocation rather than either preprocessing extreme, confirming that the data prefer a soft partition between donor matching and the smooth component. HSC distributes donor weight broadly across the control pool, whereas level-matching and filter-based competitors either concentrate weight on a few donors or extrapolate the treated unit’s own trend and overshoot the observed series. On a rolling-origin out-of-sample criterion HSC is the most accurate estimator among those we compare, and this ranking is stable across the cross-validation horizon and across two very different donor-selection philosophies. The application thus reproduces, in real data, the soft-allocation behavior that the theory and the Monte Carlo evidence predict.

The remainder of the paper is organized as follows. Section 2 formalizes the outcome decomposition, establishes notation, and characterizes the two failure modes (spurious donor matching and over-filtering) that motivate the need for a soft allocation mechanism. Section 3 introduces

the HSC estimator, derives its profiled representation, and constructs the forecast operator that extrapolates the smooth component into post-treatment periods. Section 4 develops the spectral interpretation, showing that the tuning parameter ρ acts as a frequency-dependent gain function, and describes the cross-validation procedure for selecting ρ . Section 5 presents the prediction-error decomposition into weight-estimation and forecasting terms, and discusses the trade-off under the selection of ρ . Section 6 reports Monte Carlo evidence for the HSC estimator. Section 7 applies HSC to the 1997 Hong Kong handover and compares it with established alternatives. Section 8 concludes.

2. A Tradeoff between Spurious Donor Matching and Over-Filtering

This section formalizes the allocation problem described in the Introduction. We first establish notation for the synthetic control setting, then provide the formal $L + R + \varepsilon$ decomposition and characterize two failure modes: spurious donor matching when the idiosyncratic stochastic trend R dominates, and over-filtering when shared stochastic trend in L is discarded. A simulated illustration shows that existing methods commit to one regime or the other.

2.1. Setup and notation

We observe a panel of $N_0 + 1$ units over $T = T_0 + T_{\text{post}}$ periods. Unit $i = 1$ is the treated unit; units $i = 2, \dots, N_0 + 1$ form the donor pool. Treatment is imposed at the end of period T_0 , so the pre-treatment window is $t = 1, \dots, T_0$ and the post-treatment window is $t = T_0 + 1, \dots, T$. Let $Y_{it}(0)$ denote the untreated potential outcome for unit i at time t . Under the standard no-anticipation assumption, we observe $Y_{1t} = Y_{1t}(0)$ for $t \leq T_0$. Let $X_t = (Y_{2t}, \dots, Y_{N_0+1,t})'$ denote the $N_0 \times 1$ vector of donor outcomes at time t . We write $Y_{\text{pre}} = (Y_{1,1}, \dots, Y_{1,T_0})'$ and $X_{\text{pre}} = (X_1, \dots, X_{T_0})'$ for the $T_0 \times 1$ and $T_0 \times N_0$ pre-treatment arrays. Y_{post} and X_{post} are defined similarly.

The synthetic control estimator constructs a counterfactual for the treated unit as a weighted combination of donors. The weights $\hat{\omega}$ are chosen from the simplex $\Delta = \{\omega \in \mathbb{R}^{N_0} : \omega \geq 0, \mathbf{1}'\omega = 1\}$

by minimizing the pre-treatment sum of squared residuals:

$$\hat{\omega} = \arg \min_{\omega \in \Delta} \|Y_{\text{pre}} - X_{\text{pre}}\omega\|^2,$$

and the counterfactual at horizon $h \geq 1$ is $\hat{Y}_{1,T_0+h}(0) = X'_{T_0+h}\hat{\omega}$. A common simplex-constrained extension adds an intercept $\hat{\alpha}$ to absorb a constant level shift between the treated unit and the weighted donors. The weights and intercept are estimated jointly:

$$(\hat{\omega}, \hat{\alpha}) = \arg \min_{\omega \in \Delta, \alpha \in \mathbb{R}} \|Y_{\text{pre}} - X_{\text{pre}}\omega - \alpha \mathbf{1}_{T_0}\|^2,$$

which is equivalent to matching on demeaned pre-treatment outcomes (Doudchenko and Imbens, 2016; Ferman and Pinto, 2021). The counterfactual becomes $\hat{Y}_{1,T_0+h}(0) = X'_{T_0+h}\hat{\omega} + \hat{\alpha}$.

Both formulations share the same basic structure: donor weights are chosen to minimize a pre-treatment loss computed on the observed outcome series, and the counterfactual extrapolates those weights into the post-treatment window.

2.2. Decomposing untreated outcomes and the allocation problem

We now formalize the decomposition introduced informally in Section 1 (Figure 1). We decompose untreated potential outcomes into three components:

$$Y_{it}(0) = L_{it} + R_{it} + \varepsilon_{it}. \tag{1}$$

Here $L_{it} = \Lambda'_i F_t$ is a shared low-rank component, where F_t collects latent factors and Λ_i is the corresponding vector of unit-specific loadings. The factors F_t may contain both short-run and stochastic trend movements. The defining property of L_{it} is that it is *shared*: when a convex combination of donors matches the treated unit's loadings Λ_1 , it reproduces L_{1t} in every period. By contrast, R_{it} and ε_{it} are idiosyncratic. The term R_{it} denotes an idiosyncratic stochastic trend, whose long-run variance grows without bound, whereas ε_{it} denotes idiosyncratic short-run noise with bounded long-run variance. Unlike the shared component, neither R_{it} nor ε_{it} is governed by a shared factor structure. As a result, observed outcomes may mask the low-rank structure in L_{it} , with the main difficulty arising from the idiosyncratic stochastic trend component R_{it} .

This decomposition refines the outcome framework of Arkhangelsky et al. (2021) by separating

idiosyncratic stochastic trends from short-run idiosyncratic noise. In [Arkhangelsky et al.](#)'s notation, untreated outcomes are represented by a systematic component \mathcal{L}_{it} and an idiosyncratic error ϵ_{it} . Their asymptotic analysis allows \mathcal{L} to be an approximately low-rank systematic matrix, without imposing a fixed known rank, while their Assumption 1 restricts the rows $\epsilon_{i\cdot}$ of the noise matrix to be i.i.d. Gaussian vectors with covariance matrix $\Sigma \in \mathbb{R}^{T \times T}$ whose eigenvalues are bounded and bounded away from zero. This condition permits temporal dependence and some forms of nonstationary covariance heterogeneity. In the growing- T asymptotics under which Assumption 1 is imposed, however, it excludes integrated unit-specific stochastic trends: if ϵ_{it} were a random walk with innovation variance σ^2 , then $\text{Cov}(\epsilon_{is}, \epsilon_{it}) = \sigma^2 \min\{s, t\}$, so the largest eigenvalue of Σ grows on the order of T^2 and is not bounded uniformly in T , violating the bounded-eigenvalue requirement of Assumption 1. Our decomposition therefore writes the idiosyncratic component as $R_{it} + \varepsilon_{it}$, where R_{it} captures the unit-specific stochastic trend excluded by the bounded-eigenvalue condition and ε_{it} denotes the remaining short-run noise. This split makes explicit the type of persistent idiosyncratic variation that we argue is central to the spurious matching problem.

A parallel restriction appears in [Ferman and Pinto \(2021\)](#), who study synthetic control in the fixed- N , large- T_0 regime under a linear factor model with common factors, unit-specific loadings, and idiosyncratic shocks ϵ_{it} . Their Assumption 4 requires the pre-treatment moments to converge in probability to non-stochastic constants: $T_0^{-1} \sum_t \epsilon_{it}^2 \xrightarrow{p} \sigma_\epsilon^2$, with analogous conditions on the common factors and on cross-products of factors and noise. The substantive content matches [Arkhangelsky et al.](#)'s Assumption 1: the idiosyncratic noise must have bounded long-run variance with well-behaved pre-treatment sample moments. An idiosyncratic random walk in ϵ_{it} violates Assumption 4 in the same way it violates the bounded-eigenvalue condition.

As discussed in Section 1, the fitting criterion in Section 2.1 operates on observed outcomes and therefore does not distinguish among L_{it} , R_{it} , and ε_{it} . The resulting allocation problem, deciding how much stochastic trend variation to attribute to the shared component L_{it} versus the idiosyncratic stochastic trend R_{it} , leads to two failure modes formalized in the following subsections.

2.3. The risk of spurious donor matching

When R_{it} contributes substantially to $Y_{it}(0)$, the pre-treatment optimization can achieve a close fit by assigning weight to donors whose independent persistent movements happen to co-move with the treated unit over the observed window. This is a manifestation of spurious regression in the synthetic control setting: the in-sample fit may appear excellent, yet it is driven by coincidental trending behavior rather than a shared factor structure, and therefore does not extend beyond the pre-treatment period. Shi, Xi and Xie (2025) formalize this as the *spurious synthetic control* problem, noting that “even if a country’s GDP can be closely approximated by a weighted average of others over a given period, such a fit may arise purely from coincidental trending behavior.” The simplex constraints $\omega \geq 0$, $\mathbf{1}'\omega = 1$ narrow the feasible set but do not prevent spurious fit: independent random walks can still produce close pre-treatment matches within the simplex.

It is worth emphasizing that the central failure is *weight distortion*, not merely imperfect fit. When R_{it} is quantitatively important, the optimizer is drawn toward donors whose idiosyncratic trends happen to track R_{it} in the pre-treatment period, pulling the weights away from the combination that would best reproduce the shared component L_{it} . This distinction between weight distortion and lack of fit is important because several recent proposals, including augmented synthetic control (Ben-Michael, Feller and Rothstein, 2021) and synthetic difference-in-differences (Arkhangelsky et al., 2021), improve on the standard synthetic control by augmenting it with an outcome model that corrects for the residual imbalance left by imperfect pre-treatment fit. Because these methods still begin from the donor weights chosen to match pre-treatment outcome levels, they can inherit the same underlying weight-distortion channel: the bias-correction step operates conditional on already-distorted weights, so it can at best mitigate but does not fully undo this distortion.

More fundamentally, the existing literature on synthetic control with nonstationary data identifies cointegration between the treated unit and the synthetic control as the key condition separating valid donor matching from spurious fit. In the regression-based framework studied by Masini and Medeiros (2021), counterfactual estimation requires the data-generating process to admit a cointegrating relationship involving the treated unit; without such a relationship, the regression is

spurious. [Masini and Medeiros \(2022\)](#) show that in this case the estimated treatment effect diverges and that ignoring the nonstationary nature of the data leads to severe over-rejection of the null hypothesis of no effect. [Harvey and Thiele \(2021\)](#) reach a similar conclusion from a structural time series perspective: they model the shared stochastic trend explicitly and argue that a synthetic control is valid when the target and control series share a common stochastic trend, proposing stationarity tests on the pre-treatment difference as a diagnostic for donor selection.

In the language of Section 2.2, cointegration between the treated unit and the synthetic control therefore requires that the stochastic trend content of their difference be eliminated not only in the pre-treatment period but also out of sample. When the stochastic trend variation is entirely driven by shared factors in L_{it} , a cointegrating relationship among the units is guaranteed by the factor structure, and the donor weights that minimize the pre-treatment criterion can recover the common component both in pre- and post-treatment periods. When the treated unit also contains a quantitatively important idiosyncratic stochastic trend R_{1t} , the cointegrating relationship involving the treated unit may not exist, and the critiques from the cited literature then apply directly.

2.4. The cost of hard filtering

The previous subsection showed that level-based matching is vulnerable to spurious donor matching when R_{it} is large. Two natural responses have been proposed, both of which remove stochastic trend variation before constructing the synthetic control.

The first is explicit pre-filtering. [Shi, Xi and Xie \(2025\)](#) propose decomposing the outcome into a trend and a cyclical component using the Hamilton filter ([Hamilton, 2018](#)), forecasting the treated unit’s trend from its own lagged values, and restricting donor matching to the stationary cyclical residual. Their strategy is designed to eliminate spurious matching from idiosyncratic stochastic trend by construction under the maintained trend-cycle decomposition: the Hamilton filter removes the trend component, and donor matching is then applied to the resulting cyclical residual rather than to the raw persistent series.

The second is differencing. If R_{it} is a random walk, first-differencing yields $\Delta Y_{it} = \Delta L_{it} + \Delta R_{it} + \Delta \varepsilon_{it}$, where ΔR_{it} is now stationary. This logic underlies the concern raised by [Masini and](#)

Medeiros (2022) that nonstationary data can produce spurious counterfactual estimates, motivating transformations such as differencing before applying counterfactual methods, and is related to Abadie’s (2021) observation that matching in differences can help when levels are not credibly matchable.

Both strategies address the spurious matching problem, but they share a common cost: neither distinguishes between R_{it} and the stochastic trend part of L_{it} . If the common factor F_t is a random walk with heterogeneous loadings Λ_i , then first-differencing removes the resulting stochastic trend in $\Lambda_i'F_t$ entirely. Ferman and Pinto (2021) show that when common factors include diverging non-stationary components, these components dominate the pre-treatment fitting criterion as T_0 grows, providing the primary source of identifying variation for donor weight estimation. Mechanically removing them discards an important signal for donor matching. What remains after filtering or differencing is a stationary factor structure with potentially much lower signal-to-noise ratio. The resulting donor weights can become substantially more imprecise and perform poorly in recovering the shared component of L_{it} . Abadie (2021) indeed notes that matching in first differences can inflate the variance attributable to noise, potentially inducing an increase in bias.

2.5. Illustration of the tradeoff

The preceding two subsections identified a tension between two failure modes: spurious donor matching when R_{it} dominates, and over-filtering when shared stochastic trend variation in L_{it} is discarded. The relative severity of these two risks depends on the magnitude of R_{it} relative to L_{it} .

Figure 2 illustrates the tradeoff with a simulated example. The data-generating process is $Y_{it}(0) = \Lambda_i'F_t + \kappa \cdot R_{it} + \varepsilon_{it}$, where F_t is a shared random-walk factor with heterogeneous loadings ($\Lambda_i \sim N(1, 1)$), R_{it} are idiosyncratic random walks, and ε_{it} is iid noise with $\sigma_\varepsilon = 2$. The common factor structure is the same across the two rows; the only difference is the importance of the idiosyncratic stochastic trend, governed by κ . The top row sets $\kappa = 0$ (only shared stochastic trend); the bottom row sets $\kappa = 2$ (an idiosyncratic stochastic trend added on top of the same common structure). Each column applies a different estimator. The first is synthetic control in levels with an intercept, which constructs the counterfactual as $\hat{Y}_{1, T_0+h}(0) = X_{T_0+h}'\hat{\omega}^{\text{lev}} + \hat{\alpha}$, where $\hat{\alpha}$

absorbs a constant shift between the treated unit and the weighted donors. The second is synthetic control in first differences, which estimates donor weights on the differenced data ΔY_{it} and anchors the counterfactual at the last pre-treatment observation: $\hat{Y}_{1,T_0+h}(0) = X'_{T_0+h} \hat{\omega}^{\text{dif}} + (Y_{1,T_0} - X'_{T_0} \hat{\omega}^{\text{dif}})$.

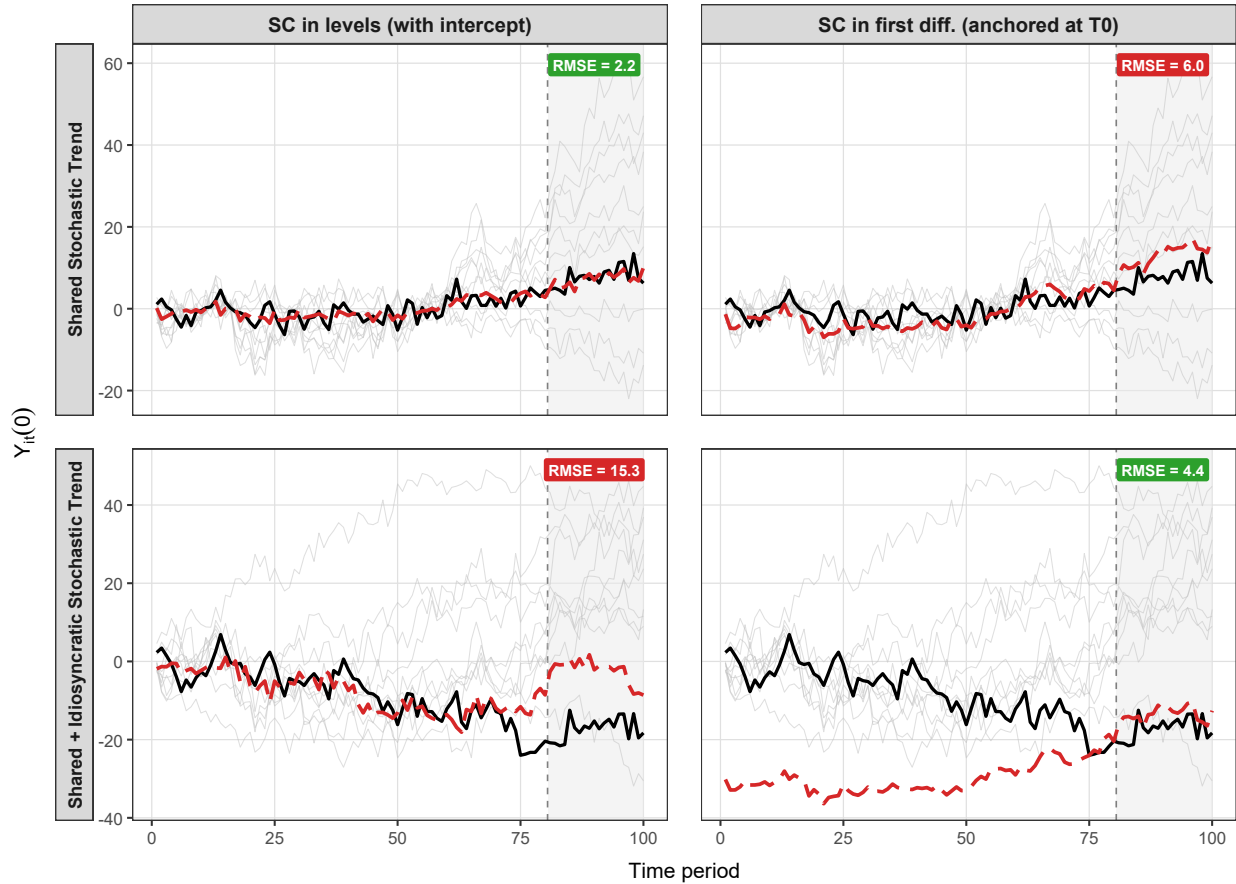


Figure 2. SPURIOUS DONOR MATCHING VERSUS OVER-FILTERING.

Notes: Solid black lines show the treated unit's outcome path (no treatment effect is imposed). Dashed red lines show the synthetic control counterfactual. Thin grey lines show individual donor units. The shaded region marks post-treatment periods. The data-generating process is $Y_{it}(0) = \Lambda'_i F_t + \kappa \cdot R_{it} + \varepsilon_{it}$ with one common random-walk factor, loadings $\Lambda_i \sim N(1, 1)$, $\sigma_\varepsilon = 2$, $N_0 = 10$ donors, $T_0 = 80$ pre-treatment periods, and $T_{\text{post}} = 20$ post-treatment periods. The top row sets $\kappa = 0$ (shared stochastic trend only); the bottom row adds idiosyncratic stochastic trend ($\kappa = 2$). RMSE is computed over post-treatment periods.

In the top-left panel, synthetic control with intercept captures the common factor structure and tracks the treated unit closely in both the pre- and post-treatment periods (RMSE = 2.2). In the top-right panel, first-differencing weakens the dominant common signal; matching on differenced data in the presence of large stationary noise ($\sigma_\varepsilon = 2$) produces weights that recover the common structure less precisely, and the reconstructed level path has a larger discrepancy (RMSE = 6.0).

In the bottom-left panel, synthetic control with intercept shows a large performance discrepancy between pre- and post- treatment periods, suggesting an instance of spurious donor matching (RMSE = 15.3). In the bottom-right panel, first-differencing synthetic control avoids the spurious match and produces a more accurate counterfactual (RMSE = 4.4).

In practice, the researcher does not know how important the idiosyncratic stochastic trend component is relative to the shared component. A method that commits fully to either level matching or hard filtering will fail in one regime or the other. This motivates the need for a *soft* allocation mechanism rather than a binary choice. The goal of this paper is to provide a synthetic control estimator that lets the data determine how much of the stochastic trend variation in the treated unit should be allocated between donor matching and a smooth treated-specific component.

3. Harmonic Synthetic Control

Section 2 showed that synthetic control’s pre-treatment fitting criterion does not distinguish between the shared low-rank component L_{it} and the idiosyncratic stochastic trend R_{it} ; level matching and hard filtering each fail in one regime or the other. To bridge these two regimes, we propose the harmonic synthetic control (HSC) estimator. The construction proceeds in three steps: weight estimation for donor matching, the treated-unit-specific time series forecaster, and the construction of the counterfactual. HSC does not attempt to disentangle L_{it} and R_{it} in the data-generating process. Instead, it seeks the optimal allocation between modeling stochastic trend variation as shared low-rank structure and modeling it as idiosyncratic stochastic trends. A single tuning parameter $\rho \in [0, 1]$ governs such an allocation.

3.1. Donor weights of HSC

We use $q \in \{1, 2\}$ to denote the smoothness order. The difference operator D_q is the q th-order difference operator: D_1 is the $(T_0 - 1) \times T_0$ first-difference operator with rows $(D_1x)_t = x_{t+1} - x_t$, and D_2 is the $(T_0 - 2) \times T_0$ second-difference operator with rows $(D_2x)_t = x_{t+2} - 2x_{t+1} + x_t$.² Let $K_q := D_q' D_q$, which is symmetric positive semidefinite with null space $\text{Null}(K_q)$ equal to $\text{span}\{\mathbf{1}_{T_0}\}$

²Explicitly, D_1 has -1 on the main diagonal and $+1$ on the first superdiagonal; D_2 has entries $+1, -2, +1$ on three consecutive diagonals.

for $q = 1$ and $\text{span}\{\mathbf{1}_{T_0}, t_{\text{pre}}\}$ for $q = 2$, where $t_{\text{pre}} := (1, \dots, T_0)'$. Recall that $X_{\text{pre}} \in \mathbb{R}^{T_0 \times N_0}$ denotes the pre-treatment donor outcome matrix, $Y_{\text{pre}} \in \mathbb{R}^{T_0}$ is the treated unit's pre-treatment outcome vector, and $\Delta_{N_0} := \{\omega \in \mathbb{R}^{N_0} : \omega \geq 0, \mathbf{1}'\omega = 1\}$ is the unit simplex.

Definition 1 (Harmonic Synthetic Control, $\rho \in (0, 1)$). For $\rho \in (0, 1)$, the HSC estimator jointly solves

$$(\hat{\omega}(\rho, q), \hat{E}_{\text{pre}}(\rho, q)) \in \arg \min_{\omega \in \Delta_{N_0}, E \in \mathbb{R}^{T_0}} \left\{ \frac{1}{\rho} \|Y_{\text{pre}} - X_{\text{pre}}\omega - E\|_2^2 + \frac{1}{1-\rho} \|D_q E\|_2^2 + \zeta^2 T_0 \|\omega\|_2^2 \right\}, \quad (2)$$

where $\zeta > 0$ is a ridge regularization parameter.³ The first term penalizes the discrepancy between the treated unit and the donor-weighted combination after removing the latent smooth component E ; the second penalizes the roughness of E through the q th-difference penalty $\|D_q E\|_2^2 = E' K_q E$; the third is a ridge penalty that helps stabilize the donor weights.

D_q determines what counts as a smooth component. When $q = 1$, the penalty $\|D_1 E\|_2^2 = \sum_{t=1}^{T_0-1} (E_{t+1} - E_t)^2$ penalizes local changes in level, so smoother paths are those that vary less from one period to the next. Constant vectors, which are in the null space of K_1 , receive no penalty. When $q = 2$, the penalty $\|D_2 E\|_2^2 = \sum_{t=1}^{T_0-2} (E_{t+2} - 2E_{t+1} + E_t)^2$ penalizes local changes in slope, so smoother paths are those with less curvature. Intercept-plus-linear-trend components, which are in the null space of K_2 , receive no penalty. Thus, for $q = 1$ the smooth component is encouraged to be locally flat in levels, whereas for $q = 2$ it is encouraged to be locally linear in time.

The tuning parameter ρ governs the relative incentives in the joint optimization over (ω, E) . Conditional on donor weights ω , the optimizer chooses E to balance fidelity to the residual $Y_{\text{pre}} - X_{\text{pre}}\omega$ against the smoothness restriction imposed by $\|D_q E\|_2^2$. When ρ is small, the fit term $\frac{1}{\rho} \|Y_{\text{pre}} - X_{\text{pre}}\omega - E\|_2^2$ receives relatively large weight compared with the roughness penalty. Therefore, conditional on a given ω , the optimizer is more willing to let E track a larger and potentially rougher portion of the residual, where roughness is measured by D_q . When ρ is large, the roughness penalty $\frac{1}{1-\rho} \|D_q E\|_2^2$ receives relatively large weight, so conditional on a given ω , the optimizer is

³Following Arkhangelsky et al. (2021), we set the default value of ζ as $T_{\text{post}}^{1/4} \hat{\sigma}$, where $\hat{\sigma}$ is the standard deviation of all elements of the first-differenced donor matrix $D_1 X_{\text{pre}}$. This is the single-treated-unit specialization of the formula $\zeta = (N_{\text{tr}} T_{\text{post}})^{1/4} \hat{\sigma}$ used for multiple treated units.

forced to choose a smoother E , where smoothness is in the sense measured by D_q .

Because ω and E are chosen jointly, the tuning parameter ρ does not act on a fixed pre-treatment discrepancy. Instead, it determines how the joint optimizer splits the treated series Y_{pre} between the donor-matched component $X_{\text{pre}}\hat{\omega}$ and the treated-unit-specific smooth component \hat{E} , with larger ρ forcing \hat{E} to be smoother.

3.2. Profiling and the HSC metric

The joint formulation in Definition 1 is useful for intuition, but the estimator becomes more transparent and computationally tractable after profiling out the treated-unit-specific smooth component E . This yields an equivalent weight-estimation problem in which the pre-treatment residual is measured under a ρ - and q -dependent metric.⁴

For any candidate donor weight vector $\omega \in \Delta_{N_0}$, define the pre-treatment discrepancy/residual as

$$r_{\text{pre}}(\omega) := Y_{\text{pre}} - X_{\text{pre}}\omega. \quad (3)$$

Fix $\rho \in (0, 1)$. For each ω , the inner minimization over E in (2) is a strictly convex quadratic program:

$$\min_{E \in \mathbb{R}^{T_0}} \left\{ \frac{1}{\rho} \|r_{\text{pre}}(\omega) - E\|_2^2 + \frac{1}{1-\rho} \|D_q E\|_2^2 \right\}.$$

To express its solution, let

$$\lambda_\rho := \frac{\rho}{1-\rho}, \quad S_{\rho,q} := (I_{T_0} + \lambda_\rho K_q)^{-1}. \quad (4)$$

Proposition 1 (Profiled representation). Fix $q \in \{1, 2\}$ and $\rho \in (0, 1)$. For every $\omega \in \Delta_{N_0}$, the inner problem in E has the unique minimizer

$$\hat{E}_{\text{pre}}(\omega; \rho, q) = S_{\rho,q} r_{\text{pre}}(\omega). \quad (5)$$

⁴We use the term ‘‘metric’’ informally throughout: $W_{\rho,q}$ is symmetric positive semidefinite (not positive definite), and it annihilates $\text{Null}(K_q)$, so the quadratic form $r'W_{\rho,q}r$ is a seminorm rather than a norm. Residual components in $\text{Null}(K_q)$ contribute zero to the HSC criterion and are handled separately through the smooth component \hat{E}_{pre} ; see the remark after Proposition 2.

Substituting this optimizer back into the criterion yields the profiled objective

$$\hat{\omega}(\rho, q) \in \arg \min_{\omega \in \Delta_{N_0}} \{r_{\text{pre}}(\omega)' W_{\rho, q} r_{\text{pre}}(\omega) + \zeta^2 T_0 \|\omega\|_2^2\}, \quad (6)$$

where

$$W_{\rho, q} := \frac{1}{\rho} (I_{T_0} - S_{\rho, q}), \quad \rho \in (0, 1). \quad (7)$$

Equivalently, the fitted treated-unit-specific smooth component is

$$\hat{E}_{\text{pre}}(\rho, q) = S_{\rho, q} (Y_{\text{pre}} - X_{\text{pre}} \hat{\omega}(\rho, q)). \quad (8)$$

The proof is deferred to Appendix A.1. Proposition 1 shows that donor weight estimation in HSC can be understood through the metric $W_{\rho, q}$, which re-weights the pre-treatment discrepancy r_{pre} in a standard ridge-regularized quadratic program on the simplex. The operator $S_{\rho, q}$ acts as a smoother that extracts the smooth part of \hat{r}_{pre} as the smooth component \hat{E}_{pre} .

We now show that this family of metrics extends continuously to the boundary cases $\rho = 0$ and $\rho = 1$. Define

$$S_{0, q} := I_{T_0}, \quad S_{1, q} := P_{0, q}, \quad (9)$$

$$W_{0, q} := K_q, \quad W_{1, q} := I_{T_0} - P_{0, q}, \quad (10)$$

where $P_{0, q}$ denotes the orthogonal projector onto $\text{Null}(K_q)$.

Proposition 2 (Continuous extension of the HSC metric). For each fixed $q \in \{1, 2\}$:

(i) The interior families satisfy

$$\lim_{\rho \downarrow 0} S_{\rho, q} = I_{T_0}, \quad \lim_{\rho \uparrow 1} S_{\rho, q} = P_{0, q},$$

and

$$\lim_{\rho \downarrow 0} W_{\rho, q} = K_q, \quad \lim_{\rho \uparrow 1} W_{\rho, q} = I_{T_0} - P_{0, q}.$$

Hence the boundary definitions (9) and (10) are the unique continuous extensions of $\{S_{\rho, q}\}$ and $\{W_{\rho, q}\}$ from $(0, 1)$ to $[0, 1]$.

(ii) $W_{\rho, q}$ is symmetric positive semidefinite for every $\rho \in [0, 1]$.

The proof is deferred to Appendix A.1. The key implication of Proposition 2 is that the HSC weight problem extends continuously from the interior $\rho \in (0, 1)$ to the endpoint cases $\rho = 0$ and $\rho = 1$, where the two boundary values correspond to familiar special cases.

At $\rho = 0$, $S_{0,q} = I_{T_0}$ means the smoother assigns the entire residual to the treated-unit-specific “smooth” component; correspondingly, $W_{0,q} = K_q = D'_q D_q$, so the metric measures only the q th-order roughness of the residual:

$$r_{\text{pre}}(\omega)' W_{0,q} r_{\text{pre}}(\omega) = \|D_q r_{\text{pre}}(\omega)\|_2^2.$$

Hence the profiled objective becomes

$$\hat{\omega}(0, q) \in \arg \min_{\omega \in \Delta_{N_0}} \{ \|D_q Y_{\text{pre}} - (D_q X_{\text{pre}}) \omega\|_2^2 + \zeta^2 T_0 \|\omega\|_2^2 \}, \quad (11)$$

that is, synthetic control applied to the q th-differenced outcomes with a ridge penalty.

At $\rho = 1$, because $W_{1,q} = I_{T_0} - P_{0,q}$, the profiled criterion penalizes only the component of the residual orthogonal to $\text{Null}(K_q)$. Using the projection identity $r'(I_{T_0} - P_{0,q})r = \min_{\gamma} \|r - Z_{0,q} \gamma\|_2^2$, where $Z_{0,q}$ is a basis of $\text{Null}(K_q)$, the profiled objective at $\rho = 1$ is equivalent to the simultaneous least-squares fit of donor weights and unregularized null-space coefficients γ . Thus, for $q = 1$, since $\text{Null}(K_1) = \text{span}\{\mathbf{1}_{T_0}\}$, the endpoint estimator is synthetic control with an intercept; for $q = 2$, since $\text{Null}(K_2) = \text{span}\{\mathbf{1}_{T_0}, t_{\text{pre}}\}$, the endpoint estimator is synthetic control with an intercept and a linear trend in time.

By Proposition 2, null-space components of the residual are not tuned by ρ . For every $v \in \text{Null}(K_q)$ and every $\rho \in (0, 1)$, $(I_{T_0} + \lambda_{\rho} K_q)v = v$, so $S_{\rho,q}v = v$ and $W_{\rho,q}v = 0$; the same identities hold at $\rho \in \{0, 1\}$ by definitions. Thus, a constant component of the residual (for $q = 1$) or any intercept-plus-linear-trend component (for $q = 2$) is always absorbed entirely into $\hat{E}_{\text{pre}}(\rho, q)$ and contributes nothing to the donor-matching criterion. The tuning parameter ρ reallocates only the residual components outside $\text{Null}(K_q)$ between donor matching and the smooth component; null-space components are always assigned to the smooth branch.

With these properties at $\rho = 0$ and $\rho = 1$, we can extend the definition of the HSC weight estimation to $\rho \in [0, 1]$.

Definition 2 (Harmonic Synthetic Control, $\rho \in [0, 1]$). For $\rho \in [0, 1]$ and $q \in \{1, 2\}$, define the HSC weight estimator by

$$\hat{\omega}(\rho, q) \in \arg \min_{\omega \in \Delta_{N_0}} \{r_{\text{pre}}(\omega)' W_{\rho, q} r_{\text{pre}}(\omega) + \zeta^2 T_0 \|\omega\|_2^2\}, \quad (12)$$

where $W_{\rho, q}$ is the continuously extended metric family from Proposition 2. The associated treated-unit-specific smooth component is

$$\hat{E}_{\text{pre}}(\rho, q) := S_{\rho, q} \hat{r}_{\text{pre}}(\rho, q), \quad \hat{r}_{\text{pre}}(\rho, q) := Y_{\text{pre}} - X_{\text{pre}} \hat{\omega}(\rho, q), \quad (13)$$

with $S_{\rho, q}$ continuously extended to $[0, 1]$ as in Proposition 2.

This profiled Definition 2 is the HSC weight estimator used throughout the remainder of the paper. Section 4 discusses the interpretation of this metric from the spectral perspective and shows how $W_{\rho, q}$ amplifies or downweights components at different frequencies.

3.3. Forecast operator and the HSC counterfactual

The previous subsection develops the HSC weight estimator $\hat{\omega}(\rho, q)$ and shows that it arises from minimizing the pre-treatment residual norm under the metric $W_{\rho, q}$. However, the donor weights alone do not define the full counterfactual. The profiled representation produces a smooth component $\hat{E}_{\text{pre}}(\rho, q)$, which captures the smooth part of the donor matching residual. To construct a post-treatment counterfactual, this smooth component is extrapolated to post-treatment periods. This term serves a similar function to the bias-correction term in augmented synthetic control (Ben-Michael, Feller and Rothstein, 2021).

To see why a forecasting step is needed, consider the decomposition implied by HSC. For each (ρ, q) , the pre-treatment residual $\hat{r}_{\text{pre}}(\rho, q) := Y_{\text{pre}} - X_{\text{pre}} \hat{\omega}(\rho, q)$ is split by the smoother $S_{\rho, q}$ into two components:

$$\hat{r}_{\text{pre}}(\rho, q) = \underbrace{S_{\rho, q} \hat{r}_{\text{pre}}(\rho, q)}_{\hat{E}_{\text{pre}}(\rho, q)} + \underbrace{(I_{T_0} - S_{\rho, q}) \hat{r}_{\text{pre}}(\rho, q)}_{\hat{u}_{\text{pre}}(\rho, q)}.$$

The first term, $\hat{E}_{\text{pre}}(\rho, q)$, is the treated-unit-specific smooth component: the smooth part of the residual that cannot be explained by the donors. The second term, $\hat{u}_{\text{pre}}(\rho, q)$, is the rough remain-

der, containing the higher-roughness components of the residual. Note that any component of the residual in $\text{Null}(K_q)$ (a constant for $q = 1$, or an intercept-plus-linear-trend component for $q = 2$) is contained in $\hat{E}_{\text{pre}}(\rho, q)$.

The treated unit's pre-treatment outcome therefore admits the three-part decomposition.

$$Y_{\text{pre}} = \underbrace{X_{\text{pre}}\hat{\omega}(\rho, q)}_{\text{donor-matched}} + \underbrace{\hat{E}_{\text{pre}}(\rho, q)}_{\text{smooth}} + \underbrace{\hat{u}_{\text{pre}}(\rho, q)}_{\text{rough remainder}} . \quad (14)$$

In the post-treatment period, the donor-matched component extends to $X_{\text{post}}\hat{\omega}(\rho, q)$ using observed donor outcomes. The rough remainder is the part of the pre-treatment residual that is suppressed by the smoother $S_{\rho, q}$; it is treated as noise and is not carried forward. The smooth component, however, represents a treated-unit-specific component that, if present in the pre-treatment period, is likely to persist. Discarding it would leave a predictable bias in the counterfactual. This motivates the introduction of a forecast operator to extrapolate $\hat{E}_{\text{pre}}(\rho, q)$ into post-treatment periods.

Let $G_q \in \mathbb{R}^{T_{\text{post}} \times T_0}$ be a deterministic linear forecast operator. The HSC counterfactual is defined as

$$\hat{Y}_{\text{post}}(0; \rho, q) := X_{\text{post}}\hat{\omega}(\rho, q) + G_q\hat{E}_{\text{pre}}(\rho, q). \quad (15)$$

The counterfactual thus combines two branches: a donor-matching component, $X_{\text{post}}\hat{\omega}(\rho, q)$, that uses cross-sectional information to predict the treated unit's counterfactual, and a time series forecasting component, $G_q\hat{E}_{\text{pre}}(\rho, q)$, that uses temporal information in the pre-treatment residual to extrapolate the smooth component. Writing $\Pi_{\rho, q} := G_q S_{\rho, q} \in \mathbb{R}^{T_{\text{post}} \times T_0}$ for the composed forecast-smoother, the counterfactual can also be expressed as

$$\hat{Y}_{\text{post}}(0; \rho, q) = X_{\text{post}}\hat{\omega}(\rho, q) + \Pi_{\rho, q}\hat{r}_{\text{pre}}(\rho, q). \quad (16)$$

The forecast operator G_q is treated as a fixed linear map throughout the analysis of donor weights and counterfactual construction. In practice, G_q may be estimated from the pre-treatment data. We impose one structural requirement on G_q .

Definition 3 (Admissible forecast operator). A linear operator $G_q : \mathbb{R}^{T_0} \rightarrow \mathbb{R}^{T_{\text{post}}}$ is an *admissible*

forecast operator of order q if, for every polynomial p of degree less than q ,

$$G_q (p(t))_{t=1}^{T_0} = (p(t))_{t=T_0+1}^{T_0+T_{\text{post}}}. \quad (17)$$

For $q = 1$, the requirement reduces to $G_1 \mathbf{1}_{T_0} = \mathbf{1}_{T_{\text{post}}}$: constants are continued as constants. For $q = 2$, it adds $G_2 (1, 2, \dots, T_0)' = (T_0 + 1, \dots, T_0 + T_{\text{post}})'$: linear trends are continued as linear trends. These are the only cases we use in what follows.

Definition 3 ensures that the forecast operator extrapolates the components which the roughness penalty leaves unpenalized, namely those in $\text{Null}(K_q)$, to the post-treatment period without distortion. The components that pass mechanically into \hat{E} (constants for $q = 1$; constants and linear trends for $q = 2$) are thereby continued unchanged. Since $S_{\rho,q}$ also leaves $\text{Null}(K_q)$ untouched for every $\rho \in [0, 1]$, the composed operator $\Pi_{\rho,q} = G_q S_{\rho,q}$ inherits the same continuation property whenever G_q is admissible.

Definition 3 is a design requirement on the forecast operator, not a property that generic forecasters automatically satisfy. The simplest admissible operators are constant extrapolation (for $q = 1$) and linear extrapolation (for $q = 2$). Constant extrapolation defines $(G_1^{\text{const}} x)_h := x_{T_0}$ for $h = 1, \dots, T_{\text{post}}$: each post-treatment period receives the last pre-treatment value. Then $G_1^{\text{const}} \mathbf{1}_{T_0} = \mathbf{1}_{T_{\text{post}}}$. Linear extrapolation defines $(G_2^{\text{lin}} x)_h := x_{T_0} + h \cdot (x_{T_0} - x_{T_0-1})$ for $h = 1, \dots, T_{\text{post}}$. Then $G_2^{\text{lin}} \mathbf{1}_{T_0} = \mathbf{1}_{T_{\text{post}}}$ and $G_2^{\text{lin}} t_{\text{pre}} = t_{\text{post}}$.

In practice, one may wish to use a richer forecasting model, for example an autoregressive or ARIMA-type specification, to extrapolate $\hat{E}_{\text{pre}}(\rho, q)$. Because such procedures involve parameter estimation, the resulting forecast operator \hat{G}_q is data-dependent and need not be admissible on its own. A convenient way to enforce the requirement is to separate the null-space and non-null-space components of the input.

Recall that $P_{0,q}$ denotes the orthogonal projector onto $\text{Null}(K_q)$, and $P_{\perp,q} := I_{T_0} - P_{0,q}$. Definition 3 constrains a forecast operator only through its action on $\text{Null}(K_q)$. Let G_q^{null} denote the unique admissible action on the null space: it has the property that, for $v \in \text{Null}(K_q)$ equal to $(p(t))_{t=1}^{T_0}$ for the unique polynomial p of degree less than q , $G_q^{\text{null}} v = (p(t))_{t=T_0+1}^{T_0+T_{\text{post}}}$. Construct the

forecast operator

$$\tilde{G}_q := G_q^{\text{null}} P_{0,q} + \hat{G}_q P_{\perp,q}.$$

For every $z \in \text{Null}(K_q)$, $\tilde{G}_q z = G_q^{\text{null}} z$, so Definition 3 holds by construction. For every $z \in \text{Null}(K_q)^\perp$, $\tilde{G}_q z = \hat{G}_q z$, so the data-driven forecaster retains full flexibility on the $\text{Null}(K_q)^\perp$ component. For components in $\text{Null}(K_q)$, G_q^{null} simply lets the constant ($q = 1$) or the linear trend ($q = 2$) persist into the post-treatment periods. These are the carry-forward G_1^{const} and the two-point linear extension G_2^{lin} defined above, respectively.

The tuning parameter ρ determines the content of the smooth component $\hat{E}_{\text{pre}}(\rho, q)$ and therefore what the forecast operator G_q is asked to extrapolate. At $\rho = 1$, the smoother $S_{1,q} = P_{0,q}$ extracts only the null-space component of the residual, and G_q continues these unpenalized components into the post-treatment period. For interior values $\rho \in (0, 1)$, the smooth component absorbs additional variation beyond the null space, and G_q extrapolates these additional components. At $\rho = 0$, the smoother $S_{0,q} = I_{T_0}$ assigns the entire residual to \hat{E}_{pre} , so G_q carries the full pre-treatment discrepancy forward. The choice of ρ thus calibrates the burden on G_q : minimal at $\rho = 1$, where extrapolation amounts to leaving null-space components unchanged, and maximal at $\rho = 0$, where the entire residual must be forecast.

4. Spectral Interpretation and Tuning

The previous section defined the HSC estimator and derived its profiled representation. We now develop the complementary perspective on this allocation. The metric $W_{\rho,q}$ acts as a frequency-dependent gain function, so ρ determines which frequency components of Y_{pre} enter the donor-matching criterion and which are diverted to the time series forecaster. We use cross-validation to select ρ by minimizing out-of-sample prediction error. We then illustrate the resulting adaptation using the simulated data introduced in Section 2.

4.1. Spectral decomposition of the HSC metric

The previous section showed that ρ controls a smooth allocation of Y_{pre} between donor matching and the time series forecaster. We now examine the complementary question: how does ρ shape the donor-matching criterion? The spectral decomposition of $W_{\rho,q}$ provides a precise answer and reveals that the key difference between HSC and existing synthetic control methods lies in how each method weights different frequency components in the optimization criterion.

Since the penalty matrix $K_q = D_q^\top D_q$ is symmetric positive semidefinite, \mathbb{R}^{T_0} admits an orthonormal basis of eigenvectors of K_q , denoted $v_{1,q}, \dots, v_{T_0,q}$, with corresponding eigenvalues $0 \leq \mu_{1,q} \leq \dots \leq \mu_{T_0,q}$. Any vector of length T_0 can be written as a linear combination of these eigenvectors. Each eigenvalue $\mu_{j,q}$ measures the roughness of the corresponding basis function as assessed by the q th-difference penalty: $\mu_{j,q} = v_{j,q}' K_q v_{j,q} = \|D_q v_{j,q}\|_2^2$. The first q eigenvectors span the null space $\text{Null}(K_q)$, corresponding to constants when $q = 1$ and constants and linear trends when $q = 2$, with $\mu_{j,q} = 0$. As the index j increases beyond q , the eigenvectors oscillate progressively more rapidly and $\mu_{j,q}$ grows.⁵ Small $\mu_{j,q}$ corresponds to low-frequency variation, such as slow-moving trends and long cycles, while large $\mu_{j,q}$ corresponds to high-frequency variation, including rapid, short-run oscillations.

For a residual vector $r_{\text{pre}}(\omega)$, define its spectral coordinates by $\tilde{r}_j(\omega) := v_{j,q}' r_{\text{pre}}(\omega)$, the coefficient on the j -th eigenvector. One can thus write $r_{\text{pre}}(\omega) = \sum_{j=1}^{T_0} \tilde{r}_j(\omega) v_{j,q}$. In these coordinates, the smoother $S_{\rho,q}$ and the profiled metric $W_{\rho,q}$ each act componentwise through scalar functions of the eigenvalue μ :

$$S_{\rho,q} r_{\text{pre}}(\omega) = \sum_{j=1}^{T_0} \underbrace{\frac{1 - \rho}{(1 - \rho) + \rho \mu_{j,q}}}_{=: s_q(\mu_{j,q}; \rho)} \tilde{r}_j(\omega) v_{j,q}, \quad (18)$$

$$r_{\text{pre}}(\omega)' W_{\rho,q} r_{\text{pre}}(\omega) = \sum_{j=1}^{T_0} \underbrace{\frac{\mu_{j,q}}{(1 - \rho) + \rho \mu_{j,q}}}_{=: w_q(\mu_{j,q}; \rho)} \tilde{r}_j(\omega)^2. \quad (19)$$

The shrinkage function $s_q(\mu; \rho)$ is decreasing in μ : smoother components (small μ) in $r_{\text{pre}}(\omega)$

⁵For $q = 1$, the eigenvalues admit the closed form $\mu_{j,1} = 4 \sin^2((j-1)\pi/(2T_0))$ for $j = 1, \dots, T_0$. For $q = 2$, the eigenvalue spectrum grows more steeply, as illustrated in Figure 3(a).

are less shrunk toward zero than rougher components (larger μ). Components in $\text{Null}(K_q)$ ($\mu = 0$) survive intact. The weight function $w_q(\mu; \rho)$ is increasing in μ : rougher components in $r_{\text{pre}}(\omega)$ receive more emphasis in the donor-matching problem. Components in $\text{Null}(K_q)$ ($\mu = 0$) are completely excluded from the donor-matching problem. From this spectral perspective, HSC therefore routes low-frequency discrepancy primarily to the time series branch and high-frequency discrepancy primarily to the donor-matching branch.

Figure 3 displays these two functions and their consequences for the simulated pre-treatment series introduced in Section 2, with $q = 1$ on the left and $q = 2$ on the right. We highlight three features of the spectral decomposition.

First, Panel (a) plots the shrinkage function $s_q(\mu; \rho)$ for five values of ρ . This function determines how much of each spectral coordinate of the pre-treatment residual is retained in the smooth component $\hat{E}_{\text{pre}}(\rho, q)$. For $\rho \in (0, 1)$, each curve equals one at $\mu = 0$ (null-space components are fully retained) and decays smoothly toward zero as μ increases, with smaller ρ producing slower decay. At $\rho = 0$, the shrinkage function equals one everywhere: the entire residual is assigned to \hat{E}_{pre} and extrapolated by G_q . At $\rho = 1$, the function collapses to the null-space indicator, $s_q(\mu; 1) = \mathbf{1}\{\mu = 0\}$. Intermediate ρ values interpolate smoothly between these extremes.

Second, Panel (b) plots the complementary weight function $w_q(\mu; \rho)$, which determines how much of each spectral coordinate enters the donor-matching criterion (6). Every curve passes through $(\mu, w) = (1, 1)$: components with $\mu > 1$ are amplified relative to uniform weighting, components with $\mu < 1$ are shrunk. At $\rho = 0$, $w_q(\mu; 0) = \mu$ (the 45-degree line), so the profiled metric reduces to K_q and donors are matched entirely in q th differences. At $\rho = 1$, $w_q(\mu; 1) = \mathbf{1}\{\mu > 0\}$ (the horizontal line), so all components outside $\text{Null}(K_q)$ are retained intact in the donor-matching criterion, while the null-space directions are absorbed by \hat{E}_{pre} . The $\rho = 1$ endpoint thus coincides with SC with intercept at $q = 1$ and with SC with intercept-plus-linear-trend at $q = 2$.

Third, the eigenvalue ranges of K_1 and K_2 differ substantially. For $q = 1$, the eigenvalues of K_1 lie in $[0, 4]$ when $T_0 = 80$, whereas for $q = 2$ the eigenvalues of K_2 span a much wider range (up to roughly 16). Under the same ρ , the wider spectrum therefore yields more extreme amplification of rough components in the sense of K_2 than in the sense of K_1 in the donor-matching criterion.

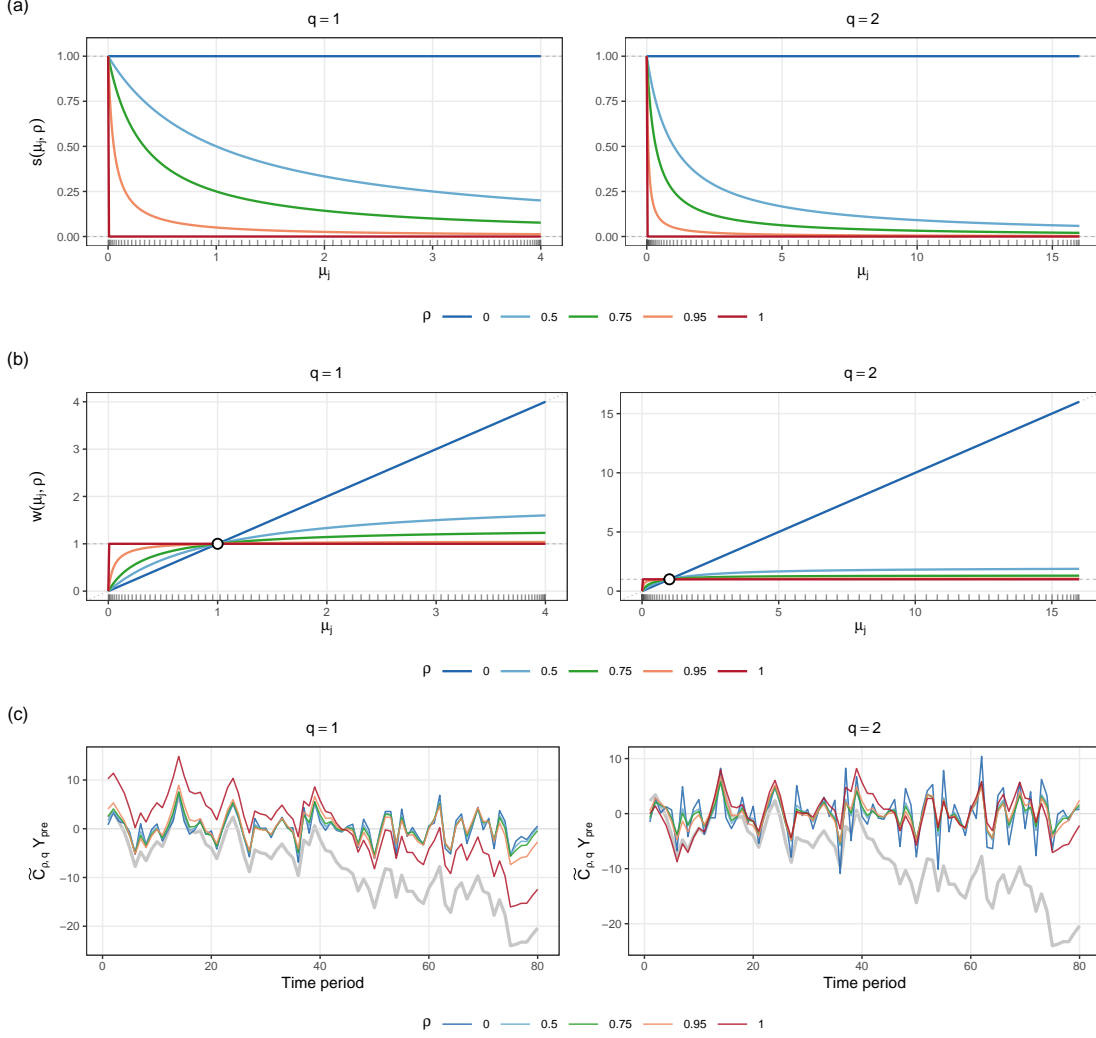


Figure 3. SPECTRAL INTERPRETATION OF THE HSC OPERATORS $S_{\rho,q}$ AND $W_{\rho,q}$.

Note: This figure illustrates the spectral reweighting mechanism of HSC with $T_0 = 80$. Panel (a) plots the shrinkage function $s_q(\mu; \rho) = (1 - \rho) / ((1 - \rho) + \rho\mu)$, which determines how much of each spectral coordinate is retained in the smooth component \hat{E}_{pre} . Panel (b) plots the weight function $w_q(\mu; \rho) = \mu / ((1 - \rho) + \rho\mu)$, which determines how much of each spectral coordinate enters the donor-matching criterion. Both panels display five values $\rho \in \{0, 0.5, 0.75, 0.95, 1\}$, with $q = 1$ (left) and $q = 2$ (right). Rug marks along the horizontal axis show the positive eigenvalues of K_q . In panel (b), the open circle marks the fixed point $(\mu, w) = (1, 1)$ through which all curves pass; the dashed line at $w = 1$ corresponds to null-space-projected weighting ($\rho = 1$); the dotted 45-degree line corresponds to pure differencing ($\rho = 0$). Panel (c) displays the spectrally transformed pre-treatment series $\tilde{C}_{\rho,q} Y_{\text{pre}}$ for the same five values of ρ , with $q = 1$ (left) and $q = 2$ (right). The grey line shows the raw pre-treatment series Y_{pre} of the treated unit from the shared + idiosyncratic stochastic trend regime ($\kappa = 2$) of Figure 2. At $\rho = 1$, the transformation removes the null-space component (mean for $q = 1$; mean and linear trend for $q = 2$) and weights all remaining directions equally. At $\rho = 0$, the transformation applies $K_q^{1/2}$, amplifying high-roughness directions; this effect is particularly visible for $q = 2$, where the wider eigenvalue range of K_2 produces a noticeably rougher transformed series. Intermediate values of ρ blend these effects, progressively attenuating trends while preserving moderate-scale variation.

Because $W_{\rho,q}$ is symmetric positive semidefinite, it admits a symmetric square root $\tilde{C}_{\rho,q} := W_{\rho,q}^{1/2} = V_q \text{diag}(\sqrt{w_q(\mu_{j,q}; \rho)}) V_q'$, where $V_q := (v_{1,q}, \dots, v_{T_0,q})$ is the orthogonal matrix of eigenvectors introduced above. The donor-matching problem can equivalently be written as

$$\hat{\omega}(\rho, q) \in \arg \min_{\omega \in \Delta_{N_0}} \left\{ \|\tilde{C}_{\rho,q} r_{\text{pre}}(\omega)\|_2^2 + \zeta^2 T_0 \|\omega\|_2^2 \right\}.$$

The transformed series $\tilde{C}_{\rho,q} Y_{\text{pre}}$ makes the effect of ρ on the data visible. Panel (c) of Figure 3 plots this transformation for the treated unit from the shared + idiosyncratic stochastic trend regime ($\kappa = 2$) of Figure 2, at five values of ρ .

In the $q = 1$ panel, at $\rho = 1$, the transformation projects out the constant direction and retains all other components with equal weight; the result resembles a demeaned version of Y_{pre} . At $\rho = 0$, the transformation reduces to $K_1^{1/2}$, which has the same quadratic form as the first-difference operator ($\|K_1^{1/2} r\|_2^2 = \|D_1 r\|_2^2$): slow trends are strongly attenuated and period-to-period oscillations are amplified. At $\rho \in \{0.5, 0.75, 0.95\}$, low-frequency components are progressively attenuated while high-frequency components are increasingly amplified. The $q = 2$ panel exhibits the same pattern with sharper contrast. At $\rho = 1$, the transformation projects out both the constant and linear-trend directions. At $\rho = 0$, it applies $K_2^{1/2}$, which has the same quadratic form as the second-difference operator: the transformed series is visibly rougher than the raw data because rapid oscillations that contribute little to the original amplitude are greatly amplified.

The name ‘‘harmonic’’ reflects the spectral structure of HSC. The weight $w_q(\mu; \rho) = \mu / ((1 - \rho) + \rho\mu)$ admits the decomposition

$$\frac{1}{w_q(\mu; \rho)} = (1 - \rho) \cdot \frac{1}{\mu} + \rho \cdot 1,$$

which identifies $w_q(\mu; \rho)$ as the weighted harmonic mean of μ and 1 with weights $(1 - \rho)$ and ρ . The two endpoints recover the arguments themselves: $w_q(\mu; 0) = \mu$ and $w_q(\mu; 1) = \mathbf{1}\{\mu > 0\}$. This structure mirrors the coefficients $1/\rho$ and $1/(1 - \rho)$ on the smoothness and residual terms in the primal objective (2). Because the harmonic mean is dominated by the smaller of its arguments, $w_q(\mu; \rho)$ is small whenever either μ is small (a low-frequency, near-null-space component) or ρ is small (the user has shifted emphasis toward \hat{E}_{pre}), giving the metric its characteristic soft cutoff.

4.2. Selection of ρ

The central tuning decision in HSC is how to allocate low-frequency components of the pre-treatment discrepancy between donor matching and the smooth component \hat{E}_{pre} . We select ρ by rolling-origin cross-validation using *only pre-treatment data of the treated unit*:⁶ at each fold, HSC is fitted on a shortened training window and used to predict held-out pre-treatment outcomes, and the ρ minimizing average prediction error is selected. This mimics the forecasting task the estimator faces at the treatment date.

The cross-validation procedure requires the researcher to specify four inputs: the smoothness order $q \in \{1, 2\}$, the forecast operator G_q , a forecast horizon $h \geq 1$, and a number of folds $L \geq 1$. The rolling forecast origins are then $k_\ell = T_0 - h - L + \ell$ for $\ell = 1, \dots, L$; by construction, $k_L + h = T_0$, so all validation windows lie within the pre-treatment period and no post-treatment data are used. At each origin k_ℓ , the training window is $\{1, \dots, k_\ell\}$ and the validation window is $\{k_\ell + 1, \dots, k_\ell + h\}$. For each candidate ρ and each origin k_ℓ , the procedure (i) re-estimates the HSC weights $\hat{\omega}(\rho, q)$ and the smooth component $\hat{E}_{\text{pre}}(\rho, q)$ on the training window, (ii) refits any data-dependent parameters of G_q on the training window (for instance, the coefficients of an ARIMA specification), (iii) constructs the counterfactual forecast $\hat{Y}_{k_\ell+s}(0; \rho, q)$ for the validation window by combining the donor-matched component with the G_q -extrapolated smooth component, and (iv) computes the squared prediction errors against the actual outcomes $Y_{k_\ell+1}, \dots, Y_{k_\ell+h}$. Because all quantities are re-estimated within each fold, the validation error is an out-of-sample measure of the joint performance of donor matching and time series extrapolation. The cross-validation criterion is

$$\text{CV}(\rho) = \frac{1}{Lh} \sum_{\ell=1}^L \sum_{s=1}^h (Y_{k_\ell+s} - \hat{Y}_{k_\ell+s}(0; \rho, q))^2, \quad (20)$$

where $\hat{Y}_{k_\ell+s}(0; \rho, q)$ denotes the HSC counterfactual prediction for period $k_\ell + s$ constructed from the training window $\{1, \dots, k_\ell\}$.

One practical consideration in constructing the candidate grid is worth noting. The equivalent

⁶Each unit may carry its own idiosyncratic stochastic trend, so the ρ that minimizes prediction error on a control unit need not be appropriate for the treated unit. We therefore restrict cross-validation to the treated unit's own pre-treatment history.

smoothing parameter $\lambda_\rho = \rho/(1 - \rho)$ is a convex function of ρ that increases slowly near $\rho = 0$ but diverges as $\rho \uparrow 1$. Consequently, a uniformly spaced grid in ρ induces a nonuniform grid in λ_ρ , with increasingly coarse coverage on the λ_ρ scale near $\rho = 1$. When the cross-validation curve exhibits dramatic change near $\rho = 1$, a convenient alternative is to construct the grid on a logarithmic scale in λ_ρ and map back via $\rho = \lambda_\rho/(1 + \lambda_\rho)$, while retaining the boundary $\rho = 0$ and $\rho = 1$ explicitly.

Beyond the choice of ρ , the same procedure can also be used to select (ρ, q) jointly by minimizing $\text{CV}(\rho, q)$ over the pair. If multiple forecast operators are under consideration, the grid extends further to (ρ, q, G_q) triples, comparing, for example, constant extrapolation against an ARIMA specification for each (ρ, q) combination. Joint selection remains computationally inexpensive because the quadratic program for each (ρ, q, k_ℓ) combination is fast to solve.⁷

4.3. An illustrative example

We illustrate HSC on the two simulated regimes from Section 2. Two configurations vary both the smoothness order q and the forecast operator G_q to show the roles of all three tuning choices (ρ , q , and G_q). In both configurations, ρ is selected by the rolling-origin cross-validation procedure of Section 4.2 with one-step-ahead horizon ($h = 1$), 10 folds ($L = 10$), and a grid of 21 equally spaced values in $[0, 1]$.

Configuration 1: $q = 1$, constant extrapolation. The first configuration sets $q = 1$ and uses the constant-extrapolation operator G_1^{const} , the most conservative admissible forecaster: each post-treatment period receives the last pre-treatment value of \hat{E}_{pre} .

Figure 4 displays the results. Each row corresponds to one regime: shared stochastic trend ($\kappa = 0$, top) and shared + idiosyncratic stochastic trend ($\kappa = 2$, bottom). The three columns show the cross-validation curve, the counterfactual fit, and the decomposition of the fitted counterfactual into its donor-matched and time series components.

In the regime with only shared stochastic trend, cross-validation selects $\hat{\rho} = 1$, the endpoint corresponding to SC with intercept. This is consistent with the spectral interpretation of Section 4.1: when the stochastic trend factor is shared across all units, the donor pool can reproduce

⁷Our implementation uses Gurobi.

the treated unit’s low-frequency dynamics, so HSC lets the donor-matching branch carry most of the load in modeling the treated series. The decomposition panel confirms this allocation: the donor component $X_{\text{post}}\hat{\omega}$ (green) almost coincides with the counterfactual $\hat{Y}_{\text{post}}(0)$ (blue), while the extrapolated smooth component $G_1^{\text{const}}\hat{E}_{\text{pre}}$ (red) is a flat horizontal line.

In the regime with both shared and idiosyncratic stochastic trends, cross-validation selects $\hat{\rho} = 0$. The donor pool can no longer reproduce the treated unit’s idiosyncratic stochastic trend, so cross-validation finds that matching entirely in first differences, with the time series branch carrying more of the prediction, yields the best out-of-sample predictions. The decomposition panel reflects this: the extrapolated smooth component $G_1^{\text{const}}\hat{E}_{\text{pre}}$ now carries a large level correction that accounts for the drift accumulated up to T_0 . In this regime, HSC reduces to ridge-regularized synthetic control in first differences, anchored at T_0 , as shown in Section 2.

The contrast between $\hat{\rho} = 1$ and $\hat{\rho} = 0$ provides a sharp demonstration of the adaptive mechanism of HSC: the same estimator with the same tuning procedure selects the two extreme endpoints of the ρ continuum, recovering pure level matching when the stochastic trend is shared and pure differencing when the drift is partly idiosyncratic, precisely the regime-dependent behavior that Section 2 argues is needed.

Configuration 2: $q = 2$, ARIMA forecast. The second configuration sets $q = 2$ and uses an ARIMA(1,1,0) model as the data-driven forecaster \hat{G}_q within the null-space separation construction of Section 3.3. Definition 3 is satisfied by design: the null-space component of \hat{E}_{pre} (which now includes both an intercept and a linear trend) is extrapolated by the canonical linear forecaster G_2^{lin} , while the non-null-space component is extrapolated by an ARIMA model.

Figure 5 displays the results in the same format as Figure 4. In the shared stochastic trend regime, cross-validation again selects $\hat{\rho} = 1$. As in Configuration 1, the donor pool suffices to match the treated unit’s dynamics, and the time series forecaster plays a minimal role. The post-treatment RMSE (2.7) is comparable to Configuration 1 (2.6).

In the regime with both shared and idiosyncratic stochastic trends, cross-validation selects $\hat{\rho} = 0.33$. The decomposition panel reveals that the smooth component \hat{E}_{pre} exhibits a clear downward trend in the pre-treatment period, and the ARIMA forecaster extrapolates this trend

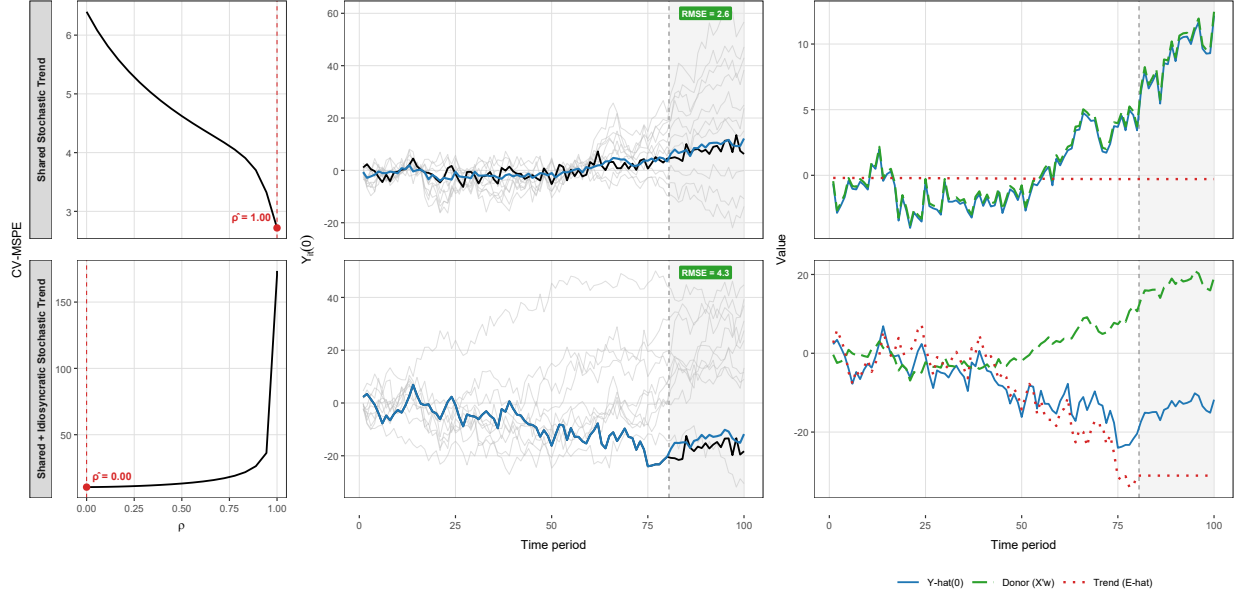


Figure 4. HSC WITH $q = 1$ AND CONSTANT EXTRAPOLATION, APPLIED TO THE TWO SIMULATED REGIMES OF SECTION 2.

Note: Each row corresponds to one DGP regime from Section 2: shared stochastic trend ($\kappa = 0$, top) and shared + idiosyncratic stochastic trend ($\kappa = 2$, bottom). The DGP parameters and seed are identical to those in Figure 2. HSC is estimated with smoothness order $q = 1$ and constant extrapolation forecast operator G_1^{const} ; the tuning parameter ρ is selected by rolling-origin cross-validation (Section 4.2) with one-step-ahead horizon $h = 1$. *Left column:* Cross-validation MSPE as a function of ρ . The red point and dashed vertical line mark the selected $\hat{\rho}$. *Middle column:* Counterfactual fit. The black line is the treated unit’s outcome $Y_{1t}(0)$; grey lines are donor units; the blue line is the HSC counterfactual $\hat{Y}_t(0; \hat{\rho}, 1)$. The shaded region marks the post-treatment window ($t > T_0$), and the green label reports the post-treatment RMSE. *Right column:* Decomposition of the HSC counterfactual for the treated unit. The blue line is the counterfactual $\hat{Y}_t(0) = X_t' \hat{\omega} + \hat{E}_t$ (identical to the middle column); the green dashed line is the donor-matched component $X_t' \hat{\omega}$; the red dotted line is the extrapolated smooth component \hat{E}_t .

into the post-treatment window. This trending extrapolation is visible in the red dotted line, which continues to decline after T_0 rather than remaining flat as in Figure 4. As a result, less of the idiosyncratic drift needs to be absorbed by the level shift alone, and the post-treatment RMSE improves from 4.3 to 3.4.⁸

This comparison highlights the complementary roles of the three tuning choices. The tuning parameter ρ controls how much of the pre-treatment discrepancy is allocated to each branch. The forecast operator G_q determines how the smooth component is extrapolated. The smoothness order q determines what counts as “smooth”. Across both configurations, the cross-validation procedure adapts ρ to the data-generating regime.

⁸The small RMSE difference (4.3 vs. 4.4) between Configuration 1 at $\hat{\rho} = 0$ and the unregularized first-differenced SC of Figure 2 reflects the ridge term $\zeta^2 T_0 \|\omega\|_2^2$.

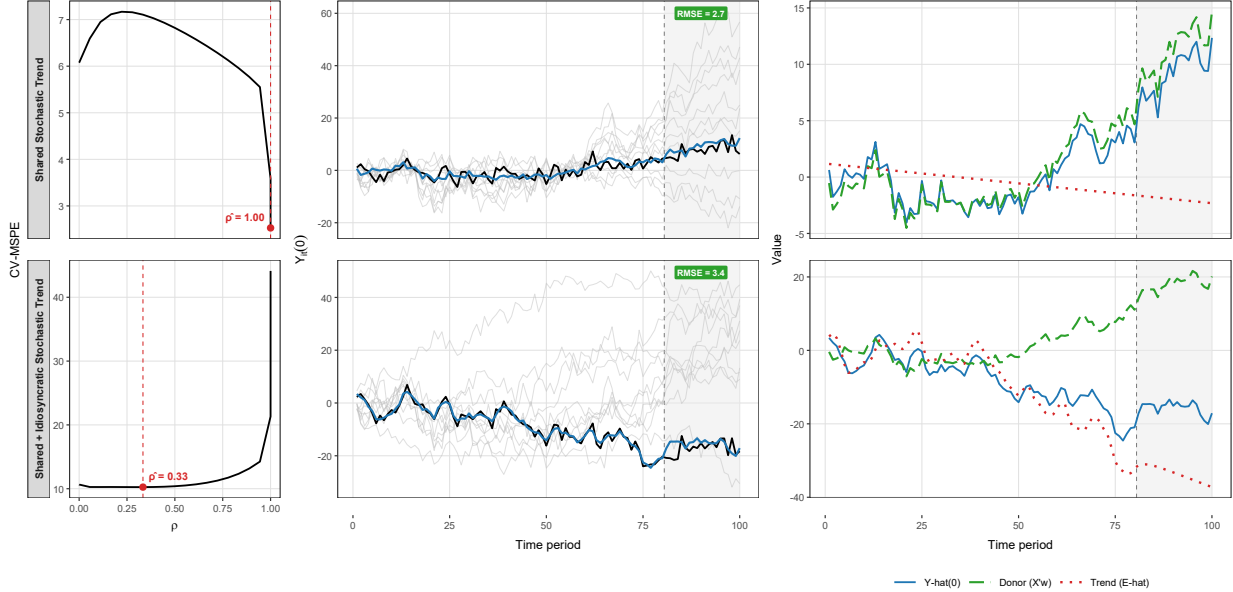


Figure 5. HSC with $q = 2$ AND ARIMA(1,1,0) FORECAST, APPLIED TO THE TWO SIMULATED REGIMES OF SECTION 2.

Note: Same DGP and format as Figure 4, but with smoothness order $q = 2$ and an ARIMA(1,1,0) forecast. The second-order penalty penalizes changes in slope, so the null space of K_2 includes both intercept and linear trend components. In the shared stochastic trend regime (top row), cross-validation again selects $\hat{\rho} = 1$, and the results are similar to Figure 4. In the shared + idiosyncratic stochastic trend regime (bottom row), cross-validation selects the interior value $\hat{\rho} = 0.33$. The decomposition panel shows that the smooth component \hat{E}_t (red dotted line) exhibits a trending pattern that the ARIMA forecaster extrapolates beyond T_0 , unlike the flat carry-forward in Figure 4. This trending extrapolation improves the post-treatment RMSE from 4.3 (Figure 4) to 3.4.

5. Prediction-Error Decomposition

Having established the HSC estimator and its spectral interpretation, we now develop a formal decomposition of the counterfactual prediction error. This decomposition separates the prediction error into a *weight-estimation* component, which captures the discrepancy introduced by estimating donor weights from observed outcomes rather than from the underlying shared structure, and a *forecasting* component, which captures the prediction error that would remain even with oracle weights. Each component depends on ρ , and their interplay provides a formal decomposition that helps interpret the adaptive ρ -selection illustrated in Section 4.3.

Throughout this section we fix $q \in \{1, 2\}$ and suppress the q -subscript when no ambiguity arises, writing $K = K_q$, $S_\rho = S_{\rho,q}$, $W_\rho = W_{\rho,q}$, $P_0 = P_{0,q}$, and $P_\perp = I_{T_0} - P_{0,q}$. We use the null-space-separated forecast operator $\tilde{G}_q = G_q^{\text{null}} P_0 + \hat{G}_q P_\perp$ constructed in Section 3.3 and write $\Pi_\rho := \tilde{G}_q S_\rho$

for the composed operator. Since S_ρ leaves $\text{Null}(K)$ components intact and \tilde{G}_q continues $\text{Null}(K)$ components to post-treatment periods (Definition 3), the composed operator inherits the null-space continuation property:

$$\Pi_\rho v = G_q^{\text{null}} v \quad \text{for every } v \in \text{Null}(K). \quad (21)$$

5.1. Outcome model and oracle benchmark

We connect the prediction error to the data-generating structure discussed in Section 2. Recall from Section 2.2 the decomposition $Y_{it}(0) = L_{it} + R_{it} + \varepsilon_{it}$, where L_{it} denotes the shared component that provides the signal for donor matching, R_{it} is an idiosyncratic stochastic trend, and ε_{it} is idiosyncratic short-run noise. For the prediction-error analysis, we work with the two-component grouping

$$Y_{it}(0) = L_{it} + \mathcal{R}_{it}, \quad (22)$$

where $\mathcal{R}_{it} := R_{it} + \varepsilon_{it}$ collects all components not explained by the shared component.⁹

Define donor and treated stacks for L and \mathcal{R} analogously to X_{pre} and Y_{pre} :

$$X_{\text{pre}} = L_{0,\text{pre}} + \mathcal{R}_{0,\text{pre}}, \quad Y_{\text{pre}} = L_{1,\text{pre}} + \mathcal{R}_{1,\text{pre}}, \quad X_{\text{post}} = L_{0,\text{post}} + \mathcal{R}_{0,\text{post}}, \quad Y_{\text{post}}(0) = L_{1,\text{post}} + \mathcal{R}_{1,\text{post}}.$$

We compare the HSC estimator against an oracle that observes the signal L directly and solves the $\rho = 1$ HSC program on L (with the null space projected out):¹⁰

$$\omega^{\text{oracle}} \in \arg \min_{\omega \in \Delta_{N_0}} \left\{ \|P_\perp(L_{1,\text{pre}} - L_{0,\text{pre}}\omega)\|_2^2 + \zeta^2 T_0 \|\omega\|_2^2 \right\}, \quad (23)$$

where P_\perp projects onto $\text{Null}(K)^\perp$, removing an intercept ($q = 1$) or an intercept and linear trend ($q = 2$). This is the same quadratic program as the $\rho = 1$ endpoint of HSC (Definition 2 with $W_{1,q} = P_\perp$), but on the shared component L rather than the observed outcome $Y = L + \mathcal{R}$. The oracle is treated as a fixed benchmark throughout the analysis.

⁹The grouping $\mathcal{R}_{it} = R_{it} + \varepsilon_{it}$ is adopted for analytical convenience: the prediction-error decomposition distinguishes between the shared component L and everything else, regardless of whether that remainder is short-run noise or a stochastic trend. The persistence structure of \mathcal{R}_{it} matters for the spurious matching channel of Term A (Section 5.3).

¹⁰The oracle uses the same ridge parameter ζ as the HSC estimator. This ensures that the oracle benchmark is not trivially superior due to different regularization, so the decomposition isolates the effects of observing Y rather than L and of using W_ρ rather than P_\perp .

5.2. The prediction-error decomposition

Recall from (16) that the HSC counterfactual at any ρ takes the form $\hat{Y}_{\text{post}}(0; \rho, q) = X_{\text{post}}\hat{\omega}(\rho, q) + \Pi_{\rho} r_{\text{pre}}(\hat{\omega}(\rho, q))$, where $r_{\text{pre}}(\omega) := Y_{\text{pre}} - X_{\text{pre}}\omega$ is the pre-treatment residual. We decompose the prediction error by introducing an oracle predictor that replaces the estimated weights with ω^{oracle} but retains the same ρ -dependent smoother and forecaster:

$$\tilde{Y}_{\text{post}}^{\text{oracle}}(0; \rho) := X_{\text{post}}\omega^{\text{oracle}} + \Pi_{\rho} r_{\text{pre}}^{\text{oracle}}, \quad (24)$$

where $r_{\text{pre}}^{\text{oracle}} := Y_{\text{pre}} - X_{\text{pre}}\omega^{\text{oracle}}$ is the oracle pre-treatment residual. Adding and subtracting $\tilde{Y}_{\text{post}}^{\text{oracle}}(0; \rho)$ in the prediction error yields:

Proposition 3 (Prediction-error decomposition). For every $\rho \in [0, 1]$,

$$\underbrace{Y_{\text{post}}(0) - \hat{Y}_{\text{post}}(0; \rho, q)}_{\text{prediction error}} = \underbrace{(\tilde{Y}_{\text{post}}^{\text{oracle}}(0; \rho) - \hat{Y}_{\text{post}}(0; \rho, q))}_{\text{Term A}(\rho) \text{ (weight estimation)}} + \underbrace{(Y_{\text{post}}(0) - \tilde{Y}_{\text{post}}^{\text{oracle}}(0; \rho))}_{\text{Term B}(\rho) \text{ (forecasting)}}. \quad (25)$$

The two terms admit the closed forms

$$\text{Term A}(\rho) = (X_{\text{post}} - \Pi_{\rho}X_{\text{pre}})(\omega^{\text{oracle}} - \hat{\omega}(\rho, q)), \quad (26)$$

$$\text{Term B}(\rho) = (Y_{\text{post}}(0) - X_{\text{post}}\omega^{\text{oracle}}) - \Pi_{\rho}(Y_{\text{pre}} - X_{\text{pre}}\omega^{\text{oracle}}). \quad (27)$$

The derivation given in Appendix A.2 uses only the linearity of $r_{\text{pre}}(\omega)$ in ω and the linearity of Π_{ρ} .

Term A isolates the cost of using the estimated weights $\hat{\omega}(\rho, q)$ rather than the oracle weights ω^{oracle} in post-treatment periods. The weight discrepancy $\omega^{\text{oracle}} - \hat{\omega}(\rho, q)$ is transferred into prediction error through the donor-forecast residual matrix $C_{\rho} := X_{\text{post}} - \Pi_{\rho}X_{\text{pre}}$, whose column j is the forecast residual when the composed operator Π_{ρ} extrapolates donor j from the pre-treatment to the post-treatment period. The subtracted term $\Pi_{\rho}X_{\text{pre}}$ appears because the donor weights enter the counterfactual twice, directly through the post-treatment donor block $X_{\text{post}}\omega$ and indirectly through the pre-treatment residual $r_{\text{pre}}(\omega) = Y_{\text{pre}} - X_{\text{pre}}\omega$ that Π_{ρ} extrapolates forward. Term A therefore depends on ρ through both the estimated weights and C_{ρ} .

Term B is the prediction error that would remain even if the oracle weights were available. It measures how accurately the composed operator Π_{ρ} extrapolates, from the pre-treatment to the

post-treatment period, the discrepancy between the treated unit and its oracle synthetic counterfactual, where the oracle weights are those defined by the shared component L . Term B depends on ρ through the smoother S_ρ embedded in Π_ρ , which controls how much of the pre-treatment oracle residual is passed to the forecaster and how much is discarded.

5.3. Weight-estimation error: three channels of distortion

We now characterize the Term A cost by identifying three distinct channels through which the weight discrepancy $\omega^{\text{oracle}} - \hat{\omega}(\rho, q)$ arises.

The estimated weights $\hat{\omega}(\rho, q)$ and the oracle weights ω^{oracle} minimize different objectives over the same constraint set Δ_{N_0} . The profiled HSC objective (Definition 2) is

$$F_\rho(\omega) := r_{\text{pre}}(\omega)' W_\rho r_{\text{pre}}(\omega) + \zeta^2 T_0 \|\omega\|_2^2, \quad (28)$$

while the oracle objective (23) is

$$H^{\text{oracle}}(\omega) := \|P_\perp(L_{1,\text{pre}} - L_{0,\text{pre}}\omega)\|_2^2 + \zeta^2 T_0 \|\omega\|_2^2. \quad (29)$$

These two objectives share the same ridge penalty but differ in two ways. First, the *metric*: HSC evaluates the pre-treatment residual under W_ρ , whereas the oracle uses P_\perp . The two coincide only at $\rho = 1$ (where $W_\rho = P_\perp$). Second, the *data*: HSC observes $X_{\text{pre}} = L_{0,\text{pre}} + \mathcal{R}_{0,\text{pre}}$ and $Y_{\text{pre}} = L_{1,\text{pre}} + \mathcal{R}_{1,\text{pre}}$, whereas the oracle operates on the signal L alone. The weight discrepancy $\omega^{\text{oracle}} - \hat{\omega}(\rho, q)$ reflects the combined effect of these two differences.

To separate the contributions of L and \mathcal{R} to the weight discrepancy, we decompose the oracle residual by component. For each $Z \in \{L, \mathcal{R}\}$, define $e_{\text{pre}}^Z := Z_{1,\text{pre}} - Z_{0,\text{pre}}\omega^{\text{oracle}} \in \mathbb{R}^{T_0}$, so that $r_{\text{pre}}^{\text{oracle}} = e_{\text{pre}}^L + e_{\text{pre}}^{\mathcal{R}}$ by additivity (22). The signal residual e_{pre}^L contains a null-space component $P_0 e_{\text{pre}}^L \in \text{Null}(K)$ that the oracle objective does not use, and a complement $P_\perp e_{\text{pre}}^L \in \text{Null}(K)^\perp$ that the oracle directly minimizes. Since both W_ρ and P_\perp annihilate $\text{Null}(K)$ components, we have $(W_\rho - P_\perp) P_\perp e_{\text{pre}}^L = (W_\rho - P_\perp) e_{\text{pre}}^L$ and $W_\rho P_\perp e_{\text{pre}}^L = W_\rho e_{\text{pre}}^L$.

The following proposition bounds $\|\text{Term A}(\rho)\|_2$ by three interpretable components that correspond to the metric difference, the data difference, and their interaction. Define the bound

components

$$A_1(\rho) := \frac{1}{T_0} \|L'_{0,\text{pre}}(W_\rho - P_\perp) e_{\text{pre}}^L\|_{Q_\rho^{-1}}, \quad (30)$$

$$A_2(\rho) := \frac{1}{T_0} \|\mathcal{R}'_{0,\text{pre}} W_\rho e_{\text{pre}}^L\|_{Q_\rho^{-1}}, \quad (31)$$

$$A_3(\rho) := \frac{1}{\sqrt{T_0}} \|e_{\text{pre}}^{\mathcal{R}}\|_{W_\rho}, \quad (32)$$

where $\|v\|_{Q_\rho^{-1}} := \sqrt{v'Q_\rho^{-1}v}$, $\|v\|_{W_\rho} := \sqrt{v'W_\rho v}$, and

$$Q_\rho := \frac{1}{T_0} X'_{\text{pre}} W_\rho X_{\text{pre}} + \zeta^2 I_{N_0} \quad (33)$$

is the Hessian of F_ρ (up to the constant $2T_0$).

Proposition 4 (Weight-estimation error envelope). For every $\rho \in [0, 1]$,

$$\|\text{Term A}(\rho)\|_2 \leq \mathcal{P}_\rho [A_1(\rho) + A_2(\rho) + A_3(\rho)], \quad (34)$$

where $\mathcal{P}_\rho := \|(X_{\text{post}} - \Pi_\rho X_{\text{pre}})Q_\rho^{-1/2}\|_{\text{op}}$ is the transfer multiplier.

Proposition 4 bounds the weight-estimation error with four ingredients, each with a distinct role. The terms $A_1(\rho)$, $A_2(\rho)$, and $A_3(\rho)$ are three sources of the weight gap $\omega^{\text{oracle}} - \hat{\omega}(\rho, q)$, each tied to a specific distortion mechanism. The matrix Q_ρ , the ridge-regularized Gram matrix of the filtered donor series $W_\rho^{1/2} X_{\text{pre}}$, summarizes how sharply the filtered donor pool distinguishes different weight-reallocation patterns; the dual norm $\|\cdot\|_{Q_\rho^{-1}}$ through which A_1 and A_2 are measured reflects this geometry. The multiplier \mathcal{P}_ρ converts the weight gap into a prediction error and is the only place in the Term A envelope where the forecast operator \tilde{G}_q enters. We unpack each ingredient in turn, then synthesize them into two opposing forces that shape Term A in ρ .

The *metric distortion* $A_1(\rho)$ measures the contribution to the weight gap $\omega^{\text{oracle}} - \hat{\omega}$ that arises because HSC and the oracle use different *metrics* to evaluate the pre-treatment residual: HSC uses W_ρ , whereas the oracle uses P_\perp . Thus A_1 is the structural price HSC pays for evaluating the pre-treatment residual under W_ρ rather than the oracle's P_\perp , which leaves the weight criterion no longer aligned with the oracle's identification target. Two limiting cases eliminate this price entirely. First, at $\rho = 1$, $W_\rho = P_\perp$ and A_1 vanishes because the two metrics coincide. Second, A_1

vanishes for all ρ whenever $P_{\perp} e_{\text{pre}}^L = 0$, that is, whenever the treated unit's signal $L_{1,\text{pre}}$ can be written as a convex combination of donor signals $L_{0,\text{pre}}\omega^{\text{oracle}}$ plus a $\text{Null}(K)$ component.¹¹ Beyond these two cases, the metric discrepancy $W_{\rho} - P_{\perp}$ widens as ρ decreases from 1, which pushes A_1 upward. However, because A_1 is measured in the Q_{ρ}^{-1} norm, which also depends on ρ , the net behavior of $A_1(\rho)$ need not be monotonic. Notably, A_1 can be nonzero even when $\mathcal{R} = 0$, which is the sense in which it is a purely structural channel.

The *interaction* $A_2(\rho)$ captures how idiosyncratic components in the donor units $\mathcal{R}_{0,\text{pre}}$ can perturb weight estimation *when the signal L is not perfectly matched*. The oracle benchmark is defined using the shared component L only, and the HSC objective is evaluated on the observed donor outcomes $X_{\text{pre}} = L_{0,\text{pre}} + \mathcal{R}_{0,\text{pre}}$. As a result, $\mathcal{R}_{0,\text{pre}}$ can accidentally align with $W_{\rho} e_{\text{pre}}^L$ and appear to help reduce the remaining signal mismatch in sample, thereby shifting $\hat{\omega}(\rho)$ away from ω^{oracle} . This term is large when $\mathcal{R}_{0,\text{pre}}$ has a substantial projection onto $W_{\rho} e_{\text{pre}}^L$, and it vanishes whenever $P_{\perp} e_{\text{pre}}^L = 0$.

The *spurious matching* $A_3(\rho)$ measures how tempted the HSC weight criterion is to chase idiosyncratic components in the donors. Unlike A_1 and A_2 , this channel does not require any mismatch in L . The oracle weights ω^{oracle} are chosen to fit L alone. The \mathcal{R} -mismatch $e_{\text{pre}}^{\mathcal{R}} = \mathcal{R}_{1,\text{pre}} - \mathcal{R}_{0,\text{pre}}\omega^{\text{oracle}}$ is untouched by the oracle and can be large. The HSC weight criterion thus has an incentive to deviate from ω^{oracle} to absorb it, pulling weights toward donors whose idiosyncratic components happen to co-move with $\mathcal{R}_{1,\text{pre}}$.

The sensitivity of A_3 to ρ depends critically on whether \mathcal{R} is short-run noise or a stochastic trend. At $\rho = 1$, $W_{\rho} = P_{\perp}$, and the weight criterion applies no spectral down-weighting beyond removing the null-space component. If \mathcal{R} contains a random-walk component, $\|e_{\text{pre}}^{\mathcal{R}}\|_{P_{\perp}}$ grows at rate $O_p(T_0)$, so $A_3(1) = O_p(T_0^{1/2}) \rightarrow \infty$, which reflects the spurious regression phenomenon discussed in Section 2.3. At $\rho = 0$, the metric reduces to $W_0 = K = D'_q D_q$, so the weight criterion operates on the q th differences of $e_{\text{pre}}^{\mathcal{R}}$; differencing renders the random-walk component stationary and yields $A_3(0) = O_p(1)$, thereby controlling the spurious channel. For interior values $\rho \in (0, 1)$,

¹¹Concretely, $P_{\perp} e_{\text{pre}}^L = 0$ means that the oracle achieves zero residual-fit term in (23): the mismatch in L lies entirely in $\text{Null}(K)$ (a level shift for $q = 1$, an affine trend for $q = 2$). Both W_{ρ} and P_{\perp} assign zero weight to $\text{Null}(K)$, so the choice of metric is inconsequential.

the spectral weight $w(\mu; \rho) = \mu / ((1 - \rho) + \rho\mu)$ interpolates smoothly between the two extremes: larger ρ retains more low-frequency energy in the weight criterion and is therefore more vulnerable to spurious matching when \mathcal{R} contains a stochastic trend, whereas smaller ρ down-weights low-frequency components more aggressively, at the cost of the metric distortion already discussed for $A_1(\rho)$. When $e_{\text{pre}}^{\mathcal{R}}$ contains only short-run noise, either because \mathcal{R} itself is stationary or because the treated unit and the control donors form a cointegrated system under the oracle weights so that the stochastic-trend components cancel, A_3 is $O_p(1)$ at both endpoints.

The operative quantity is $\lambda_{\max}(Q_\rho^{-1})$, the largest eigenvalue of Q_ρ^{-1} . It measures how weakly the HSC criterion identifies the donor weights: a large value means the filtered donors are nearly collinear in some direction, so small score discrepancies are amplified through the dual norm $\|\cdot\|_{Q_\rho^{-1}}$, inflating A_1 and A_2 . How $\lambda_{\max}(Q_\rho^{-1})$ changes with ρ can be *non-monotonic*. At $\rho = 0$, the metric is K_q , so low-frequency directions are already most strongly down-weighted while high-frequency directions are amplified. Moving ρ away from zero gradually restores weight on low-frequency components and reduces the amplification of high-frequency components. Depending on the frequency composition of the control donors, these two effects can make $\lambda_{\max}(Q_\rho^{-1})$ peak at an interior $\rho \in (0, 1)$. The ridge floor ζ^2 in Q_ρ guarantees that $\lambda_{\max}(Q_\rho^{-1}) \leq 1/\zeta^2$ even when the filtered donors are nearly collinear; the no-ridge comparison in Appendix B shows that without this floor $\lambda_{\max}(Q_\rho^{-1})$ can grow dramatically.

The transfer multiplier $\mathcal{P}_\rho = \|(X_{\text{post}} - \Pi_\rho X_{\text{pre}})Q_\rho^{-1/2}\|_{\text{op}}$ depends on ρ through two distinct mechanisms. The first is the inverse curvature $Q_\rho^{-1/2}$, which reflects the same identification geometry that shapes A_1 and A_2 . The second is C_ρ ; its dependence on ρ runs through the smoother S_ρ , which determines how much of each donor's pre-treatment path is passed to the forecaster.

Taken together, the envelope $\mathcal{P}_\rho[A_1 + A_2 + A_3]$ is governed by two opposing forces in ρ . At large ρ the dominant cost is *spurious matching*: the A_3 channel grows when \mathcal{R} carries stochastic trends, formalizing the spurious donor matching risk of Section 2.3. At small ρ the dominant cost is *identification loss*: the metric gap $W_\rho - P_\perp$ widens, possibly inflating A_1 , and the filtered donor design $W_\rho^{1/2} X_{\text{pre}}$ sheds low-frequency variation, inflating $\lambda_{\max}(Q_\rho^{-1})$. This is the over-filtering cost of Section 2.4, and it is most severe when the donor series are dominated by low-frequency variation,

as is typical for macroeconomic data. The net shape of the envelope in ρ is therefore non-monotonic in general, and depends on the size and structure of the signal mismatch e_{pre}^L , the persistence of \mathcal{R} , the frequency composition of the donor design X_{pre} , and the forecast operator \tilde{G}_q .

5.4. Forecasting error

Term B is the prediction error that would remain even if the HSC weights coincided with the oracle weights. Its size depends on how accurately the composed operator $\Pi_\rho = \tilde{G}_q S_\rho$ extrapolates the oracle pre-treatment residual into the post-treatment window. Because S_ρ varies with ρ while \tilde{G}_q does not, the ρ -dependence of Term B is governed entirely by the smoother and by what it forwards to the forecaster.

Recall the oracle pre-treatment residual $r_{\text{pre}}^{\text{oracle}}$ from Section 5.2, and define its post-treatment counterpart:

$$r_{\text{pre}}^{\text{oracle}} := Y_{\text{pre}} - X_{\text{pre}} \omega^{\text{oracle}} \in \mathbb{R}^{T_0}, \quad r_{\text{post}}^{\text{oracle}} := Y_{\text{post}}(0) - X_{\text{post}} \omega^{\text{oracle}} \in \mathbb{R}^{T_{\text{post}}}. \quad (35)$$

The null-space component is the exception under Π_ρ . By the null-space continuation property (21), $\Pi_\rho v = G_q^{\text{null}} v$ for every $v \in \text{Null}(K)$ regardless of ρ : the smoother leaves such a component intact and the forecaster then continues it by G_q^{null} , in both steps independently of ρ . The null-space content of the oracle residual therefore contributes a fixed offset to the post-treatment prediction at every ρ and plays no role in the ρ -dependent tradeoff. Accordingly, define

$$\eta_{\text{pre}}^{\text{oracle}} := r_{\text{pre}}^{\text{oracle}} - P_0 r_{\text{pre}}^{\text{oracle}} = P_\perp r_{\text{pre}}^{\text{oracle}}, \quad \eta_{\text{post}}^{\text{oracle}} := r_{\text{post}}^{\text{oracle}} - G_q^{\text{null}} P_0 r_{\text{pre}}^{\text{oracle}}. \quad (36)$$

Both vectors are the oracle residual with the same null-space content $P_0 r_{\text{pre}}^{\text{oracle}}$ removed: directly in the pre-period, and through its canonical continuation $G_q^{\text{null}} P_0 r_{\text{pre}}^{\text{oracle}}$ in the post-period. With this common adjustment, Term B(ρ) takes the form

$$\eta_{\text{post}}^{\text{oracle}} - \tilde{G}_q S_\rho \eta_{\text{pre}}^{\text{oracle}}, \quad (37)$$

with the derivation given in Appendix A.2. Both $\eta_{\text{post}}^{\text{oracle}}$ and $\eta_{\text{pre}}^{\text{oracle}}$ are ρ -independent; all ρ -dependence in Term B(ρ) enters through the smoother S_ρ .

At the endpoint $\rho = 0$, $S_0 = I$ and Term B(0) = $\eta_{\text{post}}^{\text{oracle}} - \tilde{G}_q \eta_{\text{pre}}^{\text{oracle}}$. At the other endpoint $\rho = 1$,

$S_1 = P_0$, and since $\eta_{\text{pre}}^{\text{oracle}} \in \text{Null}(K)^\perp$ by construction, $S_1 \eta_{\text{pre}}^{\text{oracle}} = 0$ and therefore Term B(1) = $\eta_{\text{post}}^{\text{oracle}}$. At $\rho = 1$ the forecaster makes no contribution to Term B beyond the canonical null-space continuation already absorbed into $\eta_{\text{post}}^{\text{oracle}}$, so the choice of \tilde{G}_q is irrelevant at this endpoint. Between the endpoints, as ρ increases from 0 to 1, the smoothed input $S_\rho \eta_{\text{pre}}^{\text{oracle}}$ decreases monotonically toward zero in the spectral sense of Section 4, so ρ is the dial that controls how much of $\eta_{\text{pre}}^{\text{oracle}}$ reaches the forecaster.

How ρ affects $\|\text{Term B}\|$ then depends on how well the raw forecast $\tilde{G}_q \eta_{\text{pre}}^{\text{oracle}}$ tracks $\eta_{\text{post}}^{\text{oracle}}$. When $\tilde{G}_q \eta_{\text{pre}}^{\text{oracle}}$ already predicts $\eta_{\text{post}}^{\text{oracle}}$ well, the raw forecast is useful and $\rho = 0$ is preferred. When $\tilde{G}_q \eta_{\text{pre}}^{\text{oracle}}$ over-extrapolates the noisier part of the residual, smoothing its input first improves the forecast and an interior $\rho > 0$ is preferred. When $\tilde{G}_q \eta_{\text{pre}}^{\text{oracle}}$ is far from $\eta_{\text{post}}^{\text{oracle}}$, the forecaster is harmful, and $\rho = 1$, which discards its input entirely and leaves Term B equal to $\eta_{\text{post}}^{\text{oracle}}$, is preferred. This logic suggests that a longer post-treatment window favors a larger ρ : the time series forecaster becomes less reliable at distant horizons, which pushes the preferred regime toward stronger regularization or full suppression of the time series forecaster.

5.5. Implications for tuning

Sections 5.3 and 5.4 characterized the two errors that HSC trades off as ρ varies. We now collect their implications for the choices a practitioner makes. HSC exposes four such choices, and the decomposition shows they play distinct roles. The tuning parameter ρ allocates the pre-treatment residual between donor matching and the time series forecaster. The forecast operator \tilde{G}_q and the smoothness order q are structural: \tilde{G}_q fixes how the non-null residual is extrapolated, and q fixes what counts as smooth and how the null space is continued. The cross-validation horizon h does not change the estimator; it determines which of the two errors the cross-validation criterion weighs most heavily. We take ρ first, then \tilde{G}_q , q , and h .

ρ is the allocation lever, and the tradeoff it controls is two-sided. At large ρ the weight criterion retains the low-frequency content of the pre-treatment residual, so when \mathcal{R} carries a stochastic trend the spurious matching channel A_3 grows and Term A rises. At small ρ the criterion is restricted toward high-frequency content: the metric distortion A_1 widens and the filtered donor

design sheds the low-frequency variation that identifies the weights, so Term A rises again through identification loss. The ρ -shape of Term B is governed instead by how accurately the composed operator extrapolates the oracle residual: when the raw forecast tracks $\eta_{\text{post}}^{\text{oracle}}$ well a small ρ is preferred, and when it does not a large ρ , which suppresses the forecaster's input, is preferred. Neither error is monotone in ρ , and their sum has no general optimum; the best ρ depends on the data-generating regime.

The forecast operator \tilde{G}_q is the lever common to both errors. It enters Term A only through C_ρ inside the transfer multiplier \mathcal{P}_ρ , and it drives Term B directly through $\tilde{G}_q S_\rho \eta_{\text{pre}}^{\text{oracle}}$. A forecaster that extrapolates the oracle residual well lowers the Term B floor. Its effect on the multiplier \mathcal{P}_ρ is separate: \mathcal{P}_ρ depends on the forecaster only through the donor forecast residuals $C_\rho = X_{\text{post}} - \Pi_\rho X_{\text{pre}}$, and the same operator can behave differently on $\eta_{\text{pre}}^{\text{oracle}}$ than on the donor paths, so the two effects need not move together. In the Monte Carlo study, the constant carry-forward and the ARIMA(1, 1, 0) forecasters both perform well.¹²

The smoothness order q is a structural choice: it fixes the penalty K_q , the null space $\text{Null}(K_q)$, and the canonical continuation G_q^{null} , and the decomposition makes its role precise. At $\rho = 0$ the metric is $K_q = D_q' D_q$, so $A_3(0) \propto \|D_q e_{\text{pre}}^{\mathcal{R}}\|_2$ is controlled only if q is large enough that D_q stationarizes the idiosyncratic component of \mathcal{R} . An $I(1)$ idiosyncratic stochastic trend is stationarized by $q = 1$, whereas an $I(2)$ idiosyncratic stochastic trend is not and requires $q = 2$. Raising q to 2 also enlarges the null space and allows a more flexible specification: since $\text{Null}(K_1) \subset \text{Null}(K_2)$, any approximately affine gap between the treated unit's signal and its donor combination is then absorbed at no metric-distortion cost. These benefits come with two costs. First, the same enlargement forces G_q^{null} to continue that affine direction: for $q = 2$ it extends the line fitted to $P_{0,2} r_{\text{pre}}^{\text{oracle}}$, and by the null-space continuation property (21) this continuation sits inside Term B at every ρ and can carry an extrapolation bias that grows with the post-treatment window T_{post} , whereas the

¹²In both cases the rule is the data-driven component \hat{G}_q of the construction in Definition 3: it is applied to the non-null part $P_{\perp,q} r$ of the pre-treatment residual r , while the null-space part $P_{0,q} r$ is continued by the canonical G_q^{null} . When \hat{G}_q is the constant carry-forward, the two parts recombine in closed form. For $q = 1$, the continued mean plus the carried-forward demeaned residual equals the last entry r_{T_0} held constant, so \hat{G}_1 coincides with the constant carry-forward applied directly to the raw pre-treatment residual. For $q = 2$, the composed forecast at horizon h is $r_{T_0} + \hat{\beta} h$, where $\hat{\beta}$ is the slope of the line fitted to the pre-treatment residual over $\text{Null}(K_2)$; equivalently, the fitted linear trend is extrapolated with its level re-anchored to the last entry r_{T_0} . Under the ARIMA(1, 1, 0) rule, the null-space part is continued in the same way, while the non-null part is forecast by the ARIMA model.

$q = 1$ continuation carries a level forward and leaves a floor that is flat in the horizon. Second, the spectrum of K_2 is much wider than that of K_1 , which makes the amplification to the high-frequency components much more significant. The metric gap $W_{\rho,q} - P_{\perp,q}$, and hence A_1 , rises more steeply as ρ falls from 1.

The cross-validation horizon h does not alter the estimator but selects which error the criterion minimizes. At a short horizon the forecaster’s extrapolation bias is typically small, so the criterion is dominated by Term A. At a long horizon the extrapolation bias accumulates and Term B can dominate; the criterion then rewards a large $\hat{\rho}$ mechanically, which suppresses the time series forecaster. It is worth noting that a larger h leaves less pre-treatment data for cross-validation. In practice, when the pre-treatment window is short, the researcher must balance the post-treatment horizon of interest against the amount of pre-treatment data retained for cross-validation.

These choices are not independent. The cross-validation criterion of Section 4.2 selects ρ , and optionally q and \tilde{G}_q jointly. In practice the structural choices can be guided by what is known about the application. Set q to the smallest order that plausibly stationarizes the raw data. Choose \tilde{G}_q conservatively unless the pre-treatment data give clear evidence that a richer forecaster predicts better. Then let cross-validation at the policy-relevant horizon h select ρ .

6. Monte Carlo Evidence

Sections 2–5 motivate HSC as a soft allocation mechanism, develop its spectral interpretation, and derive a prediction-error decomposition that separates donor matching from residual extrapolation. This section reports a Monte Carlo study that evaluates HSC’s finite-sample performance against standard synthetic control estimators and documents how the cross-validated tuning parameter $\hat{\rho}$ adapts to the underlying data-generating regime. Full details of the data-generating process appear in Appendix C.1.

6.1. Design

The data-generating process retains the additive structure used throughout the paper. Untreated potential outcomes follow

$$Y_{j,t}(0) = L_{j,t} + \kappa \mathcal{E}_{j,t} + \varepsilon_{j,t} + \alpha_j + \delta_t, \quad (38)$$

where $L_{j,t} = \sum_{k=1}^3 \Lambda_{j,k} F_{k,t}$ is a low-rank component built from three factors $F_{k,t}$ (one random walk, one ARIMA(1, 1, 0), one stationary AR(1)), $\kappa \mathcal{E}_{j,t}$ is a unit-specific ARIMA(1, 1, 0) component whose innovations interpolate between a common shock and an idiosyncratic shock by $\sqrt{\rho_u} u_t^c + \sqrt{1 - \rho_u} u_{j,t}^i$, $\varepsilon_{j,t} \sim \mathcal{N}(0, 1)$ is stationary noise, α_j is a unit fixed effect, and δ_t is a time fixed effect. The factor paths $F_{k,t}$, the idiosyncratic component $\mathcal{E}_{j,t}$, the noise $\varepsilon_{j,t}$, and the time fixed effects δ_t are redrawn in every replication; the factor loadings $\Lambda_{j,k}$ and the unit fixed effects α_j are drawn once and held fixed across replications. The treated unit's loadings are constructed as a sparse Dirichlet convex combination of donor loadings, placing the treated unit inside the donor convex hull. Two scalar parameters govern the persistence structure: $\kappa \in \{0, 0.5, 1, 2\}$ controls the amplitude of the unit-specific stochastic trend, and $\rho_u \in \{0, 0.5, 1\}$ controls how much of that persistence is shared across units. We replicate every (κ, ρ_u) cell $R = 500$ times with $T_0 = 200$ pre-treatment periods, $T_{\text{post}} = 20$ post-treatment periods, and $N_0 = 50$ donors. The treated unit receives no treatment effect, so the post-period RMSE between the estimated counterfactual and the untreated potential outcome measures predictive accuracy.

We compare five baseline synthetic control estimators against HSC. The baselines are plain SC (Abadie, Diamond and Hainmueller, 2010), SC with an intercept (SC-INT, Doudchenko and Imbens 2016), synthetic difference-in-differences (SDID, Arkhangelsky et al., 2021), and two variants of the synthetic business-cycle estimator of Shi, Xi and Xie (2025) that differ in the pre-treatment filter used to extract the cyclical component (SBCA-ARIMA and SBCA-Hamilton). Plain SC matches in levels and is therefore vulnerable to spurious matching. SC-INT removes a unit-specific level shift with an intercept, and SDID constructs its unit weights from a level-matching problem with an intercept and a ridge penalty; both still match the residual variation in levels. The SBCA family applies a pre-treatment filter to separate trend from cycle, matches donors on the cycle, and

extrapolates the treated trend independently.

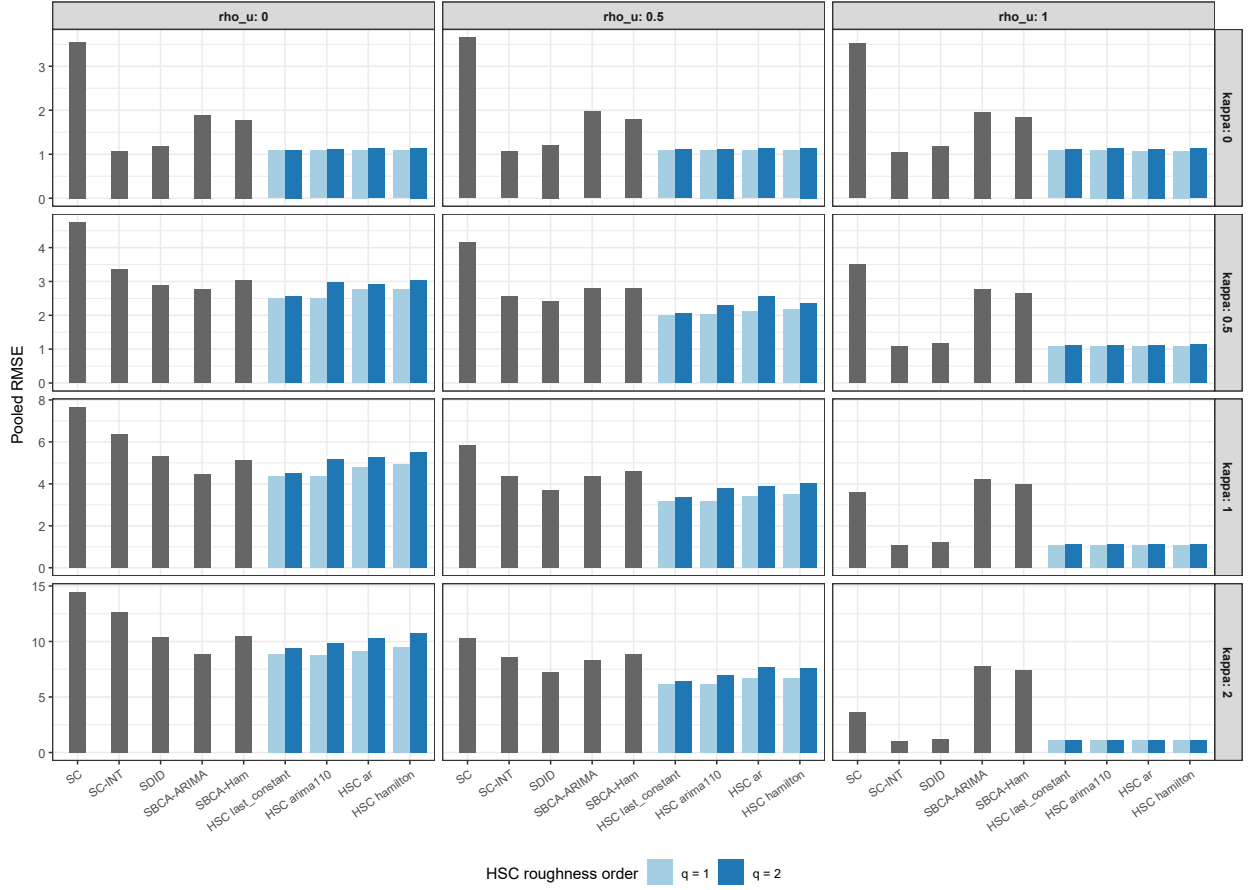
For HSC we evaluate four time series forecasters that all satisfy Definition 3: in each case the forecaster is applied only to the non-null-space component, while the null-space component is continued by the canonical G_q^{null} . The `last_constant` forecaster carries the last fitted value of the non-null-space component forward as a constant; under $q = 1$ this, combined with the canonical constant continuation of the null space, recovers carrying the last fitted value of the residual forward, and under $q = 2$ it adds a constant offset to the null-space linear extension. The `arma110` forecaster fits an ARIMA(1,1,0) to the non-null-space component, the correctly specified model for the DGP’s idiosyncratic ARIMA(1,1,0) stochastic trend. The `ar` forecaster fits a stationary AR(4) to the non-null-space component, whose forecasts mean-revert. The `hamilton` forecaster forecasts the non-null-space component with the h -step-ahead regression of Hamilton (2018). Each forecaster is evaluated at both smoothness orders $q \in \{1, 2\}$. The cross-validation horizon is fixed at $h = 1$ in this section; Appendix C.4 examines the effect of choosing $h = 20$ instead.

6.2. HSC ties or improves on baselines across regimes

Figure 6 reports the post-period RMSE pooled across the 20 post-treatment periods for each of the 12 (κ, ρ_u) cells. Within each panel we show the five baseline estimators as single bars, and we show each HSC forecaster as two bars side by side: the lighter bar reports the $q = 1$ result and the darker bar reports $q = 2$.

Three patterns are visible. First, when the component $\mathcal{E}_{j,t}$ is absent or shared across units, all four HSC forecasters tie SC-INT and SDID and substantially improve on plain SC and the SBCA family. The top row of the figure ($\kappa = 0$) and the right column ($\rho_u = 1$) display this behavior: HSC’s pooled RMSE is within a few percent of SC-INT and SDID, plain SC sits well above the others because it cannot remove the heterogeneous unit intercepts, and the SBCA filters strip away common variation that the other methods can match. Second, when the $\mathcal{E}_{j,t}$ component is present and partially or fully idiosyncratic ($\kappa \geq 0.5, \rho_u \leq 0.5$), HSC with $q = 1$ delivers the lowest pooled RMSE in most cells. The margin between HSC and SC-INT or SDID grows with κ and is

Figure 6. POST-PERIOD POOLED RMSE BY METHOD ACROSS THE (κ, ρ_u) GRID



it *Notes:* Bars report pooled RMSE $\sqrt{R^{-1}T_{\text{post}}^{-1} \sum_{r,h} (\hat{Y}_{1,T_0+h}^{(r)} - Y_{1,T_0+h}^{(0,r)})^2}$ across $R = 500$ replications and $T_{\text{post}} = 20$ post-treatment periods, for each (κ, ρ_u) cell. The five baseline estimators appear as single grey bars; the four HSC forecasters appear as paired bars with the lighter shade denoting $q = 1$ and the darker shade denoting $q = 2$. $T_0 = 200$, $N_0 = 50$, $h = 1$ cross-validation; the treated unit's loadings lie inside the donor convex hull.

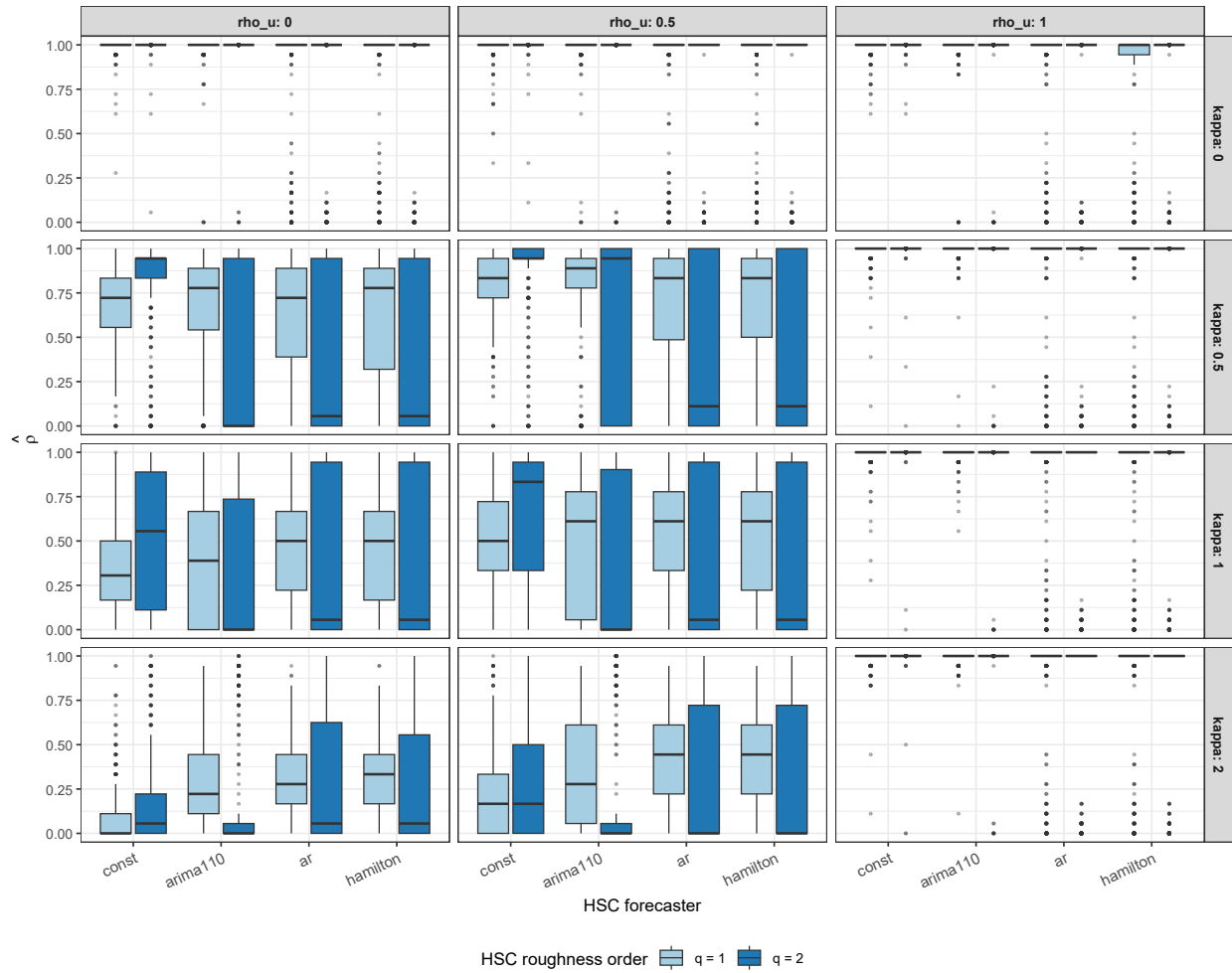
largest in the corner with the most idiosyncratic drift. The SBICA family performs well when $\mathcal{E}_{j,t}$ is completely idiosyncratic but becomes worse when $\mathcal{E}_{j,t}$ is partially shared. Third, the difference in performance between time series forecasters is visible here; the `last_constant` and `arima110` forecasters perform better than the `ar` and `hamilton` forecasters. The $q = 1$ HSC also performs better than the $q = 2$ configuration. These differences in configurations reflect the design of the DGP, as the idiosyncratic stochastic trend is an ARIMA(1,1,0) model and $q = 1$ suffices to control the spurious matching. Appendix C.2 shows that this pooled ranking holds horizon by horizon for the strongest configurations, the constant carry-forward and the $q = 1$ ARIMA(1, 1, 0) forecaster, and Appendix C.3 attributes the pooled advantage to a variance reduction that more than offsets

a small bias penalty.

6.3. Cross-validation adapts to the regime

The argument in Section 5 predicts that the optimal ρ depends on the data: when the stochastic trend is shared across units, level matching identifies donor weights well and ρ near one is optimal; when the stochastic trend is idiosyncratic, the donor pool cannot reproduce it and filtering it out by pushing ρ toward zero is preferred. Figure 7 reports the distribution of the cross-validated $\hat{\rho}$ across the same (κ, ρ_u) grid for the four HSC forecasters at both smoothness orders.

Figure 7. DISTRIBUTION OF CROSS-VALIDATED $\hat{\rho}$ ACROSS THE (κ, ρ_u) GRID



Notes: Boxplots report the distribution of the cross-validated $\hat{\rho}$ across $R = 500$ replications for each (κ, ρ_u) cell, for the four HSC time series forecasters at smoothness orders $q = 1$ (lighter shade) and $q = 2$ (darker shade). $T_0 = 200$, $N_0 = 50$, cross-validation horizon $h = 1$.

The cross-validated selection behaves as the theory predicts. When the idiosyncratic stochastic trend is absent ($\kappa = 0$, the top row of the figure or $\rho_u = 1$, the right column of the figure) the distribution of $\hat{\rho}$ almost piles up at one for every forecaster and both smoothness orders: with no idiosyncratic stochastic trend component to filter out, the CV objective rewards matching in levels. When the stochastic trend is present and at least partially unit-specific ($\kappa \geq 1$, $\rho_u \leq 0.5$, bottom-left region of the figure), $\hat{\rho}$ shifts downward: medians fall to around 0.5 at $\kappa = 1$ and near zero at $\kappa = 2$ with $\rho_u = 0$, with substantial dispersion across replications. The shift happens for all four forecasters and at both smoothness orders, confirming that the rolling-origin CV identifies the correct allocation between donor matching and time series forecaster directly from the data. Two further properties of the cross-validated allocation are deferred to the appendix: Appendix C.4 reports how $\hat{\rho}$ and post-period RMSE shift when the CV horizon h is extended from one to twenty.

7. Empirical Application: The 1997 Handover of Hong Kong

We illustrate HSC on the study of the per-capita GDP after the 1997 return of Hong Kong to Chinese sovereignty. The example was introduced by Hsiao, Ching and Wan (2012) and revisited by Shi, Xi and Xie (2025). Hsiao, Ching and Wan (2012) difference the data to a stationary growth-rate outcome and select a small set of geographically and economically proximate donors, including mainland China and Hong Kong’s Asian trading partners, by an information criterion, fitting an unrestricted regression of the treated series on the selected donors. Shi, Xi and Xie (2025) instead work with the nonstationary level of annual per-capita GDP, restrict the donor pool to developed economies with comparable long-run growth, and impose a hard separation between a treated-unit trend forecast from Hong Kong’s own history and a donor-matched cyclical component. Throughout we use the sign convention $\hat{\tau}_t = Y_{1t} - \hat{Y}_{1t}(0)$, so a negative value means observed Hong Kong GDP lies below the estimated no-handover counterfactual. The main text uses the annual data of Shi, Xi and Xie (2025) so that the comparison with the most closely related estimator is exact; Appendix D reports robustness to the cross-validation horizon and to the Hsiao, Ching and Wan (2012) geographic-neighbour donor pool.

7.1. Data and cross-validated configuration

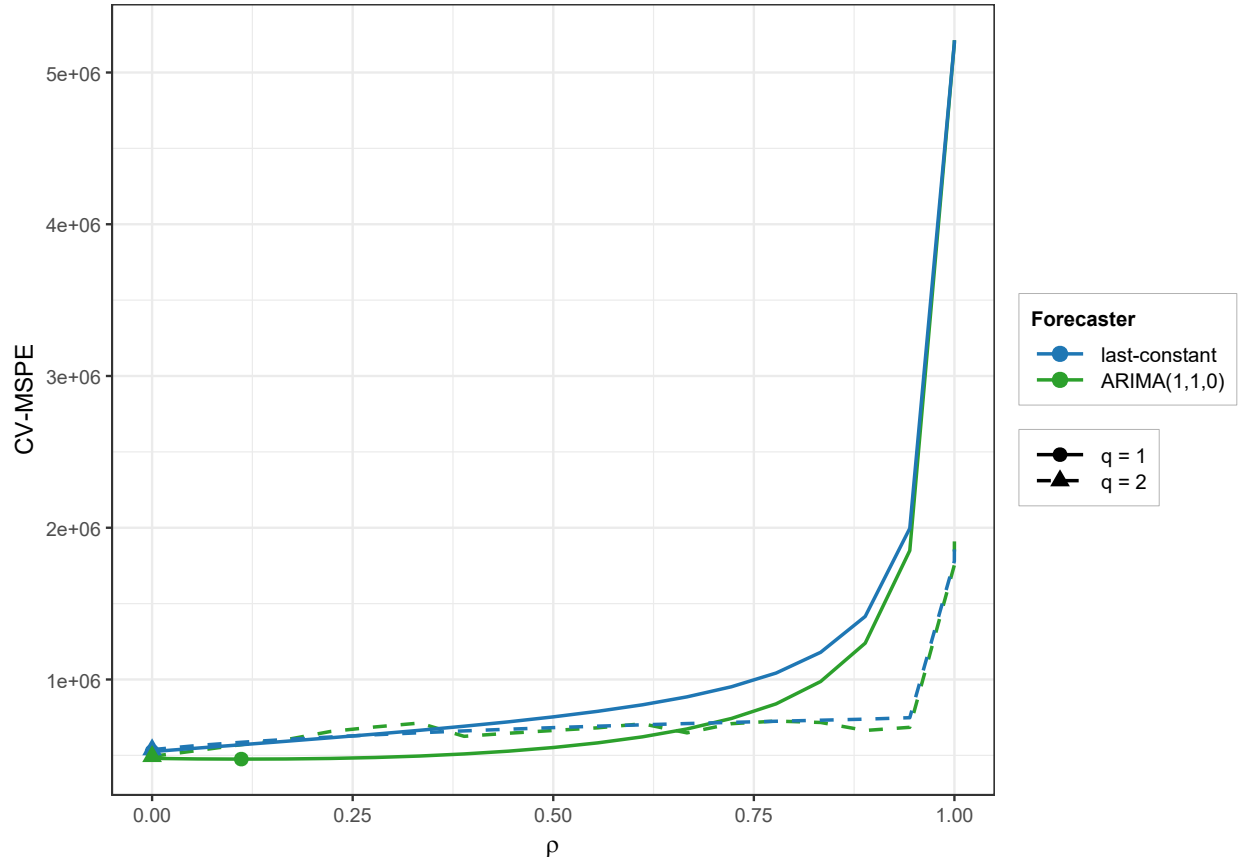
The panel is the one assembled by [Shi, Xi and Xie \(2025\)](#): annual real per-capita GDP for Hong Kong and eleven developed donor economies, including Australia, Austria, Canada, Denmark, France, Germany, Italy, Korea, the Netherlands, New Zealand, and the United States over 1961–2003. The treatment year is 1997, giving $T_0 = 36$ pre-treatment years (1961–1996) and $T_{\text{post}} = 7$ post-treatment years (1997–2003); the United Kingdom and mainland China are excluded as parties directly involved in the handover, and economies exposed to the 1997–98 Asian financial crisis or with heterogeneous welfare-state structures are excluded, following [Shi, Xi and Xie \(2025\)](#). The panel-data implementation of [Hsiao, Ching and Wan \(2012\)](#), which instead selects geographically proximate Asian donors by an information criterion on differenced data, is examined as a robustness check in Appendix D.

We evaluate HSC under four configurations: the `last_constant` and ARIMA(1, 1, 0) forecasters, each at roughness orders $q \in \{1, 2\}$, which are the configurations that performed well in the Monte Carlo study of Section 6. The tuning parameter $\hat{\rho}$ is selected by rolling-origin cross-validation with one-step-ahead horizon ($h = 1$), a 21-point ρ -grid, and the SDID-style ridge $\zeta = T_{\text{post}}^{1/4} \hat{\sigma}_{\Delta X}$. Figure 8 reports the cross-validated mean squared prediction error along the ρ -grid for the four configurations. The cross-validation selects an interior optimum: the best configuration is ARIMA(1, 1, 0) at $q = 1$ with $\hat{\rho} = 0.11$.

7.2. Counterfactual comparison

Figure 9 overlays the cross-validation-selected HSC counterfactual with those of plain synthetic control (SC, [Abadie, Diamond and Hainmueller, 2010](#)), synthetic control with an intercept (SC-INT, [Doudchenko and Imbens, 2016](#)), synthetic difference-in-differences (SDID, [Arkhangelsky et al., 2021](#)), and the synthetic business-cycle estimator of [Shi, Xi and Xie \(2025\)](#) (SBCA-Hamilton), together with observed Hong Kong GDP. The estimators fall into three groups. The HSC counterfactual tracks observed Hong Kong closely throughout the post-treatment window, reaching about \$30,000 by 2003 against an observed \$28,100, an implied $\hat{\tau}_{2003} \approx -\$1,900$. SC, SC-INT, and SDID drift moderately above the observed series. SBCA-Hamilton diverges sharply: because it forecasts

Figure 8. HONG KONG: CROSS-VALIDATED MSPE FOR THE FOUR HSC CONFIGURATIONS



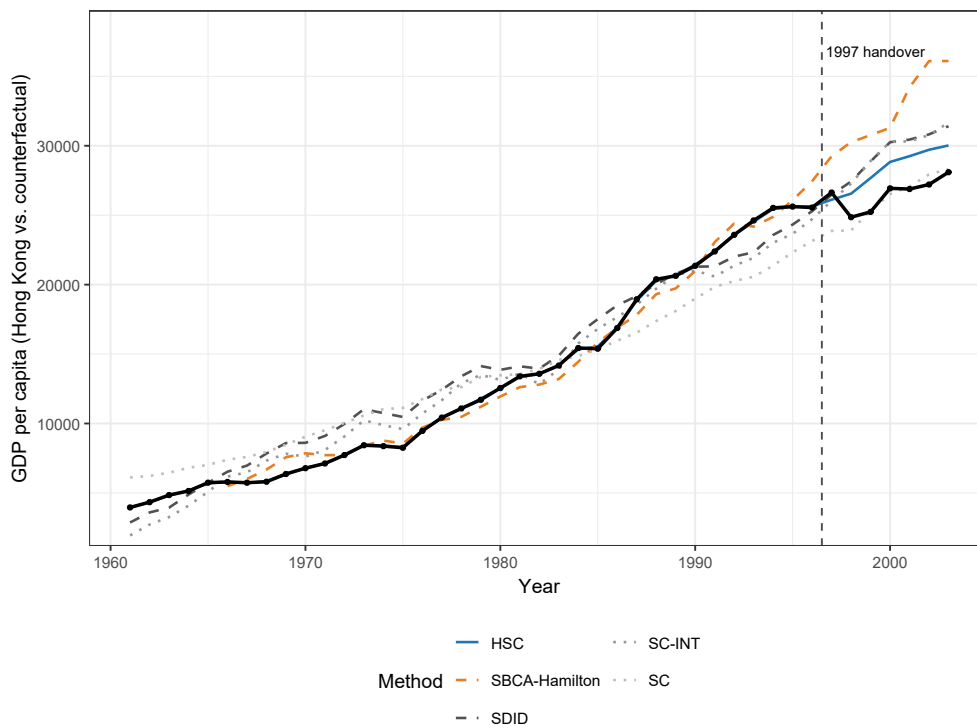
Note: Cross-validated mean squared prediction error (rolling-origin, one-step-ahead, `cv_last` = 15, 21 folds) as a function of the spectral allocation parameter ρ , for the four HSC configurations (`last.constant` and `ARIMA(1,1,0)`) forecasters at roughness orders $q = 1$ and $q = 2$. A marker on each curve denotes that configuration’s cross-validated $\hat{\rho}$. The selected configuration is `ARIMA(1,1,0)`, $q = 1$, $\hat{\rho} = 0.11$. Sample: Hong Kong plus eleven developed donor economies, annual per-capita GDP, 1961–1996 pre-treatment fitting window.

Hong Kong’s post-1997 trend by a recursive linear projection of its own pre-1997 history, and Hong Kong’s pre-handover growth was unusually steep, that projection rises to roughly \$36,100 by 2003, an implausibly large effect.

7.3. Donor-weight diversification

Figure 10 compares the donor weights that HSC, SDID, SC-INT, and SBICA-Hamilton assign across the eleven donors. The contrast is stark. HSC distributes weight broadly across all eleven economies, with no single weight exceeding 0.19 (the largest are Korea 0.18, Germany 0.14, the United States 0.13, and Italy 0.11). SC-INT collapses onto a corner solution, placing 0.91 on

Figure 9. HONG KONG: COUNTERFACTUAL PER-CAPITA GDP BY ESTIMATOR



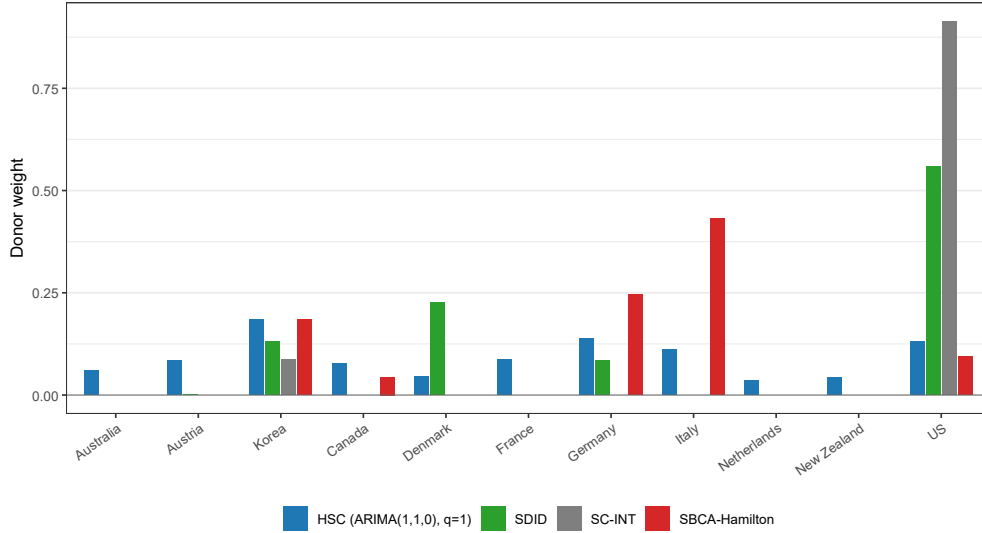
Note: Observed Hong Kong per-capita GDP (solid black, with markers) and estimated no-handover counterfactuals from HSC (the cross-validation-selected ARIMA(1, 1, 0), $q = 1$, $\hat{\rho} = 0.11$), SBCA-Hamilton (Shi, Xi and Xie, 2025), SDID (Arkhangelsky et al., 2021), SC-INT (Doudchenko and Imbens, 2016), and plain SC (Abadie, Diamond and Hainmueller, 2010). The vertical dashed line marks the 1997 handover. SBCA-Hamilton’s post-1997 trend is a recursive linear projection of Hong Kong’s pre-1997 series and rises well above the observed path. Sample: eleven developed donor economies, annual per-capita GDP, 1961–2003 ($T_0 = 36$, $T_{\text{post}} = 7$).

the United States and 0.09 on Korea. SBCA-Hamilton concentrates on four donors (Italy 0.43, Germany 0.25, Korea 0.18, the United States 0.09). SDID is intermediate: its ridge penalty deconcentrates the weights relative to SC-INT. The United States weight falls from 0.91 to 0.56 and mass spreads to Denmark (0.23), Korea, and Germany.

7.4. Out-of-sample accuracy

Pre-treatment fit cannot discriminate among these estimators, because each minimizes a different in-sample criterion. We therefore evaluate every method by the same rolling-origin, one-step-ahead cross-validated MSPE used to select $\hat{\rho}$. HSC is the most accurate method by a wide margin: at $h = 1$ the selected configuration attains a CV-MSPE of 4.8×10^5 , and all four HSC configurations ($4.8\text{--}5.4 \times 10^5$) fall below every competing estimator—SBCA-Hamilton (1.2×10^6), SDID (1.5×10^6),

Figure 10. HONG KONG: DONOR WEIGHTS BY ESTIMATOR



Note: Donor weights assigned to the eleven developed donor economies by the cross-validation-selected HSC configuration (ARIMA(1, 1, 0), $q = 1$, $\hat{\rho} = 0.11$), SDID, SC-INT, and SBCA-Hamilton. All four estimators constrain the donor weights to sum to one. HSC spreads weight across all eleven donors; SC-INT and SBCA-Hamilton concentrate on one and four donors respectively; SDID’s ridge penalty places it between these extremes. Sample: annual per-capita GDP, 1961–1996 pre-treatment fitting window.

SC-INT (3.6×10^6), and plain SC (9.0×10^6). HSC thus improves on the synthetic business-cycle estimator by roughly a factor of two and a half, and on the level-matching estimators by one to two orders of magnitude, on a criterion that uses only pre-treatment data. Appendix D shows that this ranking is preserved when the cross-validation horizon is lengthened to $h = 4$ and when the donor pool is replaced by the geographic-neighbour pool of Hsiao, Ching and Wan (2012).

8. Conclusion

Harmonic synthetic control (HSC) addresses counterfactual estimation when untreated outcomes may contain both shared and idiosyncratic stochastic trends, a regime that the researcher cannot reliably distinguish *ex ante*. Instead of committing in advance to matching in the raw level or to differencing before matching, HSC introduces a treated-unit-specific smooth component and a single tuning parameter that rolling-origin cross-validation uses to allocate predictive responsibility between donor matching and time series forecaster. The spectral interpretation, the prediction-error decomposition, the Monte Carlo evidence, and the Hong Kong application all point to the same conclusion: a soft, data-driven allocation is more robust and can adapt to different regimes.

The present paper develops and evaluates the HSC point estimator; formal uncertainty quantification is the natural next step. A prediction interval for the HSC counterfactual should combine donor-weight estimation uncertainty with out-of-sample forecast-error calibration for the smooth component, extending the synthetic-control prediction-interval framework of [Cattaneo, Feng and Titiunik \(2021\)](#) to the soft-allocation setting. Because that construction rests on additional assumptions beyond those required for the point estimator, we leave it to future works.

References

- Abadie, A. and J. Gardeazabal. 2003. “The Economic Costs of Conflict: A Case Study of the Basque Country.” *The American Economic Review* 93(1):113–132.
- Abadie, Alberto. 2021. “Using synthetic controls: Feasibility, data requirements, and methodological aspects.” *Journal of economic literature* 59(2):391–425.
- Abadie, Alberto, Alexis Diamond and Jens Hainmueller. 2010. “Synthetic control methods for comparative case studies: Estimating the effect of California’s tobacco control program.” *Journal of the American statistical Association* 105(490):493–505.
- Abadie, Alberto, Alexis Diamond and Jens Hainmueller. 2015. “Comparative politics and the synthetic control method.” *American Journal of Political Science* 59(2):495–510.
- Arkhangelsky, Dmitry, Susan Athey, David A Hirshberg, Guido W Imbens and Stefan Wager. 2021. “Synthetic difference-in-differences.” *American Economic Review* 111(12):4088–4118.
- Ben-Michael, Eli, Avi Feller and Jesse Rothstein. 2021. “The augmented synthetic control method.” *Journal of the American Statistical Association* 116(536):1789–1803.
- Cattaneo, Matias D, Yingjie Feng and Rocio Titiunik. 2021. “Prediction intervals for synthetic control methods.” *Journal of the American Statistical Association* 116(536):1865–1880.
- Doudchenko, Nikolay and Guido W Imbens. 2016. Balancing, regression, difference-in-differences and synthetic control methods: A synthesis. Technical report National Bureau of Economic Research.
- Eilers, Paul H. C. and Brian D. Marx. 1996. “Flexible Smoothing with B-Splines and Penalties.” *Statistical Science* 11(2):89–121.
- Ferman, Bruno and Cristine Pinto. 2021. “Synthetic controls with imperfect pretreatment fit.” *Quantitative Economics* 12(4):1197–1221.
- Hamilton, James D. 2018. “Why you should never use the Hodrick–Prescott filter.” *Review of Economics and Statistics* 100(5):831–843.
- Harvey, Andrew and Stephen Thiele. 2021. “Cointegration and control: Assessing the impact of events using time series data.” *Journal of Applied Econometrics* 36(1):71–85.
- Henderson, Robert. 1924. “A New Method of Graduation.” *Transactions of the Actuarial Society of America* 25:29–40.

- Hodrick, Robert J and Edward C Prescott. 1997. “Postwar US business cycles: an empirical investigation.” *Journal of Money, credit, and Banking* pp. 1–16.
- Hsiao, Cheng, H Steve Ching and Shui Ki Wan. 2012. “A panel data approach for program evaluation: measuring the benefits of political and economic integration of Hong Kong with mainland China.” *Journal of Applied Econometrics* 27(5):705–740.
- Masini, Ricardo and Marcelo C Medeiros. 2021. “Counterfactual analysis with artificial controls: Inference, high dimensions, and nonstationarity.” *Journal of the American Statistical Association* 116(536):1773–1788.
- Masini, Ricardo and Marcelo C Medeiros. 2022. “Counterfactual analysis and inference with non-stationary data.” *Journal of Business & Economic Statistics* 40(1):227–239.
- Phillips, Peter CB. 1986. “Understanding spurious regressions in econometrics.” *Journal of econometrics* 33(3):311–340.
- Shi, Zhentao, Jin Xi and Haitian Xie. 2025. “A Synthetic Business Cycle Approach to Counterfactual Analysis with Nonstationary Macroeconomic Data.” *arXiv preprint arXiv:2505.22388*
- Sun, Liyang, Eli Ben-Michael and Avi Feller. 2024. Temporal aggregation for the synthetic control method. In *AEA Papers and Proceedings*. Vol. 114 American Economic Association 2014 Broadway, Suite 305, Nashville, TN 37203 pp. 614–617.
- Whittaker, E. T. 1922. “On a New Method of Graduation.” *Proceedings of the Edinburgh Mathematical Society* 41:63–75.

Online Supplementary Materials

A. Proofs

This appendix collects the proofs of all propositions, lemmas, and corollaries stated in the main text. Section A.1 covers the results of Section 3 (the HSC estimator and its endpoint properties), and Section A.2 covers the results of Section 5 (the prediction-error decomposition and the Term A and Term B envelopes).

A.1. Proofs for Section 3

A.1.1. Proof of Proposition 1

Proof Fix $q \in \{1, 2\}$, $\rho \in (0, 1)$, and $\omega \in \Delta_{N_0}$, and write $r := r_{\text{pre}}(\omega) = Y_{\text{pre}} - X_{\text{pre}}\omega$. The inner problem is

$$\min_{E \in \mathbb{R}^{T_0}} f(E), \quad f(E) := \frac{1}{\rho} \|r - E\|_2^2 + \frac{1}{1-\rho} E' K_q E. \quad (\text{A1})$$

The Hessian of f is $\frac{2}{\rho} I_{T_0} + \frac{2}{1-\rho} K_q \succ 0$ (since $\rho \in (0, 1)$), so f is strictly convex and the minimizer is unique.

Step 1: First-order condition. Setting $\nabla_E f = 0$ gives

$$\frac{1}{\rho}(\hat{E} - r) + \frac{1}{1-\rho} K_q \hat{E} = 0.$$

Multiplying by ρ and writing $\lambda_\rho := \rho/(1-\rho)$, this becomes $(I_{T_0} + \lambda_\rho K_q) \hat{E} = r$, whence

$$\hat{E} = S_{\rho,q} r, \quad S_{\rho,q} := (I_{T_0} + \lambda_\rho K_q)^{-1}. \quad (\text{A2})$$

Step 2: Profiled objective value. The FOC can be rewritten as

$$\frac{1}{\rho}(r - \hat{E}) = \frac{1}{1-\rho} K_q \hat{E}. \quad (\text{A3})$$

Using (A3) to substitute for the first term evaluated at \hat{E} ,

$$\begin{aligned}
f(\hat{E}) &= (r - \hat{E})' \cdot \frac{1}{\rho} (r - \hat{E}) + \hat{E}' \cdot \frac{1}{1 - \rho} K_q \hat{E} \\
&= (r - \hat{E})' \cdot \frac{1}{1 - \rho} K_q \hat{E} + \hat{E}' \cdot \frac{1}{1 - \rho} K_q \hat{E} \\
&= r' \cdot \frac{1}{1 - \rho} K_q \hat{E} \\
&= \frac{1}{1 - \rho} r' K_q S_{\rho, q} r.
\end{aligned} \tag{A4}$$

Now observe that

$$\frac{1}{\rho} (I_{T_0} - S_{\rho, q}) = \frac{1}{\rho} \lambda_\rho K_q S_{\rho, q} = \frac{1}{1 - \rho} K_q S_{\rho, q},$$

where the first equality uses $(I_{T_0} + \lambda_\rho K_q) S_{\rho, q} = I_{T_0}$, which rearranges to $I_{T_0} - S_{\rho, q} = \lambda_\rho K_q S_{\rho, q}$.^{A1}

Therefore, defining $W_{\rho, q} := \frac{1}{\rho} (I_{T_0} - S_{\rho, q})$,

$$f(\hat{E}) = r' W_{\rho, q} r. \tag{A5}$$

Step 3: Profiled weight problem. In the full HSC criterion (2), only $f(E)$ involves E . Replacing $f(E)$ by its minimum (A5) yields

$$\hat{\omega}(\rho, q) \in \arg \min_{\omega \in \Delta_{N_0}} \{ r_{\text{pre}}(\omega)' W_{\rho, q} r_{\text{pre}}(\omega) + \zeta^2 T_0 \|\omega\|_2^2 \},$$

which is (6). Substituting $\hat{\omega}(\rho, q)$ into (A2) gives (8). \square

A.1.2. Proof of Proposition 2

Proof Fix $q \in \{1, 2\}$ and write $K = K_q$, $P_0 = P_{0, q}$. Let $0 = \mu_1 = \dots = \mu_d < \mu_{d+1} \leq \dots \leq \mu_{T_0}$ be the eigenvalues of K (with $d = \dim \text{Null}(K) = q$), and let v_1, \dots, v_{T_0} be a corresponding orthonormal eigenbasis. For $\rho \in (0, 1)$, the definitions $\lambda_\rho = \rho/(1 - \rho)$ and $S_{\rho, q} = (I + \lambda_\rho K)^{-1}$ give

$$S_{\rho, q} v_k = \frac{1}{1 + \lambda_\rho \mu_k} v_k, \quad W_{\rho, q} v_k = \frac{1}{\rho} \left(1 - \frac{1}{1 + \lambda_\rho \mu_k} \right) v_k = \frac{\mu_k}{(1 - \rho) + \rho \mu_k} v_k.$$

Part (i): limits. For each eigenvalue μ_k , define $s_k(\rho) := 1/(1 + \lambda_\rho \mu_k)$ and $w_k(\rho) := \mu_k / ((1 - \rho) + \rho \mu_k)$.

^{A1}Because $S_{\rho, q} = (I_{T_0} + \lambda_\rho K_q)^{-1}$ is a function of K_q , the two operators commute and $K_q S_{\rho, q} = S_{\rho, q} K_q$, so either ordering may be used throughout.

As $\rho \downarrow 0$: $\lambda_\rho \rightarrow 0$, so $s_k(\rho) \rightarrow 1$ for every k . Hence $S_{\rho,q} \rightarrow I_{T_0}$. Similarly, $w_k(\rho) \rightarrow \mu_k$ for every k , so $W_{\rho,q} \rightarrow K = K_q$.

As $\rho \uparrow 1$: $\lambda_\rho \rightarrow \infty$. For the null-space eigenvectors ($\mu_k = 0, k \leq d$): $s_k(\rho) = 1$ and $w_k(\rho) = 0$ for all ρ . For the positive eigenvectors ($\mu_k > 0, k > d$): $s_k(\rho) = 1/(1 + \lambda_\rho \mu_k) \rightarrow 0$ and $w_k(\rho) = \mu_k / ((1 - \rho) + \rho \mu_k) \rightarrow 1$. Therefore $S_{\rho,q} \rightarrow P_{0,q}$ and $W_{\rho,q} \rightarrow I_{T_0} - P_{0,q}$.

Since these limits agree with the boundary definitions (9) and (10), both families admit unique continuous extensions to $[0, 1]$.

Part (ii): positive semidefiniteness. For $\rho \in (0, 1)$, the eigenvalues $w_k(\rho) \geq 0$ for all k , so $W_{\rho,q} \succeq 0$. At the endpoints, $W_{0,q} = K = D'_q D_q \succeq 0$ and $W_{1,q} = I_{T_0} - P_{0,q}$ is an orthogonal projector, hence positive semidefinite. \square

A.2. Proofs for Section 5

A.2.1. Proof of Proposition 3

Term A. From the oracle predictor (24) and the HSC counterfactual:

$$\begin{aligned} \text{Term A}(\rho) &= \tilde{Y}_{\text{post}}^{\text{oracle}}(0; \rho) - \hat{Y}_{\text{post}}(0; \rho, q) \\ &= X_{\text{post}} \omega^{\text{oracle}} + \Pi_\rho r_{\text{pre}}^{\text{oracle}} - X_{\text{post}} \hat{\omega} - \Pi_\rho r_{\text{pre}}(\hat{\omega}) \\ &= X_{\text{post}}(\omega^{\text{oracle}} - \hat{\omega}) + \Pi_\rho(r_{\text{pre}}^{\text{oracle}} - r_{\text{pre}}(\hat{\omega})). \end{aligned}$$

Since $r_{\text{pre}}(\omega) = Y_{\text{pre}} - X_{\text{pre}}\omega$ is linear in ω , $r_{\text{pre}}^{\text{oracle}} - r_{\text{pre}}(\hat{\omega}) = -X_{\text{pre}}(\omega^{\text{oracle}} - \hat{\omega})$, so

$$\text{Term A}(\rho) = (X_{\text{post}} - \Pi_\rho X_{\text{pre}})(\omega^{\text{oracle}} - \hat{\omega}).$$

Term B. From the definition (25) and the oracle predictor (24):

$$\begin{aligned} \text{Term B}(\rho) &= Y_{\text{post}}(0) - \tilde{Y}_{\text{post}}^{\text{oracle}}(0; \rho) \\ &= Y_{\text{post}}(0) - X_{\text{post}} \omega^{\text{oracle}} - \Pi_\rho r_{\text{pre}}^{\text{oracle}} \\ &= (Y_{\text{post}}(0) - X_{\text{post}} \omega^{\text{oracle}}) - \Pi_\rho (Y_{\text{pre}} - X_{\text{pre}} \omega^{\text{oracle}}). \end{aligned}$$

\square

A.2.2. Gradient decomposition

The proof of Proposition 4 relies on an exact decomposition of the gradient discrepancy between the HSC and oracle objectives at the oracle weights.

Lemma A1 (Gradient decomposition at ω^{oracle}). Let F_ρ and H^{oracle} be defined by (28)–(29). Then

$$\frac{1}{2}(\nabla F_\rho(\omega^{\text{oracle}}) - \nabla H^{\text{oracle}}(\omega^{\text{oracle}})) = \underbrace{-L'_{0,\text{pre}}(W_\rho - P_\perp)e_{\text{pre}}^L}_{g_1} - \underbrace{\mathcal{R}'_{0,\text{pre}}W_\rho e_{\text{pre}}^L}_{g_2} - \underbrace{X'_{\text{pre}}W_\rho e_{\text{pre}}^{\mathcal{R}}}_{g_3}. \quad (\text{A6})$$

Proof The gradients are

$$\begin{aligned} \nabla F_\rho(\omega) &= -2X'_{\text{pre}}W_\rho r_{\text{pre}}(\omega) + 2\zeta^2 T_0\omega, \\ \nabla H^{\text{oracle}}(\omega) &= -2L'_{0,\text{pre}}P_\perp(L_{1,\text{pre}} - L_{0,\text{pre}}\omega) + 2\zeta^2 T_0\omega. \end{aligned}$$

At $\omega = \omega^{\text{oracle}}$, the ridge terms cancel. For the oracle objective, $P_\perp(L_{1,\text{pre}} - L_{0,\text{pre}}\omega^{\text{oracle}}) = P_\perp e_{\text{pre}}^L$. For the HSC objective, $r_{\text{pre}}(\omega^{\text{oracle}}) = r_{\text{pre}}^{\text{oracle}} = e_{\text{pre}}^L + e_{\text{pre}}^{\mathcal{R}}$. Since $P_0 e_{\text{pre}}^L \in \text{Null}(K)$ and W_ρ annihilates $\text{Null}(K)$ (Proposition 2), $W_\rho r_{\text{pre}}^{\text{oracle}} = W_\rho e_{\text{pre}}^L + W_\rho e_{\text{pre}}^{\mathcal{R}}$. Expanding $X_{\text{pre}} = L_{0,\text{pre}} + \mathcal{R}_{0,\text{pre}}$:

$$\begin{aligned} \frac{1}{2}(\nabla F_\rho(\omega^{\text{oracle}}) - \nabla H^{\text{oracle}}(\omega^{\text{oracle}})) &= -X'_{\text{pre}}W_\rho(e_{\text{pre}}^L + e_{\text{pre}}^{\mathcal{R}}) + L'_{0,\text{pre}}P_\perp e_{\text{pre}}^L \\ &= -L'_{0,\text{pre}}W_\rho e_{\text{pre}}^L - \mathcal{R}'_{0,\text{pre}}W_\rho e_{\text{pre}}^L - X'_{\text{pre}}W_\rho e_{\text{pre}}^{\mathcal{R}} + L'_{0,\text{pre}}P_\perp e_{\text{pre}}^L \\ &= -L'_{0,\text{pre}}(W_\rho - P_\perp)e_{\text{pre}}^L - \mathcal{R}'_{0,\text{pre}}W_\rho e_{\text{pre}}^L - X'_{\text{pre}}W_\rho e_{\text{pre}}^{\mathcal{R}}, \end{aligned}$$

where the last line groups $-L'_{0,\text{pre}}W_\rho e_{\text{pre}}^L + L'_{0,\text{pre}}P_\perp e_{\text{pre}}^L = -L'_{0,\text{pre}}(W_\rho - P_\perp)e_{\text{pre}}^L$. \square

A.2.3. Constrained minimizer gap

Lemma A2. Let $\hat{\omega}(\rho) \in \arg \min_{\omega \in \Delta_{N_0}} F_\rho(\omega)$ and $\omega^{\text{oracle}} \in \arg \min_{\omega \in \Delta_{N_0}} H^{\text{oracle}}(\omega)$. Then

$$\|\omega^{\text{oracle}} - \hat{\omega}(\rho)\|_{Q_\rho} \leq \frac{1}{2T_0} \|\nabla F_\rho(\omega^{\text{oracle}}) - \nabla H^{\text{oracle}}(\omega^{\text{oracle}})\|_{Q_\rho^{-1}}. \quad (\text{A7})$$

Proof Let $d := \omega^{\text{oracle}} - \hat{\omega}(\rho)$. The minimizers of the convex differentiable functions F_ρ and H^{oracle} over the closed convex set Δ_{N_0} satisfy the variational inequalities

$$\langle \nabla F_\rho(\hat{\omega}), \omega - \hat{\omega} \rangle \geq 0 \quad \forall \omega \in \Delta_{N_0}, \quad \langle \nabla H^{\text{oracle}}(\omega^{\text{oracle}}), \omega - \omega^{\text{oracle}} \rangle \geq 0 \quad \forall \omega \in \Delta_{N_0}.$$

Setting $\omega = \omega^{\text{oracle}}$ in the first and $\omega = \hat{\omega}$ in the second, then adding:

$$\langle \nabla F_\rho(\hat{\omega}) - \nabla H^{\text{oracle}}(\omega^{\text{oracle}}), d \rangle \geq 0.$$

Inserting $\pm \nabla F_\rho(\omega^{\text{oracle}})$ and using $\nabla F_\rho(\hat{\omega}) - \nabla F_\rho(\omega^{\text{oracle}}) = -2T_0 Q_\rho d$ (since F_ρ is quadratic with

Hessian $2T_0Q_\rho$):

$$2T_0\|d\|_{Q_\rho}^2 \leq \langle \nabla F_\rho(\omega^{\text{oracle}}) - \nabla H^{\text{oracle}}(\omega^{\text{oracle}}), d \rangle \leq \|\nabla F_\rho(\omega^{\text{oracle}}) - \nabla H^{\text{oracle}}(\omega^{\text{oracle}})\|_{Q_\rho^{-1}} \|d\|_{Q_\rho},$$

where the last step is the generalized Cauchy–Schwarz inequality. Dividing both sides by $2T_0\|d\|_{Q_\rho}$ (the claim is trivial if $d = 0$) yields (A7). \square

A.2.4. Dual-norm bound

Lemma A3 (Dual-norm bound). For any $u \in \mathbb{R}^{T_0}$,

$$\frac{1}{T_0} \|X'_{\text{pre}} W_\rho u\|_{Q_\rho^{-1}} \leq \frac{1}{\sqrt{T_0}} \|u\|_{W_\rho}. \quad (\text{A8})$$

Proof Set $b := W_\rho^{1/2} u$ and $\tilde{X} := T_0^{-1/2} W_\rho^{1/2} X_{\text{pre}}$, so that $Q_\rho = \tilde{X}' \tilde{X} + \zeta^2 I_{N_0}$ and $X'_{\text{pre}} W_\rho u = \sqrt{T_0} \tilde{X}' b$. Then

$$\frac{1}{T_0^2} \|X'_{\text{pre}} W_\rho u\|_{Q_\rho^{-1}}^2 = \frac{1}{T_0} b' \tilde{X} (\tilde{X}' \tilde{X} + \zeta^2 I)^{-1} \tilde{X}' b.$$

Using a compact SVD $\tilde{X} = U \Sigma V'$, we have $\tilde{X} (\tilde{X}' \tilde{X} + \zeta^2 I)^{-1} \tilde{X}' = U \text{diag}(\sigma_i^2 / (\sigma_i^2 + \zeta^2)) U' \preceq I_{T_0}$, so the expression is bounded by $T_0^{-1} \|b\|_2^2 = T_0^{-1} \|u\|_{W_\rho}^2$. \square

A.2.5. Proof of Proposition 4

Proof The proof proceeds in three steps.

Step 1: gradient decomposition. By Lemma A1, the gradient discrepancy at ω^{oracle} decomposes as $\frac{1}{2}(\nabla F_\rho(\omega^{\text{oracle}}) - \nabla H^{\text{oracle}}(\omega^{\text{oracle}})) = -(g_1 + g_2 + g_3)$, with g_1, g_2, g_3 as in (A6).

Step 2: weight gap bound. From Lemma A2 and the triangle inequality:

$$\|\omega^{\text{oracle}} - \hat{\omega}\|_{Q_\rho} \leq \frac{1}{T_0} \|g_1\|_{Q_\rho^{-1}} + \frac{1}{T_0} \|g_2\|_{Q_\rho^{-1}} + \frac{1}{T_0} \|X'_{\text{pre}} W_\rho e_{\text{pre}}^{\mathcal{R}}\|_{Q_\rho^{-1}}.$$

The first two terms equal A_1 and A_2 by definition (30)–(31). Applying Lemma A3 with $u = e_{\text{pre}}^{\mathcal{R}}$ to the third term gives A_3 as defined in (32). Hence $\|\omega^{\text{oracle}} - \hat{\omega}\|_{Q_\rho} \leq A_1 + A_2 + A_3$.

Step 3: transfer to prediction error. From (26), insert $Q_\rho^{-1/2} Q_\rho^{1/2}$:

$$\|\text{Term A}(\rho)\|_2 = \|C_\rho(\omega^{\text{oracle}} - \hat{\omega})\|_2 \leq \|C_\rho Q_\rho^{-1/2}\|_{\text{op}} \|\omega^{\text{oracle}} - \hat{\omega}\|_{Q_\rho} = \mathcal{P}_\rho \|\omega^{\text{oracle}} - \hat{\omega}\|_{Q_\rho} \leq \mathcal{P}_\rho (A_1 + A_2 + A_3).$$

\square

A.2.6. Proof of (37)

Proof From the closed form (27),

$$\text{Term B}(\rho) = r_{\text{post}}^{\text{oracle}} - \Pi_{\rho} r_{\text{pre}}^{\text{oracle}}.$$

Decompose the pre-period residual along $\text{Null}(K)$ and its orthogonal complement: $r_{\text{pre}}^{\text{oracle}} = P_0 r_{\text{pre}}^{\text{oracle}} + \eta_{\text{pre}}^{\text{oracle}}$ by (36). Because S_{ρ} fixes $\text{Null}(K)$ (Proposition 2), $S_{\rho}(P_0 r_{\text{pre}}^{\text{oracle}}) = P_0 r_{\text{pre}}^{\text{oracle}}$, and because \tilde{G}_q satisfies the null-space continuation property $\tilde{G}_q v = G_q^{\text{null}} v$ for every $v \in \text{Null}(K)$ of Section 3.3,

$$\Pi_{\rho}(P_0 r_{\text{pre}}^{\text{oracle}}) = \tilde{G}_q(P_0 r_{\text{pre}}^{\text{oracle}}) = G_q^{\text{null}} P_0 r_{\text{pre}}^{\text{oracle}}.$$

Therefore

$$\begin{aligned} \text{Term B}(\rho) &= r_{\text{post}}^{\text{oracle}} - \Pi_{\rho}(P_0 r_{\text{pre}}^{\text{oracle}}) - \Pi_{\rho} \eta_{\text{pre}}^{\text{oracle}} \\ &= r_{\text{post}}^{\text{oracle}} - G_q^{\text{null}} P_0 r_{\text{pre}}^{\text{oracle}} - \tilde{G}_q S_{\rho} \eta_{\text{pre}}^{\text{oracle}} \\ &= \eta_{\text{post}}^{\text{oracle}} - \tilde{G}_q S_{\rho} \eta_{\text{pre}}^{\text{oracle}}, \end{aligned}$$

using the definition of $\eta_{\text{post}}^{\text{oracle}}$ in (36). □

B. Monte Carlo evaluation of the prediction-error decomposition

This appendix reports a Monte Carlo study that evaluates the prediction-error decomposition of Section 5 along the ρ -grid. The goals are: (i) to display the three Term A channels of Section 5.3 and the identification geometry encoded in Q_ρ^{-1} and \mathcal{P}_ρ ; (ii) to exhibit how the ρ -profile of Term B varies with the forecaster \tilde{G}_q (Section 5.4); and (iii) to show how Term A and Term B combine into the ρ -shape of the prediction error across four (q, \tilde{G}_q) configurations under two DGP regimes.

B.1. Setup

Data generating process. For each replication we simulate panel data $Y_{it} = \Lambda_i F_t + \kappa R_{it}^{\text{rw}} + \varepsilon_{it}$ on $i \in \{0, 1, \dots, N_0\}$ (one treated unit and N_0 donors) and $t \in \{1, \dots, T_0 + T_{\text{post}}\}$. The single common factor $F_t = \sum_{s \leq t} u_s$ is a random walk with $u_s \sim N(0, 1)$. The loadings $\Lambda_i \sim N(1, 0.5^2)$ are drawn once per replication and held fixed across t . The unit-specific random walks $R_{it}^{\text{rw}} = \sum_{s \leq t} v_{is}$ have $v_{is} \sim N(0, 1)$. The idiosyncratic short-run noise $\varepsilon_{it} \sim N(0, 0.5^2)$ is iid across (i, t) . The residual is then $\mathcal{R}_{it} = \kappa R_{it}^{\text{rw}} + \varepsilon_{it}$, and the observed outcome decomposes as $Y_{it} = L_{it} + \mathcal{R}_{it}$ with $L_{it} = \Lambda_i F_t$. We set $N_0 = 10$, $T_0 = 80$, $T_{\text{post}} = 5$, and the ridge parameter $\zeta = T_{\text{post}}^{1/4} \hat{\sigma}_{\Delta X}$ as in [Arkhangelsky et al. \(2021\)](#), where $\hat{\sigma}_{\Delta X}$ is the empirical standard deviation of the first-differenced donor pre-period series.

Two experiments. We consider two values of κ , corresponding to the regimes of Section 2.5:

- *Shared stochastic trend regime* ($\kappa = 0$): \mathcal{R} reduces to idiosyncratic short-run noise.
- *Shared + idiosyncratic stochastic trend regime* ($\kappa = 2$): each unit carries an independent random walk in addition to the idiosyncratic short-run noise.

Four configurations. For each replication we estimate HSC under four configurations. All four use the admissible forecast operator $\tilde{G}_q = G_q^{\text{null}} P_{0,q} + \hat{G}_q P_{\perp,q}$ of Section 3.3: the null-space part of the pre-period residual, $P_{0,q} r$, is always continued by the canonical operator G_q^{null} (a constant for $q = 1$, an intercept-plus-linear trend for $q = 2$), while the data-driven component \hat{G}_q acts only on the non-null part $P_{\perp,q} r$. The configurations differ in the smoothness order q and in the choice of \hat{G}_q :

- ($q = 1$, G_1^{const}): \hat{G}_1 is the constant carry-forward, holding the last value of the non-null part flat. Recombined with the continued null-space mean, the two parts collapse to the raw last residual r_{T_0} held constant across the post-period window.
- ($q = 1$, ARIMA(1, 1, 0)): \hat{G}_1 is an ARIMA(1, 1, 0) model fitted to the non-null part of the pre-period residual, with the null-space mean continued exactly as above.

- ($q = 2$, G_2^{const}): \hat{G}_2 is again the constant carry-forward on the non-null part. Recombined with the canonical intercept-plus-linear continuation on $\text{Null}(K_2)$, the composed forecast at horizon h is $r_{T_0} + \hat{\beta} h$, where $\hat{\beta}$ is the slope of the line fitted to the pre-period residual over $\text{Null}(K_2)$; equivalently, the fitted linear trend is extrapolated with its level re-anchored to the last observed residual r_{T_0} .
- ($q = 2$, $\text{ARIMA}(1, 1, 0)$): \hat{G}_2 is an $\text{ARIMA}(1, 1, 0)$ model on the non-null part, with the null-space intercept-plus-linear trend continued by G_2^{null} .

Grid in ρ . For every simulation round we sweep ρ over the 19-point grid $\{0, 0.05, 0.1, 0.2, 0.3, \dots, 0.8, 0.85, 0.9, 0.93, 0.95, 0.97, 0.98, 0.99, 0.995, 1\}$, denser near $\rho = 1$ where the most rapid changes occur.

Computed quantities. At every simulation round we compute the squared prediction error and its RMSE counterpart $\sqrt{T_{\text{post}}^{-1} \sum_t (\cdot)^2}$, the norms $\|\text{Term A}(\rho)\|_2$ and $\|\text{Term B}(\rho)\|_2$ from the closed forms (26)–(27), the three channels A_1, A_2, A_3 of (30)–(32), $\lambda_{\max}(Q_\rho^{-1})$, and the transfer multiplier $\mathcal{P}_\rho = \|C_\rho Q_\rho^{-1/2}\|_{\text{op}}$, and average them across $B = 200$ replications. The design is run twice: with the baseline ridge $\zeta = T_{\text{post}}^{1/4} \hat{\sigma}_{\Delta X}$ and with $\zeta = 0$, to isolate the stabilizing role of the ridge.

B.2. Term A: channels and identification geometry

The channels A_1, A_2, A_3 and $\lambda_{\max}(Q_\rho^{-1})$ depend on the data and the penalty K_q but not on \tilde{G}_q , so we report them at one configuration per q (G_1^{const} and G_2^{const}); the transfer multiplier $\mathcal{P}_\rho = \|C_\rho Q_\rho^{-1/2}\|_{\text{op}}$ depends on \tilde{G}_q through $C_\rho = X_{\text{post}} - \Pi_\rho X_{\text{pre}}$ and is reported for all four configurations.

Three channels. Figure B1 (top) plots the three channels of Section 5.3. The metric-distortion channel A_1 is hump-shaped and vanishes at $\rho = 1$ (where $W_\rho = P_\perp$). The interaction channel A_2 is uniformly small and never the binding channel. The spurious matching channel $A_3 = T_0^{-1/2} \|e_{\text{pre}}^{\mathcal{R}}\|_{W_\rho}$ stays small and bounded in the shared stochastic trend regime; in the shared + idiosyncratic regime it is controlled at small ρ , where the q th differencing in $W_0 = K_q$ stationarizes the unit-specific random walks, and rises sharply toward $\rho = 1$ as W_ρ retains their low-frequency content.

Identification geometry. Figure B1 (bottom) plots $\lambda_{\max}(Q_\rho^{-1})$ (Lemma A2). Since $Q_\rho \succeq \zeta^2 I_{N_0}$, the bound $\lambda_{\max}(Q_\rho^{-1}) \leq 1/\zeta^2$ holds for every ρ . The ridged profile is nearly flat, around 0.25 in the shared stochastic trend regime and around 0.065 in the shared + idiosyncratic regime. With $\zeta = 0$ (Figure B2) it is markedly larger and far more variable, demonstrating the stabilizing role of the ridge.

Transfer multiplier. Figure B3 reports \mathcal{P}_ρ , the ρ -dependent factor multiplying $A_1 + A_2 + A_3$ in the envelope of Proposition 4. In every configuration \mathcal{P}_ρ is larger in the shared + idiosyncratic regime, peaking near 8, than in the shared stochastic trend regime, where it peaks near 3 for the $q = 1$ configurations and near 4–5 for the $q = 2$ configurations (largest under the $q = 2$ ARIMA(1, 1, 0) forecaster).

Tightness of the envelope. Figure B4 overlays $\mathcal{P}_\rho(A_1 + A_2 + A_3)$ with the realized $\|\text{Term A}(\rho)\|$. In every ridged cell and at every grid point the envelope lies weakly above the realized norm, confirming Proposition 4 numerically. It is conservative, exceeding $\|\text{Term A}\|$ by roughly five- to eighteenfold, the gap being largest where $\|\text{Term A}\|$ is smallest, in the shared stochastic trend regime.

B.3. Synthesis: Term A, Term B, and the ρ -shape of the prediction error

Figure B5 overlays the per-period RMSE with the per-period norms of Term A and Term B. Across every panel $\|\text{Term B}\|$ exceeds $\|\text{Term A}\|$ throughout the grid, so forecasting is the dominant contributor to the prediction error; and the ρ -shape of $\|\text{Term B}\|$ is configuration-specific, neither monotone nor uniformly oriented across the four (q, \tilde{G}_q) cells (Section 5.4).

Shared stochastic trend regime ($\kappa = 0$). The RMSE is low, with mean RMSE ≈ 0.70 – 0.77 at the optimum (Table B1). $\|\text{Term B}\|$ is the larger term throughout (per-period ≈ 0.6 against ≈ 0.1 – 0.2 for $\|\text{Term A}\|$), but both are small in absolute terms ($\|\text{B}\| \approx 1.4$, $\|\text{A}\| \approx 0.3$ – 0.5 at the optimum).

Shared + idiosyncratic stochastic trend regime ($\kappa = 2$). Both terms grow and Term B dominates: at the optimum $\|\text{Term B}\| \approx 7.2$ – 7.4 against $\|\text{Term A}\| \approx 1.1$ – 1.6 , roughly a factor of five. The ex-post RMSE-minimizing ρ^* is small for every configuration (between 0 and 0.30), the mean RMSE is ≈ 3.3 , and the RMSE rises toward $\rho = 1$ (Table B1).

Role of ridge regularization. In the shared stochastic trend regime the no-ridge RMSE is lower (e.g. 0.60 vs. 0.71 for $q = 1$, G_1^{const}), since without the ridge bias the estimator matches more precisely when identification is strong. In the shared + idiosyncratic regime removing the ridge inflates $\|\text{Term A}\|$ by roughly 2.8–3.7 \times yet the RMSE barely moves (e.g. 3.41 vs. 3.32), because Term B dominates and is largely unaffected by the ridge. The ridge thus stabilizes weight estimation but has little effect on RMSE when forecasting error binds.

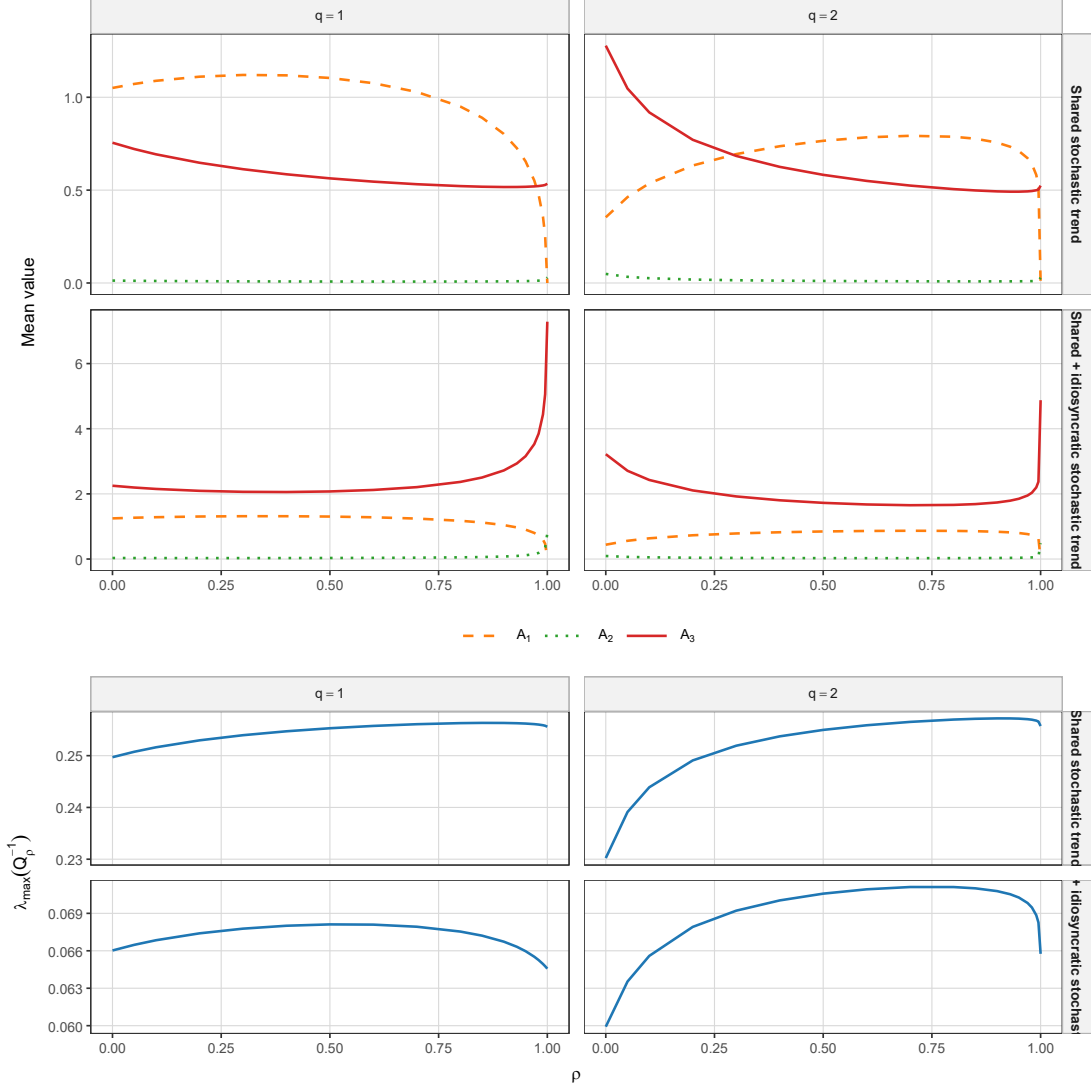


Figure B1. TERM A CHANNELS AND IDENTIFICATION GEOMETRY.

Note: Top row: the three channels of the Term A envelope of Proposition 4, plotted as a function of ρ . Orange dashed: A_1 , the metric-distortion channel. Green dotted: A_2 , the interaction channel. Red solid: A_3 , the spurious matching channel. Bottom row: $\lambda_{\max}(Q_{\rho}^{-1})$, the largest eigenvalue of the inverse of the Hessian $Q_{\rho} = T_0^{-1} X'_{\text{pre}} W_{\rho} X_{\text{pre}} + \zeta^2 I_{N_0}$. Columns correspond to the representative configurations ($q = 1, G_1^{\text{const}}$) and ($q = 2, G_2^{\text{const}}$). Top facet within each column: shared stochastic trend regime ($\kappa = 0$). Bottom facet: shared + idiosyncratic stochastic trend regime ($\kappa = 2$). All curves are means over $B = 200$ replications of the DGP described in Section B.1; ridge parameter $\zeta = T_{\text{post}}^{1/4} \hat{\sigma}_{\Delta X}$.

B.4. Summary and limitations

The Monte Carlo evidence matches Section 5: several channel profiles are non-monotone in ρ , and Term B consistently exceeds Term A (roughly fivefold at the optimum in the shared + idiosyncratic regime, threefold to fivefold in the shared stochastic trend regime). The ex-post RMSE-minimizing

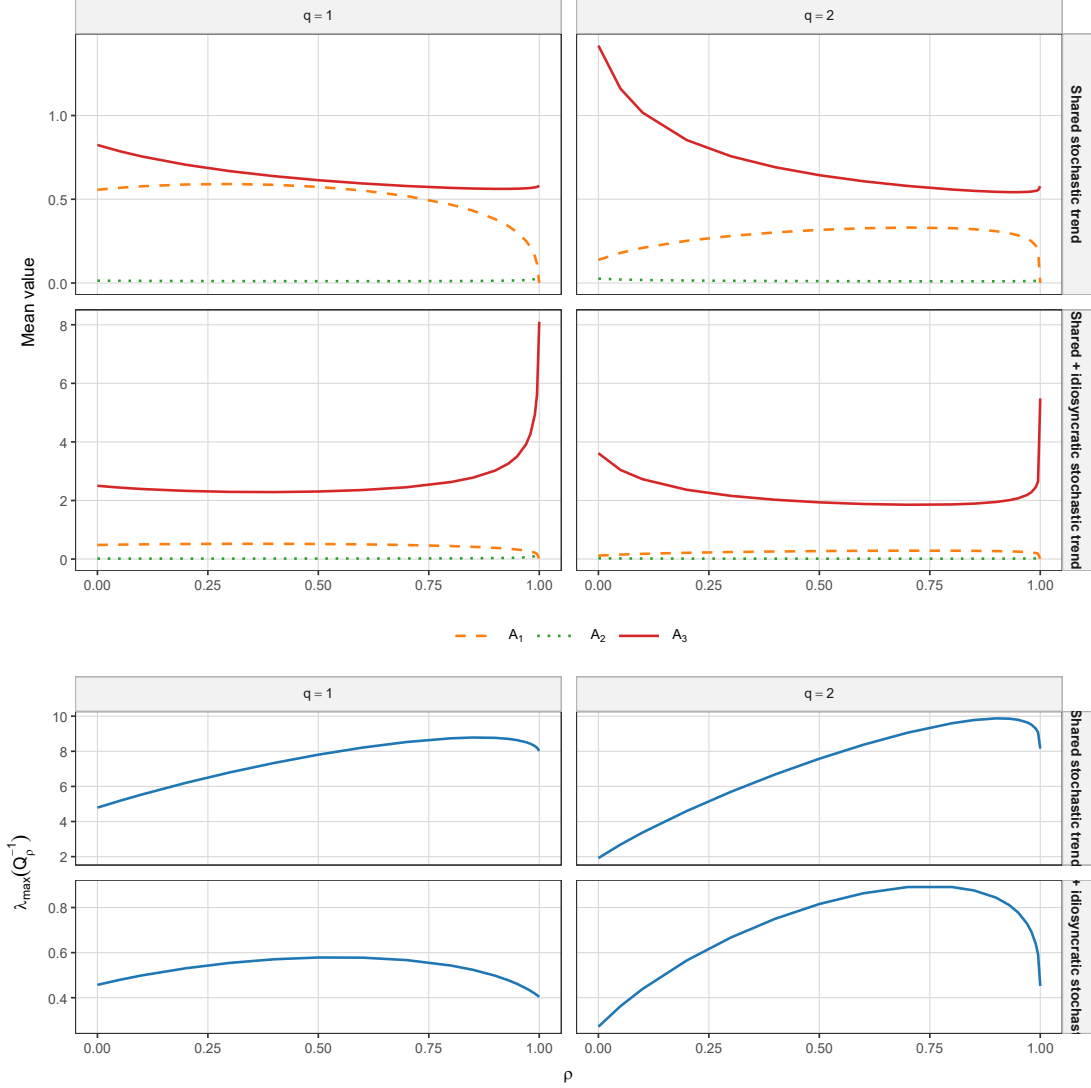


Figure B2. TERM A CHANNELS AND IDENTIFICATION GEOMETRY WITHOUT RIDGE REGULARIZATION ($\zeta = 0$).

Note: Same layout as Figure B1 but with $\zeta = 0$ (no ridge regularization). Without the ridge floor, $\lambda_{\max}(Q_p^{-1})$ can grow much larger, demonstrating the stabilizing role of the ridge term. The A_1 , A_2 , A_3 channels in the top row are also computed at $\zeta = 0$.

ρ is small throughout the shared + idiosyncratic regime; it depends jointly on the DGP and the forecaster \tilde{G}_q (Section 5.5).

Three caveats apply. The design fixes $N_0 = 10$, $T_0 = 80$, $T_{\text{post}} = 5$; the channel magnitudes and the location of the RMSE minimum depend on T_0 and on $\sigma_\Lambda/\sigma_\varepsilon$. The persistent part of \mathcal{R} is a unit-specific random walk; richer time series processes would change the relative magnitudes of A_3 and may shift the optimal ρ . And the figures are sample means over $B = 200$ replications.

Cross-validation (Section 4.2) navigates this landscape empirically, with ρ allocating the pre-

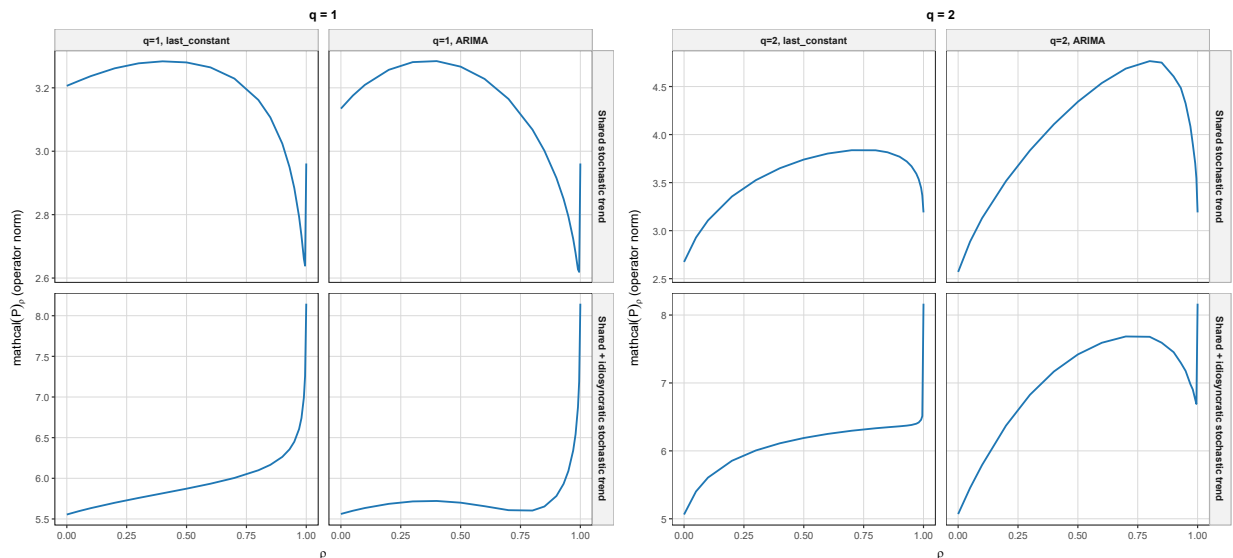


Figure B3. TRANSFER MULTIPLIER \mathcal{P}_ρ .

Note: Mean operator norm $\mathcal{P}_\rho = \|C_\rho Q_\rho^{-1/2}\|_{\text{op}}$ as a function of ρ , where $C_\rho := X_{\text{post}} - \Pi_\rho X_{\text{pre}}$. Left panel: $q = 1$. Right panel: $q = 2$. Within each panel, columns are the two estimator configurations (G_q^{const} and ARIMA(1, 1, 0)) and rows are the two DGP regimes (shared stochastic trend on top, shared + idiosyncratic stochastic trend on bottom). Means are over $B = 200$ replications.

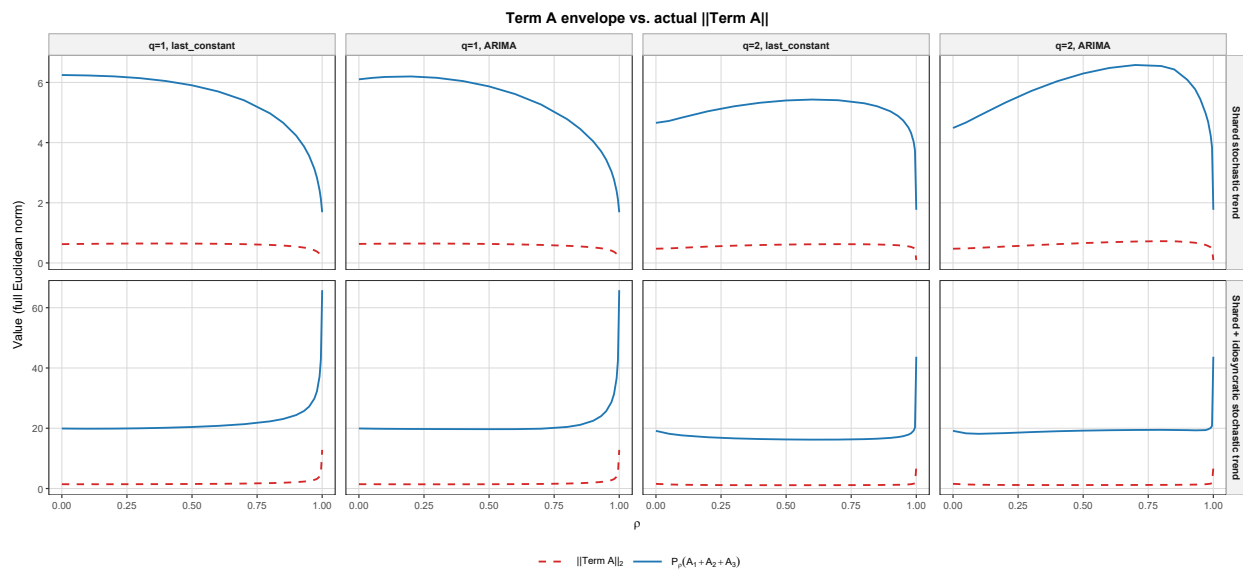


Figure B4. TIGHTNESS OF THE TERM A ENVELOPE.

Note: Mean Term A envelope $\mathcal{P}_\rho(A_1 + A_2 + A_3)$ of Proposition 4 (orange dashed) and the mean realized norm $\|\text{Term A}(\rho)\|_2$ (black solid), as functions of ρ . Left panel: $q = 1$. Right panel: $q = 2$. Within each panel, columns are the two estimator configurations (G_q^{const} and ARIMA(1, 1, 0)) and rows are the two DGP regimes (shared stochastic trend on top, shared + idiosyncratic stochastic trend on bottom). The envelope lies weakly above the realized norm at every grid point in every cell, confirming Proposition 4 numerically; the gap measures the conservativeness of the uniform bound. Means are over $B = 200$ replications; ridge parameter $\zeta = T_{\text{post}}^{1/4} \hat{\sigma}_{\Delta X}$.

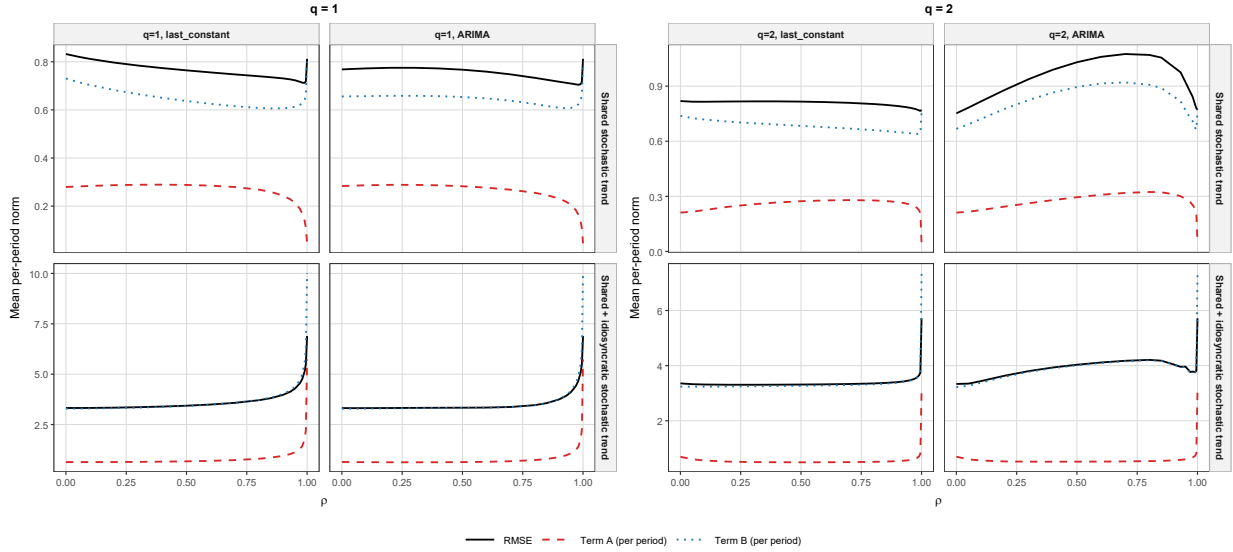


Figure B5. PER-PERIOD RMSE, Term A, AND Term B.

Note: Mean per-period RMSE (black solid), mean per-period $\|\text{Term A}(\rho)\|_2/\sqrt{T_{\text{post}}}$ (red dashed), and mean per-period $\|\text{Term B}(\rho)\|_2/\sqrt{T_{\text{post}}}$ (blue dotted) as functions of ρ . Left panel: $q = 1$. Right panel: $q = 2$. Within each panel, columns are the two estimator configurations (G_q^{const} and ARIMA(1, 1, 0)) and rows are the two DGP regimes (shared stochastic trend on top, shared + idiosyncratic stochastic trend on bottom). Per-period normalization places the three curves on the same scale as the RMSE, which is the square root of the per-period mean squared error. Means are over $B = 200$ replications.

period information between weight estimation (Term A) and forecasting (Term B), and the channels of Sections 5.3–5.4 accounting for the shapes it traces.

Table B1. EX-POST RMSE-MINIMIZING ρ^* , MEAN RMSE, AND THE CORRESPONDING MEAN NORMS OF Term A AND Term B AT THE OPTIMUM.

Configuration	Shared stochastic trend ($\kappa = 0$)				Shared + idiosyncratic stochastic trend ($\kappa = 2$)			
	ρ^*	RMSE	$\ A\ $	$\ B\ $	ρ^*	RMSE	$\ A\ $	$\ B\ $
<i>Panel A: Ridge regularization $\zeta = T_{\text{post}}^{1/4} \hat{\sigma}_{\Delta X}$ (default)</i>								
$q = 1, G_1^{\text{const}}$	0.990	0.71	0.31	1.44	0.050	3.32	1.42	7.36
$q = 1, \text{ARIMA}(1, 1, 0)$	0.980	0.70	0.37	1.39	0.050	3.31	1.42	7.35
$q = 2, G_2^{\text{const}}$	0.995	0.76	0.47	1.44	0.300	3.31	1.12	7.27
$q = 2, \text{ARIMA}(1, 1, 0)$	0.000	0.75	0.47	1.49	0.000	3.34	1.56	7.20
<i>Panel B: No ridge regularization ($\zeta = 0$)</i>								
$q = 1, G_1^{\text{const}}$	0.970	0.60	0.46	1.35	0.100	3.41	4.05	8.06
$q = 1, \text{ARIMA}(1, 1, 0)$	0.970	0.60	0.46	1.35	0.200	3.39	4.00	7.96
$q = 2, G_2^{\text{const}}$	0.995	0.63	0.61	1.41	0.700	3.39	4.15	8.15
$q = 2, \text{ARIMA}(1, 1, 0)$	1.000	0.63	0.45	1.40	0.000	3.47	4.33	7.85

Notes: Each entry reports the ex-post RMSE-minimizing grid value ρ^* on the 19-point grid that minimizes mean per-period RMSE over $B = 200$ replications, the corresponding mean RMSE, and the mean Euclidean norms $\|\text{Term A}(\rho^*)\|_2$ and $\|\text{Term B}(\rho^*)\|_2$ at the same ρ^* . This ρ^* is an ex-post RMSE minimizer and is distinct from the cross-validation selector $\hat{\rho}$ of Section 4.2. RMSE is the per-period quantity $\sqrt{T_{\text{post}}^{-1} \sum_t (\cdot)^2}$, while $\|\text{Term A}\|$ and $\|\text{Term B}\|$ are full Euclidean norms over the post-treatment window of length $T_{\text{post}} = 5$; dividing the latter by $\sqrt{T_{\text{post}}} \approx 2.24$ converts them to the same per-period scale as the RMSE column. The DGP is described in Section B.1, with $N_0 = 10$, $T_0 = 80$, $T_{\text{post}} = 5$, $\sigma_\Lambda = \sigma_\varepsilon = 0.5$. Panel A uses the default ridge parameter $\zeta = T_{\text{post}}^{1/4} \hat{\sigma}_{\Delta X}$; Panel B sets $\zeta = 0$.

C. Monte Carlo robustness for the estimator comparison

This appendix supplements the Monte Carlo evidence of Section 6. Section C.1 reports the simulation details, including the parameter values for the data-generating process, the seed scheme, and the frozen-versus-redrawn split for each component of the panel. Section C.2 reports the per-period RMSE trajectory that underlies the pooled-RMSE comparison of Section 6.2. Section C.3 decomposes the pooled RMSE into pooled bias and pooled variance and briefly attributes HSC’s RMSE advantage to a variance reduction. Section C.4 compares the cross-validated $\hat{\rho}$ and post-period RMSE between $h = 1$ and $h = 20$ cross-validation.

C.1. Simulation details

The data-generating process used throughout Section 6 and this appendix is

$$Y_{j,t}(0) = L_{j,t} + \kappa \mathcal{E}_{j,t} + \varepsilon_{j,t} + \alpha_j + \delta_t, \quad j \in \{0, 1, \dots, N_0\}, \quad t \in \{1, \dots, T_0 + T_{\text{post}}\}, \quad (\text{C1})$$

where the index $j = 0$ denotes the treated unit and $j = 1, \dots, N_0$ denote the donors (this appendix indexes the treated unit as $j = 0$ for notational convenience in the DGP). The treated unit receives no treatment effect ($\tau = 0$), so the post-period error of any counterfactual estimator \hat{Y}_{0,T_0+h} is $\hat{Y}_{0,T_0+h} - Y_{0,T_0+h}(0)$.

Low-rank component. The component $L_{j,t}$ is built from $K = 3$ latent factors:

$$L_{j,t} = \sum_{k=1}^3 \Lambda_{j,k} F_{k,t}, \quad (\text{C2})$$

where $F_{1,t}$ is a random walk with innovation variance $\sigma_{\text{rw}}^2 = 4$, $F_{2,t}$ is an integrated ARIMA(1, 1, 0) process with autoregressive coefficient $\phi_F = 0.5$ and innovation variance $\sigma_{\text{arima}}^2 = 4$, and $F_{3,t}$ is a stationary AR(1) with autoregressive coefficient $\rho_s = 0.6$ and innovation variance $\sigma_s^2 = 1$. The factor paths $F_{k,t}$ are drawn fresh in every replication. The loadings $\Lambda_{j,k}$ for the donors are drawn iid from $\mathcal{N}(0, 0.5^2)$ and truncated to $[-2, 2]$, and are held fixed across replications.

Treated loading. The treated unit’s loading vector is the convex combination

$$\lambda_0 = \sum_{j \in \mathcal{S}} \omega_j^* \Lambda_{j,\cdot}, \quad \omega^* \in \Delta_{N_0}, \quad |\mathcal{S}| = 8, \quad (\text{C3})$$

where $\mathcal{S} \subset \{1, \dots, N_0\}$ is a uniformly drawn support of eight donors and ω^* is drawn from a sparse Dirichlet distribution on that support. By construction λ_0 lies inside the convex hull of the donor loadings. The treated loading is held fixed across replications.

Idiosyncratic stochastic trend. The component $\mathcal{E}_{j,t}$ is a unit-specific ARIMA(1, 1, 0) process with autoregressive coefficient $\phi_e = 0.25$. Its innovation $U_{j,t}$ mixes a common shock and an idiosyncratic shock:

$$U_{j,t} = \sqrt{\rho_u} u_t^c + \sqrt{1 - \rho_u} u_{j,t}^i, \quad (\text{C4})$$

with $u_t^c, u_{j,t}^i \sim \mathcal{N}(0, 1 - \phi_e^2)$ iid. The amplitude $\kappa \in \{0, 0.5, 1, 2\}$ scales the entire $\mathcal{E}_{j,t}$ component, and the cross-unit correlation parameter $\rho_u \in \{0, 0.5, 1\}$ continuously interpolates between purely idiosyncratic drift and purely shared drift. Both shocks are drawn fresh in every replication.

Stationary noise and fixed effects. The stationary noise $\varepsilon_{j,t}$ is iid $\mathcal{N}(0, 1)$ and is drawn fresh in every replication. The unit fixed effect α_j is drawn iid from $U(5, 15)$ for the donors and fixed at $\alpha_0 = 0$ for the treated unit; the unit fixed effects are held fixed across replications. The time fixed effect $\delta_t \sim \mathcal{N}(0, 1)$ is iid and is drawn fresh in every replication.

Sample sizes and grid. We use $T_0 = 200$ pre-treatment periods, $T_{\text{post}} = 20$ post-treatment periods, $N_0 = 50$ donors, and $R = 500$ replications per cell of the (κ, ρ_u) grid. Table C1 summarizes which components are redrawn per replication and which are held fixed.

Table C1. FROZEN VERSUS REDRAWN COMPONENTS OF THE DATA-GENERATING PROCESS.

Component	Redrawn per rep	Fixed across reps
Donor loadings $\Lambda_{j,k}$		✓
Treated loading λ_0		✓
Unit fixed effects α_j		✓
Factor paths $F_{k,t}$	✓	
Idiosyncratic component $\mathcal{E}_{j,t}$	✓	
Stationary noise $\varepsilon_{j,t}$	✓	
Time fixed effects δ_t	✓	

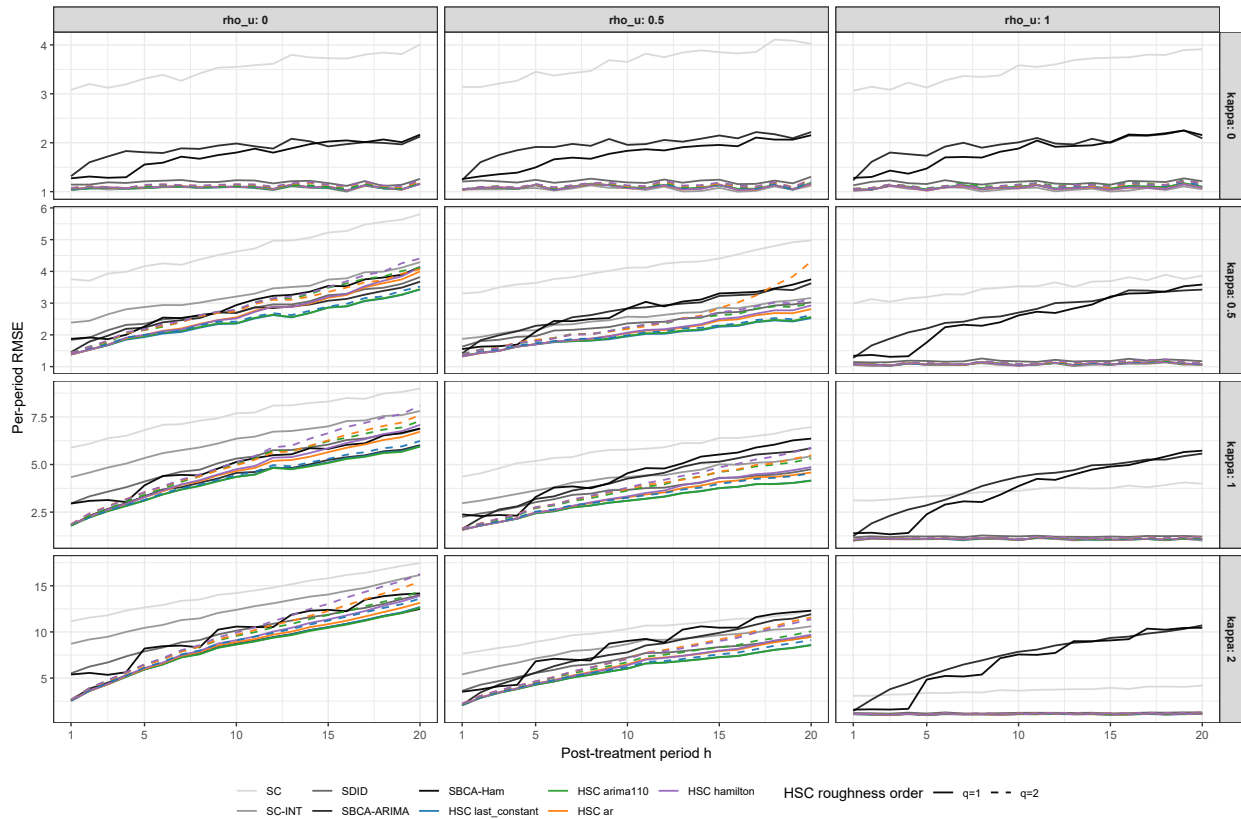
The seed for each replication is derived deterministically from a master seed and the cell index $(\kappa, \rho_u, \text{rep})$, so the entire study is reproducible. Bit-for-bit reproducibility is verified by re-running the harness with the same master seed and checking R -level identity of all numerical columns of the raw output.

C.2. Per-period RMSE

Section 6.2 reports RMSE pooled across the 20 post-treatment periods. Figure C1 shows the period-by-period picture behind the pooled comparison. In the cells with $\kappa \geq 0.5$ and $\rho_u \leq 0.5$, the constant carry-forward configurations (`last_constant` at $q = 1$ and $q = 2$) and the $q = 1$ `arma110` configuration lie at or below SC-INT and SDID at every horizon. The $q = 2$ `ar`, `arma110`, and `hamilton` trajectories instead rise above SDID and, at the longest horizons, above SC-INT, with the unfavorable gap widening as h grows; the $q = 1$ `hamilton` configuration (and, in the $\kappa=0.5$,

$\rho_u=0$ cell, $q = 1$ ar) likewise exceeds SDID at the longest horizons while staying below SC-INT. For example, at $(\kappa, \rho_u) = (2, 0.5)$ and $h = 20$ the $q = 2$ ar trajectory reaches about 11.6 against SDID 9.5 and SC-INT 10.6. In the shared stochastic trend cells (top row $\kappa = 0$ or right column $\rho_u = 1$) the per-period RMSEs are small (about 1.0–1.3) and the HSC trajectories stay near SC-INT and SDID, except the $q = 2$ forecasters, which run up to roughly 10–18% above the better of the two baselines at the longest horizons.

Figure C1. PER-PERIOD RMSE BY METHOD ACROSS THE (κ, ρ_u) GRID



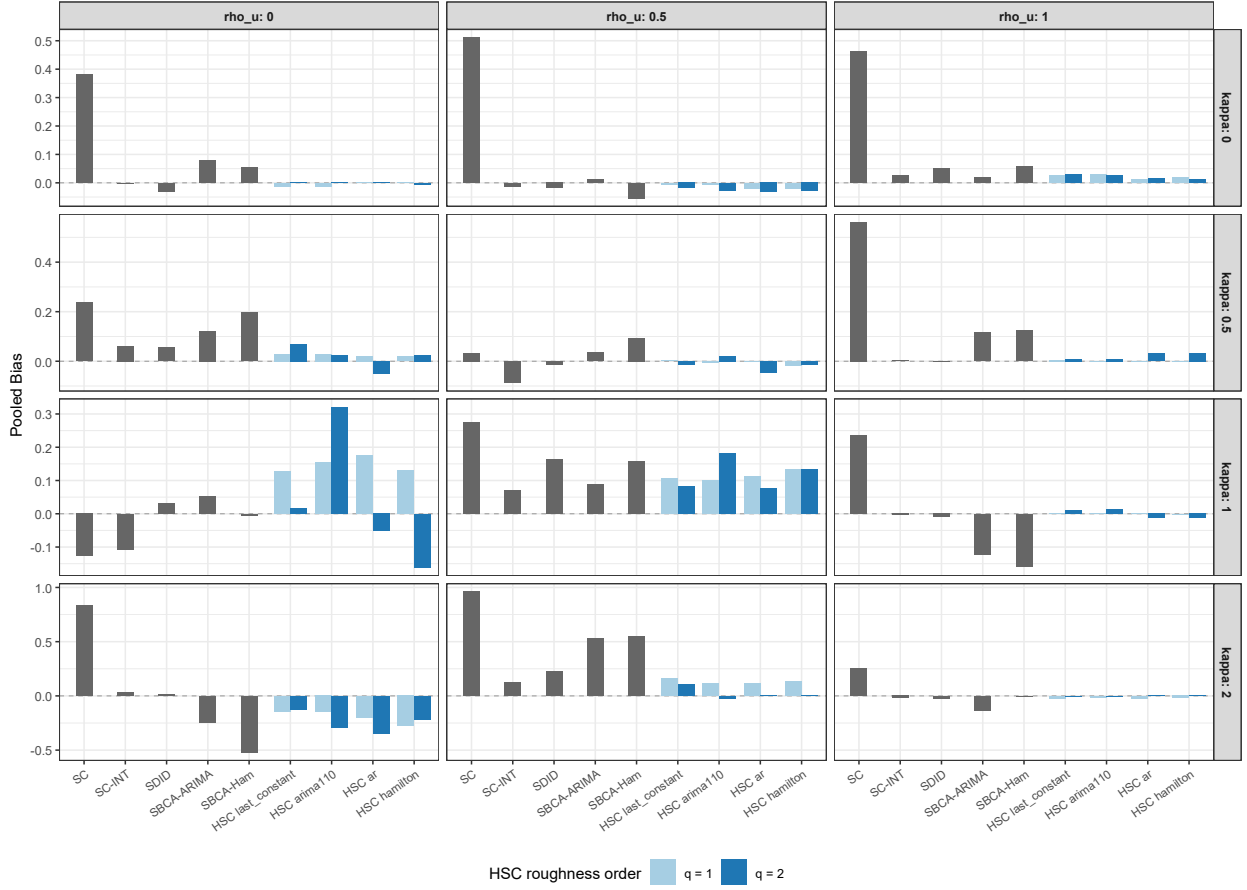
Notes: Lines report per-period RMSE $\sqrt{R^{-1} \sum_r (\hat{Y}_{1, T_0+h}^{(r)} - Y_{1, T_0+h}^{(0,r)})^2}$ across $R = 500$ replications, by post-treatment period $h \in \{1, \dots, 20\}$. Solid lines correspond to $q = 1$ and dashed lines to $q = 2$ for each HSC forecaster; baselines do not depend on q . $T_0 = 200$, $N_0 = 50$, $h = 1$ cross-validation.

C.3. Pooled bias and pooled variance

The pooled RMSE in Figure 6 can be decomposed into a bias contribution and a variance contribution. Figures C2 and C3 report the pooled bias and pooled variance using the same layout as Figure 6.

In the shared stochastic trend cells the bias is small for every method and the variance is comparable across HSC, SC-INT, and SDID. In the shared + idiosyncratic stochastic trend cells HSC carries a slightly larger bias than SC-INT and SDID but a meaningfully smaller variance, and

Figure C2. POOLED BIAS BY METHOD ACROSS THE (κ, ρ_u) GRID



Notes: Bars report pooled bias $R^{-1}T_{\text{post}}^{-1} \sum_{r,h} (\hat{Y}_{1,T_0+h}^{(r)} - Y_{1,T_0+h}^{(0,r)})$ across $R = 500$ replications and $T_{\text{post}} = 20$ post-treatment periods, for each (κ, ρ_u) cell. Layout and color encoding match Figure 6.

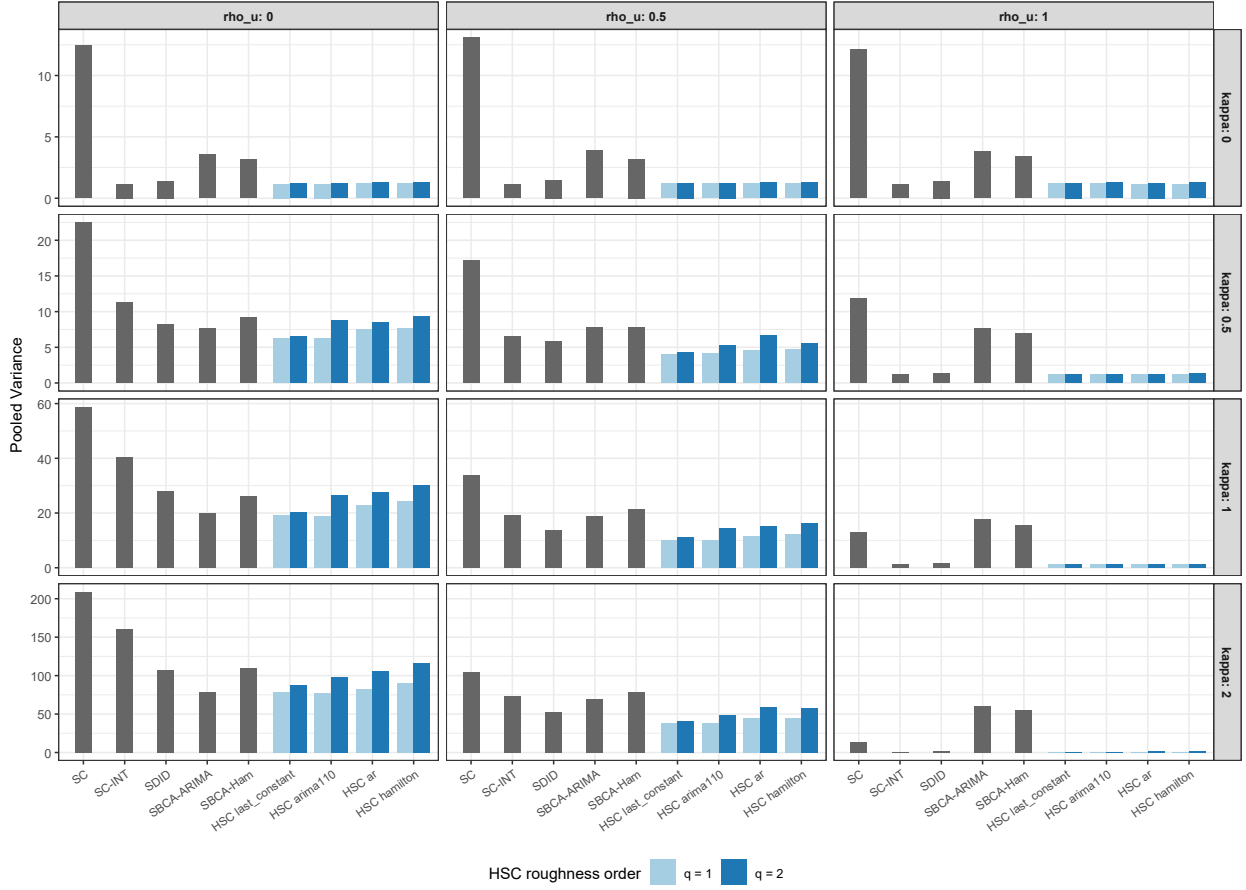
the variance reduction more than offsets the bias penalty in the pooled RMSE of Figure 6. The mechanism is consistent with the spectral interpretation of Section 4: by selecting an interior $\hat{\rho}$, HSC trades a small amount of low-frequency information against a substantial reduction in spurious matching of the donor pool to the treated unit’s idiosyncratic drift.

C.4. Cross-validation horizon

Section 6.3 fixes the cross-validation horizon at $h = 1$. Here we examine how the cross-validated $\hat{\rho}$ and the post-period RMSE shift when the horizon is extended to $h = 20$.

Distribution of $\hat{\rho}$. Figures C4 and C5 report the distribution of $\hat{\rho}$ at $h = 1$ and $h = 20$ for $q = 1$ and $q = 2$ respectively. In cells where $\hat{\rho}$ is already near one under $h = 1$ (the top row $\kappa = 0$ and the right column $\rho_u = 1$), the distribution is essentially unchanged at $h = 20$. In cells where $\hat{\rho}$ is interior under $h = 1$ (the shared + idiosyncratic stochastic trend region with $\kappa \geq 1$ and

Figure C3. POOLED VARIANCE BY METHOD ACROSS THE (κ, ρ_u) GRID



Notes: Bars report pooled variance $\text{Var}_{r,h}(\hat{Y}_{1,T_0+h}^{(r)} - Y_{1,T_0+h}^{(0,r)})$ across $R = 500$ replications and $T_{\text{post}} = 20$ post-treatment periods, for each (κ, ρ_u) cell. Layout and color encoding match Figure 6.

$\rho_u \leq 0.5$), the distribution shifts upward at $h = 20$: the median moves substantially toward one and the boxes widen. The shift is systematic across forecasters and cells. Intuitively, a longer-horizon CV objective penalizes forecaster extrapolation error more heavily, so the optimizer reallocates predictive responsibility from the time series branch toward the donor pool by raising ρ .

RMSE consequences of the horizon choice. The upward shift in $\hat{\rho}$ does not translate into uniformly better RMSE. Figure C6 reports the window-pooled RMSE at the representative shared + idiosyncratic stochastic trend cell $(\kappa, \rho_u) = (2, 0.5)$ for two windows: an early window covering post-treatment periods $\{1, \dots, 10\}$ and a late window covering $\{11, \dots, 20\}$. In the early window the $h = 1$ HSC bars sit at or below the $h = 20$ bars for every forecaster at both smoothness orders. In the late window this still holds for all $q = 1$ configurations and for the $q = 2$ arima110, hamilton, and last_constant configurations, but the $q = 2$ ar configuration reverses, its $h = 20$ bar (9.2) falling below its $h = 1$ bar (9.6). Apart from that single configuration the larger $\hat{\rho}$ selected

Figure C4. DISTRIBUTION OF $\hat{\rho}$ AT $h = 1$ VERSUS $h = 20$ CROSS-VALIDATION, $q = 1$

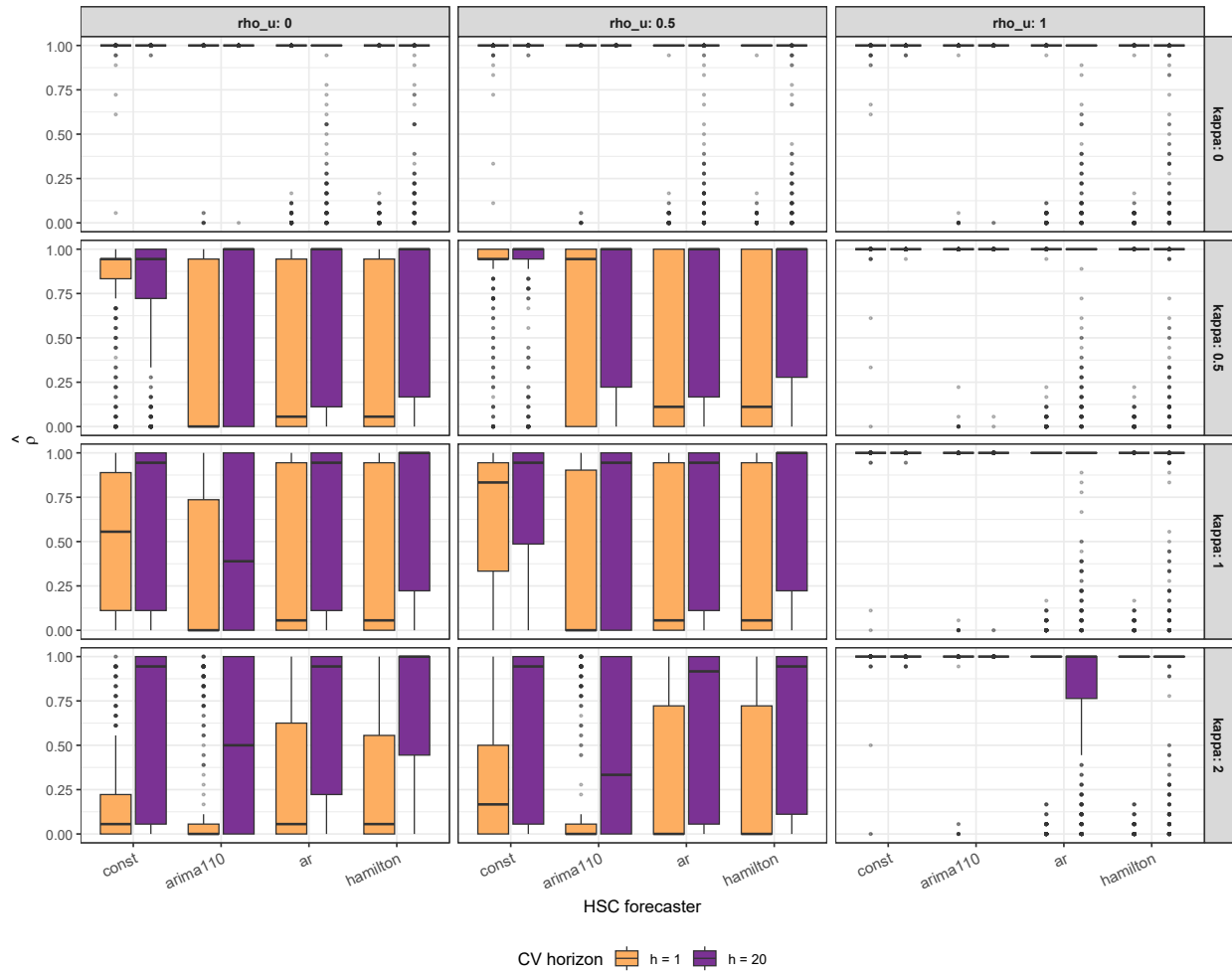


Notes: Boxplots report the distribution of the cross-validated $\hat{\rho}$ across $R = 500$ replications for each (κ, ρ_u) cell, at cross-validation horizons $h = 1$ (orange) and $h = 20$ (purple), for the four HSC time series forecasters at $q = 1$. $T_0 = 200$, $N_0 = 50$.

by $h = 20$ does not improve long-horizon predictive accuracy in this representative cell; the pattern is similar across other cells in the shared + idiosyncratic stochastic trend region.

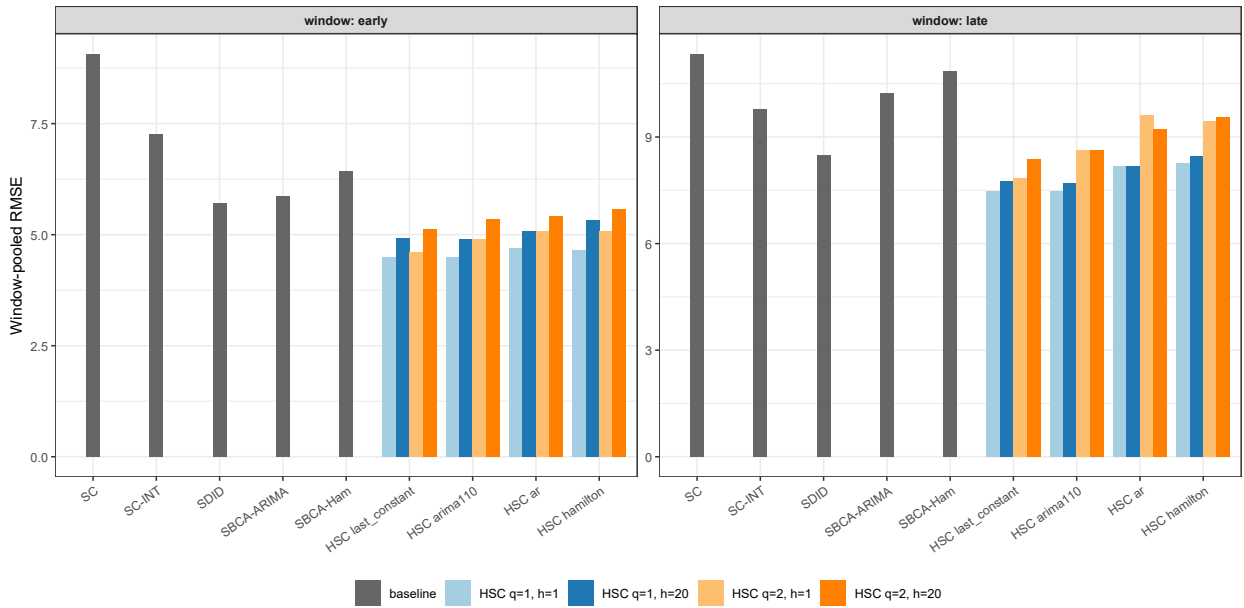
The takeaway is that the $h = 1$ default used in the main text is a robust choice: shortening the cross-validation horizon does not sacrifice accuracy at the longer post-treatment horizons, and a longer cross-validation horizon does not deliver an improvement that compensates for the additional computational cost.

Figure C5. DISTRIBUTION OF $\hat{\rho}$ AT $h = 1$ VERSUS $h = 20$ CROSS-VALIDATION, $q = 2$



Notes: Same as Figure C4 for smoothness order $q = 2$.

Figure C6. WINDOW-POOLED RMSE AT $h = 1$ VERSUS $h = 20$ CROSS-VALIDATION, REPRESENTATIVE CELL $(\kappa, \rho_u) = (2, 0.5)$



Notes: Bars report window-pooled RMSE $\sqrt{R^{-1} |W|^{-1} \sum_{r, h \in W} (\hat{Y}_{1, T_0+h}^{(r)} - Y_{1, T_0+h}^{(0,r)})^2}$ for the early window $W = \{1, \dots, 10\}$ and the late window $W = \{11, \dots, 20\}$, restricted to the cell $(\kappa, \rho_u) = (2, 0.5)$. Each HSC forecaster appears as four bars: $q = 1$ with $h = 1$ (light blue), $q = 1$ with $h = 20$ (dark blue), $q = 2$ with $h = 1$ (light orange), and $q = 2$ with $h = 20$ (dark orange). The five baseline estimators do not depend on the HSC cross-validation and appear as single grey bars. $T_0 = 200$, $N_0 = 50$.

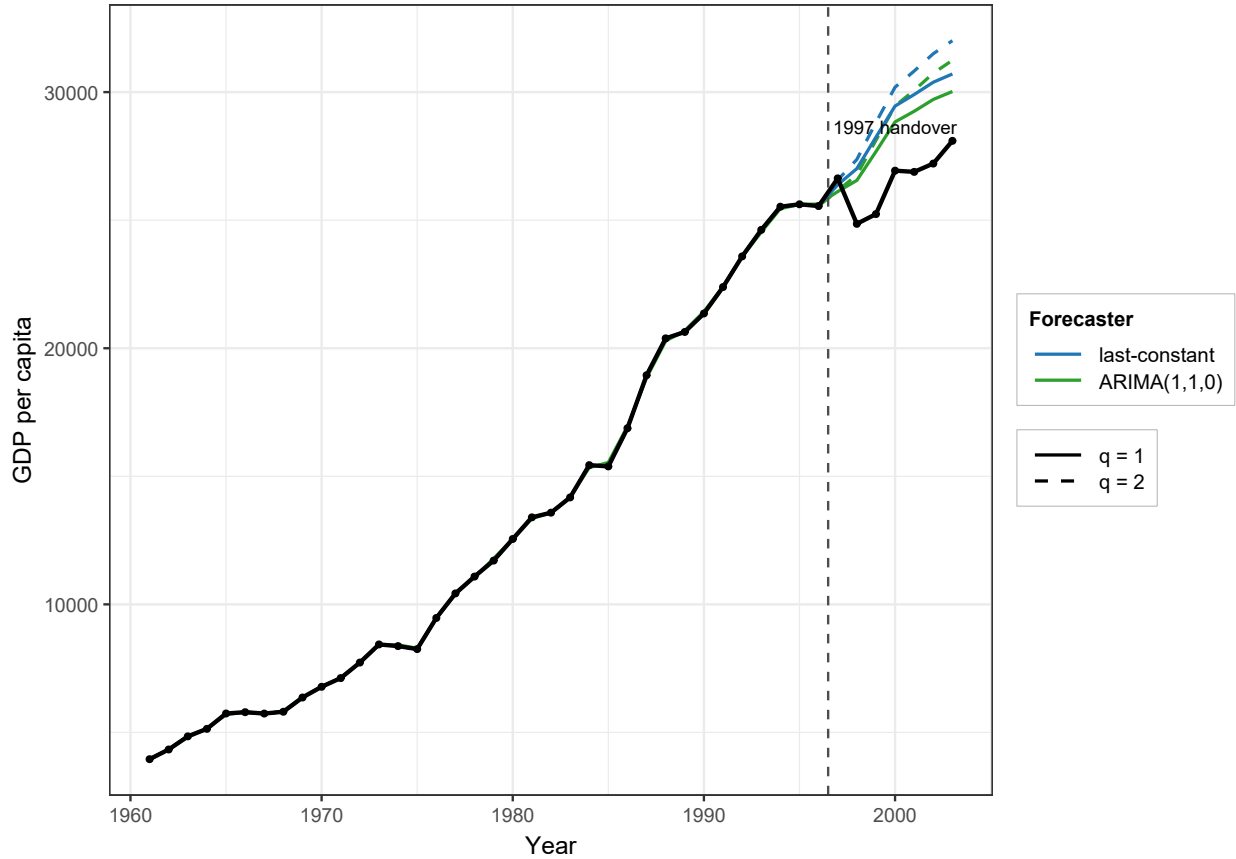
D. Hong Kong: robustness

This appendix reports three robustness checks for the Hong Kong application of Section 7: sensitivity to the choice of HSC forecaster and roughness order, sensitivity to the cross-validation horizon, and sensitivity to the donor pool. All three preserve the qualitative conclusions of the main text.

D.1. All four HSC configurations

Figure D1 overlays the counterfactuals of all four HSC configurations, each evaluated at its own cross-validated $\hat{\rho}$. The four trajectories stay close throughout the post-treatment window—within about 2% of one another in 1997, widening to about 6% by 2003—and all four imply a sizable negative effect, so the headline result of Section 7.2 is not an artifact of selecting the ARIMA(1, 1, 0), $q = 1$ configuration.

Figure D1. HONG KONG: COUNTERFACTUALS FROM ALL FOUR HSC CONFIGURATIONS ($h = 1$)

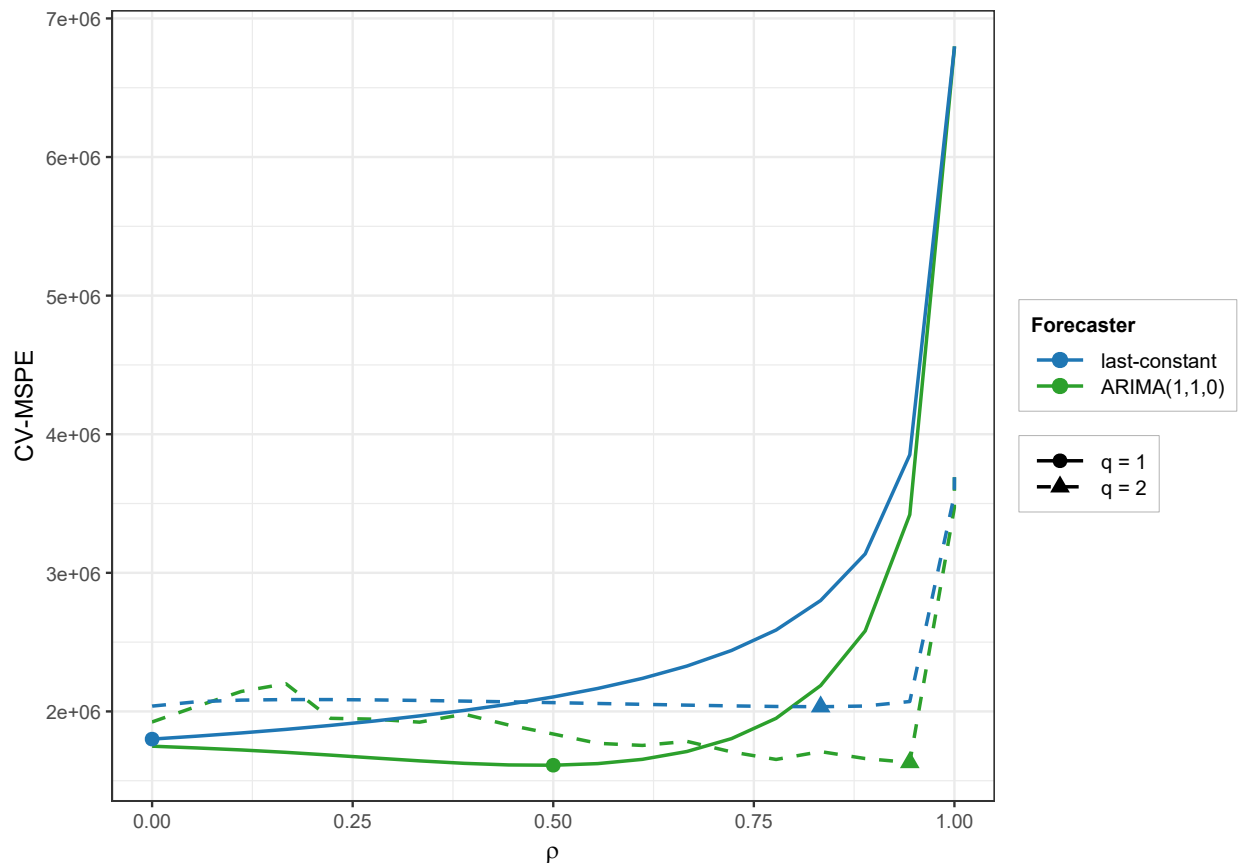


Note: Estimated no-handover counterfactuals from the four HSC configurations (`last_constant` and ARIMA(1,1,0) forecasters at $q \in \{1, 2\}$), each evaluated at its own one-step-ahead cross-validated $\hat{\rho}$, with observed Hong Kong per-capita GDP (solid black). Sample: eleven developed donor economies, annual per-capita GDP, 1961–2003.

D.2. Cross-validation horizon

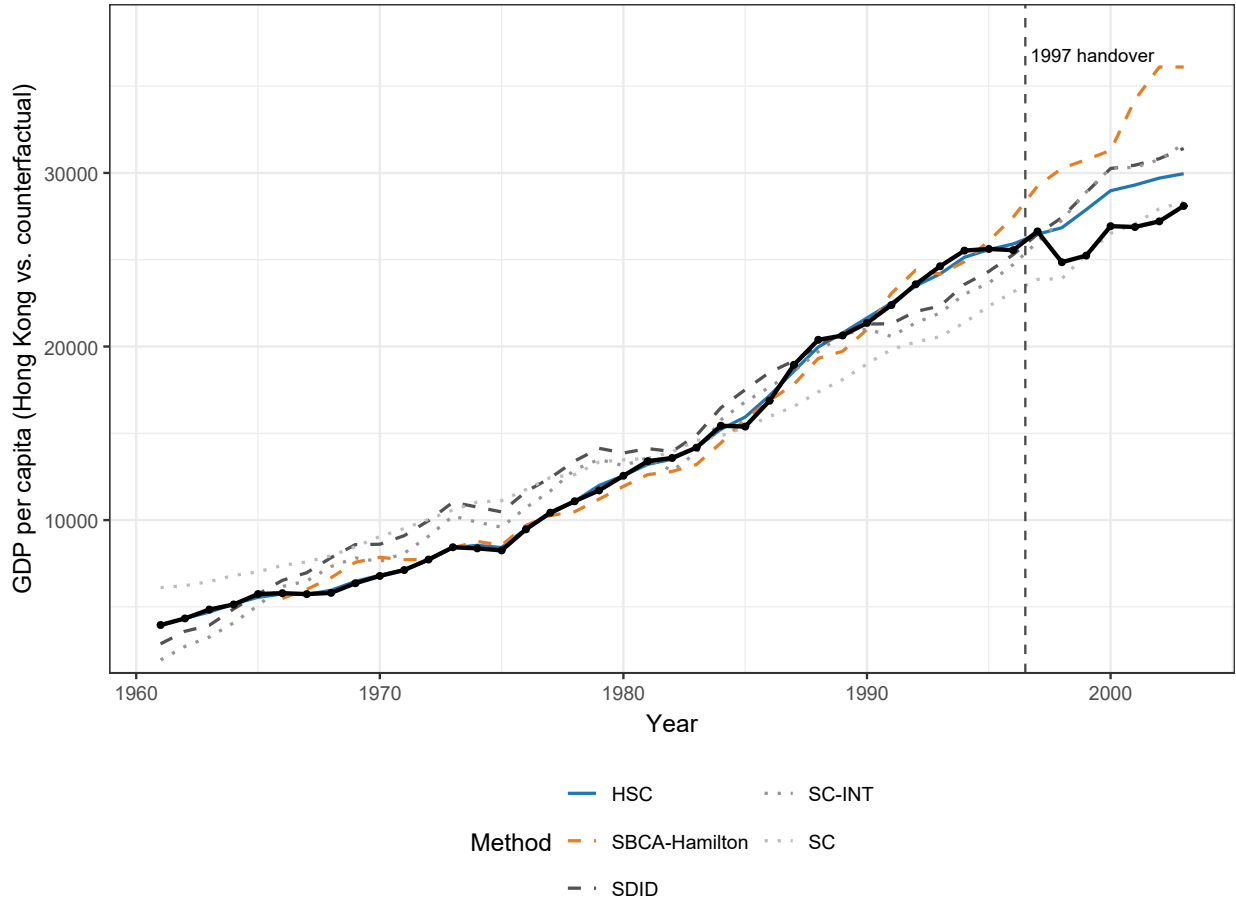
The Monte Carlo study (Section 6.3) shows that lengthening the cross-validation horizon shifts $\hat{\rho}$ upward, reallocating predictive responsibility from the treated-unit forecaster toward the donor pool. The same pattern appears in the Hong Kong data. Figure D2 shows that at $h = 4$ the cross-validated optimum of the selected configuration moves from $\hat{\rho} = 0.11$ to $\hat{\rho} = 0.50$. Figure D3 shows the resulting counterfactual comparison: HSC continues to track observed Hong Kong more closely than any baseline, and on the four-step-ahead CV-MSPE all four HSC configurations ($1.6\text{--}2.0 \times 10^6$) again fall below every baseline (SBCA-Hamilton 4.4×10^6 , SDID 4.6×10^6 , SC-INT 9.2×10^6 , plain SC 1.9×10^7).

Figure D2. HONG KONG: CROSS-VALIDATED MSPE AT THE FOUR-YEAR HORIZON ($h = 4$)



Note: Cross-validated mean squared prediction error at the four-step-ahead horizon ($h = 4$) as a function of ρ , for the four HSC configurations. A marker on each curve denotes that configuration's cross-validated $\hat{\rho}$. Relative to the one-step-ahead horizon of Figure 8, the selected $\hat{\rho}$ shifts upward (from 0.11 to 0.50), reallocating predictive responsibility toward the donor pool. Sample: eleven developed donor economies, 1961–1996 pre-treatment.

Figure D3. HONG KONG: COUNTERFACTUAL PER-CAPITA GDP BY ESTIMATOR ($h = 4$)



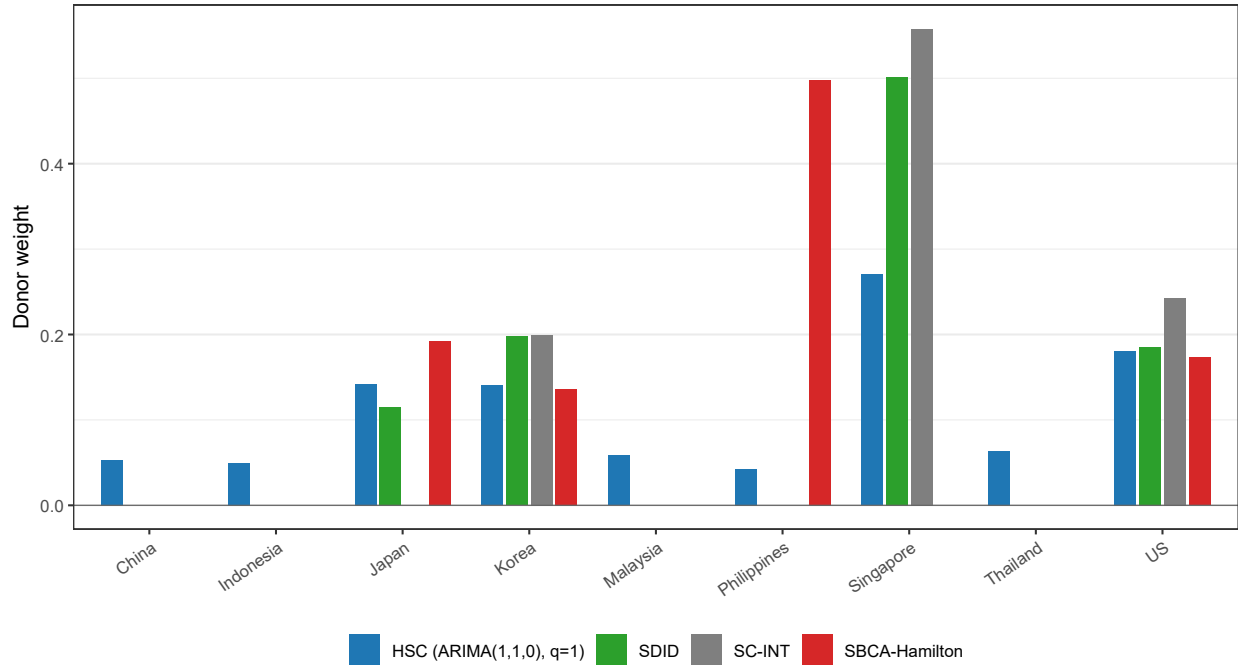
Note: Observed Hong Kong per-capita GDP (solid black) and estimated no-handover counterfactuals from the cross-validation-selected HSC configuration at $h = 4$, SBCA-Hamilton, SDID, SC-INT, and plain SC. The vertical dashed line marks the 1997 handover. Sample: eleven developed donor economies, annual per-capita GDP, 1961–2003.

D.3. Geographic-neighbour donor pool

Hsiao, Ching and Wan (2012) select donors by geographic and economic proximity rather than long-run comparability. We re-estimate HSC and the baselines on the nine economies from that pool that are available in the Shi, Xi and Xie (2025) data release—mainland China, Indonesia, Japan, Korea, Malaysia, the Philippines, Singapore, Thailand, and the United States; Taiwan, also used by Hsiao, Ching and Wan (2012), is not in the release—over the same 1961–2003 window. The cross-validation again selects ARIMA(1, 1, 0), $q = 1$ with $\hat{\rho} = 0.11$. Figure D4 shows that HSC again distributes weight broadly across the donor pool while the comparison estimators concentrate, and Figure D5 shows that the four HSC configurations again cluster. On the one-step-ahead CV-MSPE all four HSC configurations ($3.6\text{--}3.9 \times 10^5$) again fall below every baseline (SDID 5.1×10^5 , SC-INT 1.1×10^6 , plain SC 1.2×10^6 , SBCA-Hamilton 1.6×10^6). HSC’s advantage over every

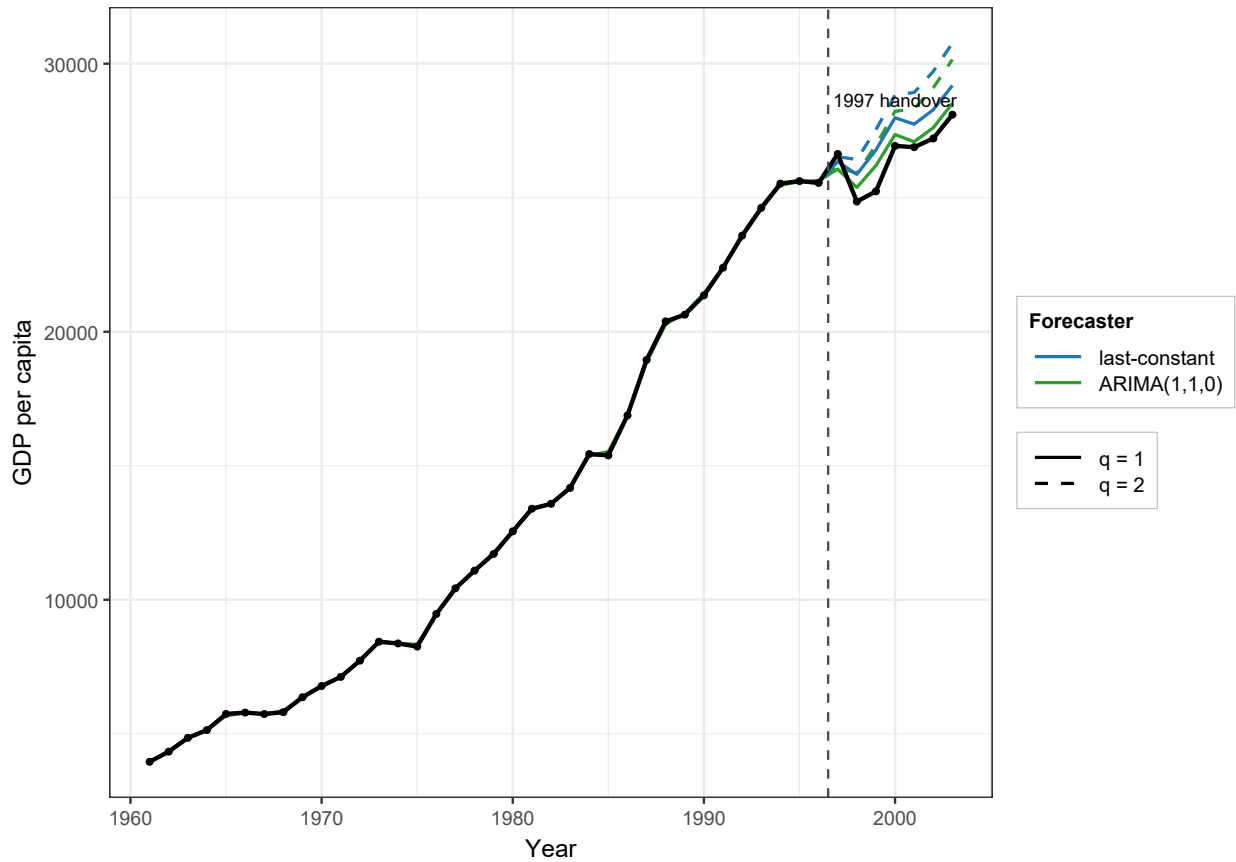
baseline therefore survives replacing the entire donor-selection philosophy. The ordering among the baselines does change: with a geographic-neighbour donor pool SBCA-Hamilton becomes the weakest comparator rather than the strongest, while SDID, SC-INT, and plain SC all improve substantially.

Figure D4. HONG KONG: DONOR WEIGHTS BY ESTIMATOR, GEOGRAPHIC-NEIGHBOUR POOL



Note: Donor weights assigned to the nine geographic-neighbour donor economies of [Hsiao, Ching and Wan \(2012\)](#) available in the [Shi, Xi and Xie \(2025\)](#) release, by the cross-validation-selected HSC configuration (ARIMA(1, 1, 0), $q = 1$, $\hat{\rho} = 0.11$), SDID, SC-INT, and SBCA-Hamilton. HSC again spreads weight broadly while the comparison estimators concentrate. Sample: annual per-capita GDP, 1961–1996 pre-treatment fitting window.

Figure D5. HONG KONG: COUNTERFACTUALS FROM ALL FOUR HSC CONFIGURATIONS, GEOGRAPHIC-NEIGHBOUR POOL ($h = 1$)



Note: Estimated no-handover counterfactuals from the four HSC configurations, each at its own one-step-ahead cross-validated $\hat{\rho}$, with observed Hong Kong per-capita GDP (solid black), estimated on the nine geographic-neighbour donors of [Hsiao, Ching and Wan \(2012\)](#). Sample: annual per-capita GDP, 1961–2003.